

Diese Dissertation haben begutachtet:

.....



DISSERTATION

Magneto-Optic Study of Novel HgTe-Based Thin Films

ausgeführt zum Zwecke der Erlangung des akademischen Grades eines
Doktors der Naturwissenschaften unter der Leitung von

Univ.Prof. Dr.rer.nat Andrei Pimenov

E138

Institut für Festkörperphysik

eingereicht an der Technischen Universität Wien
Fakultät für Physik

von

Jan Gospodarič

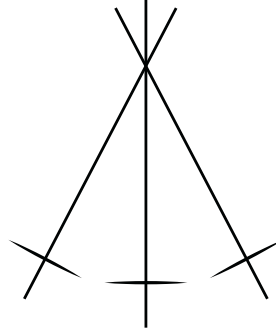
Matrikelnummer: 01639372

Hedwiggasse 2/21, 1020 Wien

Wien, am December 14, 2020



Die approbierte gedruckte Originalversion dieser Dissertation ist an der TU Wien Bibliothek verfügbar.
The approved original version of this doctoral thesis is available in print at TU Wien Bibliothek.



Ta je za vaju.

Kurzfassung

Diese Arbeit beschäftigt sich mit der magneto-optischen Untersuchung von HgTe/CdHgTe-Quantentöpfen im Sub-Terahertz-Frequenzbereich. HgTe-Quantentöpfe sind einzigartige Beispiele für zweidimensionale Systeme, in denen, abhängig von deren Dicke, viele exotische Eigenschaften auftreten, die auf sich auf die invertierte Bandstruktur von reinem HgTe zurückführen lassen.

Als primäres experimentelles Werkzeug wurden Transmissionsexperimente in einem Mach-Zehnder Interferometer mit einer kontrollierten Polarisation des Lichts durchgeführt. Dieser Ansatz ermöglichte es uns, in den untersuchten Proben die Reaktion des zweidimensionalen Elektronengases auf die angelegten elektromagnetischen Felder systematisch zu beobachten, während das Fermi-Niveau im System durch Top-Gating verschoben wurde. Mit Hilfe der Drude-Theorie und optischer Übertragungsmatrizen wurde ein Modell entworfen, um die Zyklotronresonanzen in dreidimensionalen topologischen Isolatoren auf HgTe-Basis und halbmetallischen HgTe-Proben zu analysieren.

Eine Untersuchung der Superradianz-Effekte in einem dreidimensionalen topologischen Isolator hat gezeigt, dass die Superradianz mit dem elektrodynamischen Ansatz erklärt werden kann und somit ein rein klassischer Effekt ist. Dieses experimentelle Verfahren erlaubt die Trennung der Energieverluste im System in intrinsische- und Strahlungsbeiträge.

Des Weiteren wird in dieser Arbeit ein Verfahren zur experimentellen Vermessung der Bandstruktur durch die Analyse der Zyklotronresonanz vorgestellt. Mit unserem Ansatz können die Elektronen- und Lochdispersionsbeziehungen anhand der Eigenschaften der Ladungsträger im System, wie Zyklotronmasse und Ladungsträgerkonzentration, rekonstruiert werden.

In einem dreidimensionalen topologischen Isolator wurde die Detektion separater Resonanzmoden, entsprechend den Oberflächenzuständen an zwei gegenüberliegenden Filmgrenzflächen, dem Volumenleitungsband und dem Valenzband, durch das Top-Gating ermöglicht. Unter Berücksichtigung der durch das Gate-Potential erzeugten Asymmetrie, stimmt die experimentelle Bandstruktur ziemlich gut mit den Vorhersagen des $k \cdot p$ -Modells überein.

Ein ähnliches Verfahren wurde für halbmetallische HgTe-Quantentöpfe angewandt. Eine detaillierte vergleichende Analyse der experimentellen Bandstrukturen mit theoretischen Berechnungen zeigt eine sehr gute Übereinstimmung. Dies beinhaltet als zentrale Ergebnisse die direkte Bestätigung der Elektronen- und Lochbandüberlappung, die Ermittlung der effektiven Masse der Löcher und der Nachweis des zweiten Leitungsunterbandes. Die Ergebnisse werden durch die Analyse der Shubnikov-de-Haas-Schwingungen in der Kapazität bekräftigt, welche bestätigen, dass, aufgrund von Masseninversion und Strukturinversionsasymmetrien, eine anomale zweifache Loch-Tal-Degeneration beobachtet werden kann.

Außerdem befasst sich die Dissertation auch mit den Fortschritten beim 3D-Druck als eine Möglichkeit, neuartige optische Terahertz-Komponenten zu entwerfen und zu prototypisieren. Insbesondere wird eine neue Art der Berechnung, des Designs und der Herstellung einer Wellenplatte untersucht, die einen einfallenden Strahl phasenmoduliert, um ein vordefiniertes Intensitätsprofil auf einer entfernten Bildebene zu erzeugen. Die erzielten Ergebnisse zeigen eine gute Übereinstimmung mit theoretischen Vorhersagen.

Abstract

This thesis is mainly devoted to the magneto-optical spectroscopic study of HgTe/CdHgTe quantum wells in the sub-terahertz frequency range. HgTe quantum wells are unique examples of two-dimensional systems, in which many exotic thickness-dependent properties arise due to the inverted band structure of bulk HgTe.

A Mach-Zehnder interferometer implementing controlled polarization of the light was used as the primary experimental tool for transmission experiments. This approach allowed us to systematically observe the response of the two-dimensional electron gas in the studied samples to the applied electromagnetic fields, while the Fermi level in the system was shifted by top-gating. With the help of Drude theory and optical transfer-matrices, a model of the investigated samples was designed in order to analyze the cyclotron resonances in HgTe-based three-dimensional topological insulators and semi-metallic HgTe samples.

An investigation of the superradiance effects in a three-dimensional topological insulator has shown that the superradiance can be explained using the electrodynamic approach and is therefore a fully classical effect. This experimental procedure allows the separation of energy losses in the system into distinct intrinsic and radiation contributions.

Furthermore, this work demonstrates a procedure for experimental mapping of the band structure from the analysis of the cyclotron resonance. Within our approach, the acquired properties of the charge carriers in the system, such as cyclotron mass and carrier concentration, allowed the reconstruction of the electron- and hole-dispersion relations. In a three-dimensional topological insulator, top gating allowed the detection of separate resonance modes corresponding to the surface states at two opposite film interfaces, the bulk conduction band, and the valence band. Considering the effect of the asymmetric gating potential, the experimental band structure agrees reasonably well with the predictions of the $\mathbf{k} \cdot \mathbf{p}$ model.

A similar procedure was utilized for semi-metallic HgTe quantum wells. Detailed comparative analysis of experimental band structures with theoretical calculations demonstrates a very good agreement. In detail, the main findings are a direct proof of the electron- and hole-band overlap, the effective mass of holes, and the detection of the second conduction subband. The results are strongly supported by the analysis of Shubnikov-de Haas oscillations in capacitance, which confirm that an anomalous two-fold hole-valley degeneracy is observed due to bulk inversion and structure-inversion asymmetries.

In addition, the thesis also covers advances in 3D-printing as a way to design and prototype novel terahertz optical components. In particular, a new way of calculating, designing, and fabricating a waveplate that phase-modulates an incident beam to create a predefined intensity profile on a distant image plane is investigated. The results of this show good agreement with theoretical predictions.

Contents

1	Introduction	1
2	Propagation of Electromagnetic Radiation Through Matter	5
2.1	Transfer-Matrix Formalism	5
2.1.1	Stratified Medium	7
2.1.2	Dielectric Slab	8
2.1.3	Metallic Film	9
2.1.4	Transmission Through an Insulating Slab and a Metallic Film	11
2.2	Submillimeter Continuous-Wave Spectroscopy	13
2.2.1	Mach-Zehnder Interferometer	14
2.3	3D-Printed Wave Plates	19
3	Electron Dynamics in a Two-Dimensional Crystal	25
3.1	The Drude Model	25
3.1.1	Two-Dimensional Electron Gas	26
3.2	The Semiclassical Model	28
3.2.1	Bloch Theory	28
3.2.2	Validity of the Semiclassical Model	31
3.2.3	The Effective Cyclotron Mass	33
3.3	Landau Quantization	37
4	Mercury Telluride	43
4.1	The Inverted Band Structure of HgTe	44
4.2	Strained HgTe Films	46
4.3	Sample Preparation	47
5	Experimental Investigation of HgTe Samples	51
5.1	Cyclotron Resonance Experiments	51
5.2	The Drude Analysis	56

6	Superradiance in HgTe	61
6.1	Superradiant Decay and the Drude Model	61
6.2	Superradiance in a HgTe-Based TI	64
6.3	Summary	67
7	Band Structure Mapping of 2D Crystals	69
7.1	HgTe-Based Topological Insulator	70
7.1.1	Theoretical Model	71
7.1.2	Results and Discussion	74
7.1.3	Summary	82
7.2	Semimetallic HgTe Samples	83
7.2.1	Theoretical Model	84
7.2.2	Results and Discussion	86
7.2.3	Summary	95
8	Conclusion	97
9	Acknowledgments	99
	Bibliography	103

1. Introduction

This thesis was written in the midst of a global pandemic. These uncertain times brought us into realization of how much we depend and rely on the modern-age technology, and, perhaps, that we are becoming even more addicted to it. The latest products of the technological revolution, such as artificial intelligence, advancements in gene editing and synthetic biology, nanotechnology, internet of things, digital learning and communication platforms, 3D printing, have played a major role in controlling the spread of the virus and keeping us physically and mentally sound [1]. The current health crisis certainly affected the global social and economic trends. However, as Hans Rosling describes in his book *Factfulness* [2], even the most rational and informed among us usually think worse of the world than it actually is. Before this year, we were in fact the closest to ending world hunger and poverty that we have ever been and we are statistically healthier and safer than ever. For that, we have to thank our constant strive for social, political and technological advancement.

Realizing the importance of the technological innovation for our everyday life allows us to draw in to the topic at hand. Every since the first transistor was discovered in the mid-20th Century, semiconductors have been in the spotlight for the microelectronic industry. The latter field presents one of the main driving forces of the technological revolution. The great advances in electronics and computer science were propelled forward by the outcome of the research on semiconductors. And we are not done yet. This race for further improvement, constant lowering of production costs, miniaturization is without a finish line and it strongly relies on novel discoveries in the field of semiconductors.

Semiconductors, and other solids as well, can be well described by the electronic band theory. The electronic band structure of a solid is the quantum mechanical solution for the allowed and forbidden electronic energy levels in the periodic crystal lattice. The band structure is a very important fingerprint of a solid since it can be used to explain many physical properties, such as electrical and optical conductivity, and it therefore presents a crucial part in the framework of understanding electronic components. In case the sample has an exposed surface, the standard technique of angle-resolved photoemission spectroscopy (ARPES) [3] presents an established way to obtain the necessary information. However, in several cases, especially in two-dimensional (2D) hetero-structures, several buffer and capping layers prevent collecting the data from the photo-emitted electrons, thus, making the approach with ARPES highly limited.

In condensed matter physics, topology became quite a hot topic in the recent times. In fact, it all began when the quantum hall effect was recognized as the first topological

state in matter [4, 5]. This occurred a few years after its discovery in a semiconductor by von Klitzing in 1980 [6]. Later, already in the current century, a new topological state, namely the quantum spin hall effect, was proposed [7] and later observed [8] in HgTe quantum wells, i.e, a hetero-structure of semiconducting layers. The effect arises since heavy mercury atoms cause strong spin-orbit interaction, which in turn results in a unique band reordering in bulk HgTe. While bulk HgTe is known for its zero-gap semimetallic band structure, HgTe/CdHgTe quantum wells showed multiple exotic thickness-dependent properties. Some states found in these systems are the 2D semi-metallic state [9], the Dirac-fermion system [10, 11], and the topological insulator state [12], in which the bulk insulator is accompanied by conducting surface states. In these configurations, the spin-orbit interaction results in locking between the electron spin and momentum, which raised a lot of interest from the spintronic community due to the possibility of application in means of data transfer and storage. These systems also became a popular playground for scientists in search of the Majorana fermions.

While the semiconductor scientific community has been active for more than 200 years, a relatively new field of terahertz technology emerged in the last couple of decades. Terahertz, or submillimeter radiation, represents the electromagnetic spectrum between the visible or infrared and the microwave region, therefore between the photonics and electronics. The terahertz region is also referred to as the "terahertz gap" due to the long lasting lack of sources and detectors. Both other ends of the spectrum were subject to a long history of research and developments. In the recent years, however, innovation brought us to new discoveries of possible ways of generation and detection of terahertz radiation. Terahertz spectroscopy became a very powerful and promising tool in science, industry, biology, medicine, in the security sector and in many other fields. This frequency range still presents one of the least explored electromagnetic regions and due to the great potential of its application, there is a high demand for elements that manipulate the propagation of the terahertz electromagnetic beams.

The aim of this work is to present a merger of both fields presented above. A spectroscopic study of HgTe/CdHgTe quantum wells in the sub-terahertz range of 40 – 1100 GHz. The thesis is structured as follows.

For a successful interpretations of a spectroscopic study, a theoretical framework, describing the interaction of matter with electromagnetic radiation, is required. We will show in Chapter 2 that the fundamental tool to achieve that is Maxwell's theory, which allows us to formulate a set of matrices that describe the propagation of electromagnetic radiation through various stratified media. Afterwards, we will present the Mach-Zehnder interferometer, which served as the main experimental tool for the magneto-optic experiments. The interferometric setup allows measuring the complex transmission of a continuous radiation through the sample. At the end of Chapter 2, we will briefly demonstrate that the advances in three-dimensional (3D) printing allow to design and fabricate novel components for the emerging field of terahertz technology.

Using epitaxial growth methods, semiconductor hetero-structures can be fabricated

with an atomic size accuracy. Combining layers of different materials can result in a potential well, which hosts the electrons in a very narrow 2D region, which is also known as a 2D electron gas. Chapter 3 will be devoted to the classical, semiclassical and quantum mechanical descriptions of the electron dynamics in a 2D quantum well.

Chapter 4 will describe how the interplay of the band inversion in bulk HgTe and strain induced by the hetero-structure of the investigated samples, i.e., HgTe/CdHgTe quantum wells, results in various striking phenomena. Furthermore, the exact structure of the investigated samples will be presented, specifically, two HgTe-based topological insulators and two semi-metallic systems.

The theoretical framework from the beginning of this thesis can be successfully applied to extract electronic properties of the investigated systems. In Chapter 5, the analysis of spectroscopic data will be presented. In fact, the purity of the investigated samples allows to observe cyclotron resonances of the active holes and electrons. The analysis of the response to electromagnetic fields gives us a direct access to the fundamental properties of the charge carriers. An investigation of the superradiance effects in a three-dimensional topological insulator will be presented in Chapter 6. Superradiance occurs when several emitters couple to radiate coherently, and in turn increase the energy loss rate of the system. Chapter 7 demonstrates a procedure for experimental mapping of the band structure from the analysis of the cyclotron resonance in the case of a topological insulator and two semi-metals. The comparison of the experimentally obtained band structures with the corresponding theoretical prediction, calculated by E. G. Novik in terms of the $k \cdot p$ theory, demonstrates that our approach is especially useful for 2D materials.

2. Propagation of Electromagnetic Radiation Through Matter

With the use of spectroscopy, we investigate the interaction between matter and electromagnetic radiation. For a successful analysis, it is required to develop a suitable theoretical model, which then allows characterizing the investigated material. The beginning of this chapter will briefly demonstrate Maxwell's theory, the fundamental tool to describe the propagation of electromagnetic radiation. After that, we will start to draw closer to the subject of this thesis and focus only on transmission and reflection of electromagnetic radiation when it encounters borders between many different optical media, or more specifically, stratified media. As will be shown later in this thesis, an insulating slab with a metallic film on top serves as a quite exact model of the experimentally investigated samples. Accordingly, the propagation of light through such a model will be presented in terms of 4×4 transfer-matrix formalism. This will finally allow us to obtain theoretical formulas for complex transmission. These will be used to interpret the experimental results measured by the Mach-Zehnder interferometer, i.e., the main experimental tool in this work, which will be presented in the second section of this chapter. We will present various measuring configurations of the Mach-Zehnder interferometer setup and explain how it allows measuring even the complex transmission through an investigated sample. The last section of this chapter will be focused on 3D printed beam shaping elements. This demonstration serves the reader as a convenient way to familiarize with the behavior of submillimeter radiation in practice.

2.1 Transfer-Matrix Formalism

The electromagnetic field is represented by two vectors, the electric vector \mathbf{E} and the magnetic induction \mathbf{B} . When considering the electromagnetic field in matter it is necessary to include an additional set of vectors: the electric displacement \mathbf{D} and the magnetic vector \mathbf{H} . The relations between these quantities are governed by the Maxwell's Equations [13]:

$$\nabla \times \mathbf{H} = \mathbf{j} + \frac{\partial \mathbf{D}}{\partial t}, \quad (2.1)$$

$$\nabla \times \mathbf{E} = -\frac{\partial \mathbf{B}}{\partial t}. \quad (2.2)$$

The behavior of matter under the influence of the electromagnetic field is presented by the constitutive relations:

$$\mathbf{j} = \sigma \mathbf{E}, \quad (2.3)$$

$$\mathbf{D} = \epsilon \epsilon_0 \mathbf{E}, \quad (2.4)$$

$$\mathbf{B} = \mu \mu_0 \mathbf{H}. \quad (2.5)$$

Here, σ is the electrical conductivity, \mathbf{j} is the electric current density, ϵ is the (relative) permittivity, and μ is the (relative) magnetic permeability. The constants $\epsilon_0 = 1/\mu_0 c_0^2$ and $\mu_0 = 4\pi \cdot 10^{-7}$ H/m are the vacuum permittivity and the vacuum permeability, respectively, where c_0 is the speed of light in vacuum. Eq. (2.3) is the vector form of Ohm's law. In this thesis only non-magnetic materials will be discussed, therefore we define $\mu = 1$. Conducting matter, such as metals or semiconductors, are characterized by $\sigma \neq 0$. The usual distinction between metals and semiconductors is that the conductivity of metals decreases with temperature, while for the semiconductors, σ tends to increase with temperature. However, this characterization is often faulty and unreliable. The σ of insulating matter (dielectrics) is negligibly small. Metals, insulators and semiconductors will be described in terms of their band structure later in Chapter 3. The conductivity σ and permittivity ϵ generally depend on the frequency of the applied fields. Moreover, under the influence of dynamic fields, materials often have a delayed response, which is given by complex values of σ and ϵ . Considering σ , the imaginary part results in a delayed current, while for a complex ϵ , the real part is related to the energy stored in the material and the imaginary part is related to various processes that dissipate energy. Definitions above are valid only for matter for which the physical properties are constant. It is crucial, however, to describe what happens when the properties change in space. On the boundary between two media, where n_{12} corresponds to the normal that points from the first to the second media, the conditions that are significant for our approach are the following:

$$n_{12} \times (\mathbf{E}_2 - \mathbf{E}_1) = 0, \quad (2.6)$$

stating that the tangential component of the electric vector is continuous across the boundary, and

$$n_{12} \times (\mathbf{H}_2 - \mathbf{H}_1) = \mathbf{j}, \quad (2.7)$$

meaning that the tangential component of the magnetic vector changes if there are currents present on the boundary between the two media. The simplest solutions for all electromagnetic vectors, $\mathbf{E}, \mathbf{D}, \mathbf{H}, \mathbf{B}$, can be found in the form of plane waves:

$$\mathbf{A}(\mathbf{r}, t) = \mathbf{A}_0 e^{i(\mathbf{k}\mathbf{r} - \omega t)}, \quad (2.8)$$

where \mathbf{A}_0 is some complex amplitude, $\mathbf{k} = \frac{\omega}{c} \hat{\mathbf{k}}$ is the wave vector pointing in the direction of propagation, $\omega = 2\pi\nu$ is the angular frequency of the radiation, ν is its frequency, and finally c represents the speed of light in matter. In correlation with the speed of light in vacuum c_0 , speed in matter reads $c = c_0/n$ with $n = \sqrt{\epsilon\mu}$ being the refractive index.

By the use of Eqs. (2.1) and (2.2), it can be seen that in isotropic dielectrics with $\sigma = 0$ ($\mathbf{j} = 0$) the \mathbf{E} , \mathbf{H} and \mathbf{k} form a set of three orthogonal vectors. If we set $\mathbf{k} = k(z)$ (the wave propagates along the z -axis in the Cartesian system), the wave is said to be linearly polarized if the electric (or magnetic) field is confined to a plane parallel to the z -axis or that the phase difference between E_x and E_y is a multiple of π . If $E_y/E_x = \pm i$, the wave is circularly polarized. Here, plus and minus indicate left- and right-handed circularity, respectively. Other forms, more complicated ratios of E_y/E_x , are characterized as elliptically polarized.

2.1.1 Stratified Medium

Let us draw closer to the problem at hand, which is the interaction of the electromagnetic field with an investigated material or structure, which is assumed to be stratified in the z -direction. That means that its optical properties do not change in any direction within the plane perpendicular to z , or, in simpler terms:

$$\epsilon = \epsilon(z). \quad (2.9)$$

This approach is very useful for the physics of multilayered structures, where the sample structure is combined of thin plane-parallel layers. These layers are here assumed to be infinite in the xy -plane. As we will see later in Chapter 4, such structures can be produced by the molecular-beam epitaxy technique, which allows very precise deposition or materials, even single-atom layers. Next, we consider a linearly-polarized electric field as a sum of left- and right-traveling waves, which are propagating in the z -direction:

$$E_x(z) = E^+ + E^- = E_0^+ e^{+ikz} + E_0^- e^{-ikz} \quad (2.10)$$

For convenience, we have omitted the time-dependent factors. According to Eqs. (2.6) and (2.7), in dielectric media, both electric \mathbf{E} and magnetic field \mathbf{H} have to be continuous across the interface of two media, thus making it convenient to describe the field as the vector $(E(z), H(z))$. According to Eq. (2.1):

$$H_y(z) = \frac{1}{\eta} (E^+ - E^-) \quad (2.11)$$

where $\eta = \sqrt{\frac{\mu_0 \mu}{\epsilon_0 \epsilon}}$ represents the characteristic impedance of the medium. One can conveniently write:

$$\begin{pmatrix} E_x \\ H_y \end{pmatrix} = A(\eta) \begin{pmatrix} E^+ \\ E^- \end{pmatrix}, \quad (2.12)$$

where the transformation matrix and its inverse are:

$$A(\eta) = \begin{pmatrix} 1 & 1 \\ \frac{1}{\eta} & -\frac{1}{\eta} \end{pmatrix}, \quad A(\eta)^{-1} = \frac{1}{2} \begin{pmatrix} 1 & \eta \\ 1 & -\eta \end{pmatrix}. \quad (2.13)$$

These 2×2 matrices correspond to a linearly-polarized wave in the x -plane. Since any arbitrary elliptically polarized wave can be described in a basis with two orthogonal linearly-polarized waves, it is in fact more convenient to work with (E_x, E_y, H_x, H_y) and $(E_x^+, E_y^+, E_x^-, E_y^-)$. In this case, we redefine $A(\eta)$ as:

$$A(\eta) = \begin{pmatrix} 1 & 0 & 1 & 0 \\ 0 & 1 & 0 & 1 \\ 0 & -\frac{1}{\eta} & 0 & \frac{1}{\eta} \\ \frac{1}{\eta} & 0 & -\frac{1}{\eta} & 0 \end{pmatrix}, \quad A(\eta)^{-1} = \frac{1}{2} \begin{pmatrix} 1 & 0 & 0 & \eta \\ 0 & 1 & -\eta & 0 \\ 1 & 0 & 0 & -\eta \\ 0 & 1 & \eta & 0 \end{pmatrix}. \quad (2.14)$$

As we will see below, this comes especially handy when we deal with metallic films in magnetic field.

2.1.2 Dielectric Slab

First, let's consider what happens when \mathbf{E} propagates through a dielectric media ($\sigma = 0$) with a (complex) permittivity ϵ_1 and a length of L (see Fig. 2.1):

$$\begin{pmatrix} E_x^+(L) \\ E_y^+(L) \\ E_x^-(L) \\ E_y^-(L) \end{pmatrix} = \begin{pmatrix} e^{ikL} & 0 & 0 & 0 \\ 0 & e^{ikL} & 0 & 0 \\ 0 & 0 & e^{-ikL} & 0 \\ 0 & 0 & 0 & e^{-ikL} \end{pmatrix} \begin{pmatrix} E_x^+(0) \\ E_y^+(0) \\ E_x^-(0) \\ E_y^-(0) \end{pmatrix} = M_{IS} \begin{pmatrix} E_x^+(0) \\ E_y^+(0) \\ E_x^-(0) \\ E_y^-(0) \end{pmatrix}. \quad (2.15)$$



Figure 2.1: Schematics of an insulating slab.

Let us remember here that $k = k(\epsilon_1)$. We can describe the propagation in the basis of (E_x, E_y, H_x, H_y) by using the appropriate transformation matrices $A(\eta)$:

$$\begin{pmatrix} E_x(L) \\ E_y(L) \\ H_x(L) \\ H_y(L) \end{pmatrix} = A(\eta_1) M_{IS} A^{-1}(\eta_1) \begin{pmatrix} E_x(0) \\ E_y(0) \\ H_x(0) \\ H_y(0) \end{pmatrix} = M'_{IS} \begin{pmatrix} E_x(0) \\ E_y(0) \\ H_x(0) \\ H_y(0) \end{pmatrix}, \quad (2.16)$$

where $\eta_1 = \sqrt{\frac{\mu_0}{\epsilon_0 \epsilon_1}}$. For the propagation matrix through an insulating slab we obtain the following result:

$$M'_{IS} = \begin{pmatrix} \cos(kL) & 0 & 0 & i\eta_1 \sin(kL) \\ 0 & \cos(kL) & -i\eta_1 \sin(kL) & 0 \\ 0 & -\frac{i}{\eta_1} \sin(kL) & \cos(kL) & 0 \\ \frac{i}{\eta_1} \sin(kL) & 0 & 0 & \cos(kL) \end{pmatrix}. \quad (2.17)$$

2.1.3 Metallic Film

In a metallic medium, free electrons respond to the applied field which results in a non-zero \mathbf{j} (for details, see Chapter 3). Assuming the field in a form of a plane wave, combining Eqs. (2.1), (2.3) and (2.4) shows that a metal medium can be presented as a dielectric medium with an effective dielectric permittivity:

$$\epsilon' = \epsilon + \frac{i}{\epsilon_0 \omega} \sigma \approx \frac{i}{\epsilon_0 \omega} \sigma. \quad (2.18)$$

Above, we have assumed that in metals $\sigma/\epsilon_0 \omega \gg \epsilon$. This is a valid assumption at low operating experimental frequency ranges [14] (0.1 – 1 THz in this thesis) since the frequency is much lower than the plasma frequency and the energy of the radiation is too weak to excite interband transitions. Under these conditions, ϵ can be estimated to have the same order of magnitude as for dielectrics. For example, the free electron model for metals [15], which is a good model for most metals, estimates $\epsilon = 1$. The material we investigate in this work is HgTe, which, as will be described below, has both, insulating and metallic characteristics. Its static dielectric constant is for example $\epsilon(\omega = 0) = 21$. On the other side, conductivity of metals at low frequencies is usually of the order of $10^5 \text{ } (\Omega\text{m})^{-1}$, which gives at $\omega = 1 \text{ THz}$ a striking $\sigma/\epsilon_0 \omega \approx 10^4$ thus proving that $\epsilon' = \frac{i}{\omega} \sigma$ is true even for bad metals. Due to the imaginary ϵ' , the traveling wave is damped while it propagates through the metallic medium. Introducing a complex \mathbf{k} into the wave equation and using the relation $n = \sqrt{\epsilon} = \sqrt{\sigma/2\epsilon_0 \omega}(1 + i) = n'(1 + i)$ gives:

$$\mathbf{E} = \mathbf{E}_0 e^{-\frac{\omega}{c_0} n' \mathbf{k} \cdot \mathbf{r}} e^{i(\frac{\omega}{c_0} n' \mathbf{k} \cdot \mathbf{r} - \omega t)}. \quad (2.19)$$

The metallic film with a thickness of d is assumed to be very thin, much thinner than the skin depth of the material:

$$d \ll c_0 \sqrt{\frac{2\epsilon_0}{\omega\sigma}}. \quad (2.20)$$

Usually the skin depth is a couple of μm , while the thickest metallic layer in the samples under consideration in this thesis is 80 nm. Since also the wavelength of the radiation is much larger than the thickness of the film, in this case not only the damping part in Eq. (2.19) is negligible, but the electric field inside the film can be assumed to be uniform, or in mathematical terms: $\mathbf{E}(d) \sim \mathbf{E}(0)$. Let us write the integral form of the Ampère's law (Eq. (2.1)):

$$\oint H dl = \iint j dA = \sigma E d. \quad (2.21)$$

With the help of Fig. 2.2, we can establish the next relations:

$$H_x(d) = H_x(0) + \sigma_{yy} E_y d + \sigma_{yx} E_x d, \quad (2.22)$$

$$H_y(d) = H_y(0) - \sigma_{xx} E_x d - \sigma_{xy} E_y d. \quad (2.23)$$

Here we have assumed that the conductivity σ is a tensor. This is in correlation with

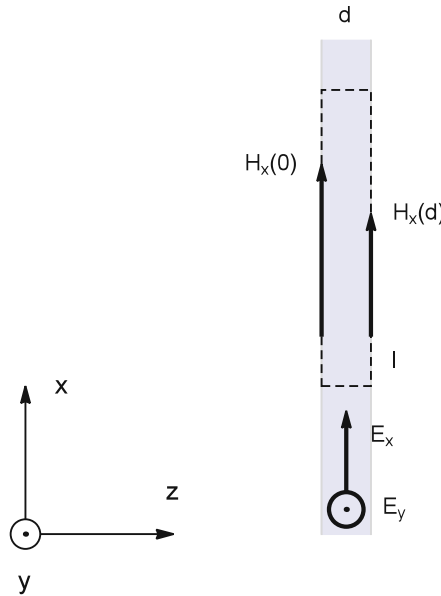


Figure 2.2: Illustration of a thin metallic film with a thickness of d in the presence of electromagnetic fields. According to Ohm's law, electric field in the xy -plane results in a current j , which is related to the magnetic field on both sides of the film with Ampère's law (Eq. (2.1)). For simplicity, the magnetic field is considered only in the x -axis.

the Drude model, described in Chapter 3, which is used to describe the conductivity of

a metal in electromagnetic fields. Accordingly, for an isotropic material, the following relations are true when the external magnetic field is perpendicular to the film (Faraday geometry): $\sigma_{xx} = \sigma_{yy}$ and $\sigma_{xy} = -\sigma_{yx}$. We can see that in the case the off-diagonal terms of σ are not zero, two initially orthogonal waves start to mix. This effect is known as the Faraday effect or Faraday rotation. Using Eqs. (2.22) and (2.23), we can construct the following propagation matrix for a thin conducting film:

$$\begin{pmatrix} E_x(d) \\ E_y(d) \\ H_x(d) \\ H_y(d) \end{pmatrix} = \begin{pmatrix} 1 & 0 & 0 & 0 \\ 0 & 1 & 0 & 0 \\ -\sigma_{xy}d & \sigma_{xx}d & 1 & 0 \\ -\sigma_{xx}d & -\sigma_{xy}d & 0 & 1 \end{pmatrix} \begin{pmatrix} E_x(0) \\ E_y(0) \\ H_x(0) \\ H_y(0) \end{pmatrix} = M'_{MF} \begin{pmatrix} E_x(0) \\ E_y(0) \\ H_x(0) \\ H_y(0) \end{pmatrix} \quad (2.24)$$

As a necessary condition for our approach, we have assumed the film to be very thin. Accordingly, we will avoid operating with a conductivity tensor in three dimensions. In the text ahead we will assign σ to the surface (or 2D) conductivity, thus setting $\sigma d \rightarrow \sigma_{2D} \rightarrow \sigma$. In such case:

$$\begin{aligned} M_{MF} &= A^{-1}(\eta) M'_{MF} A(\eta) = A^{-1}(\eta) \begin{pmatrix} 1 & 0 & 0 & 0 \\ 0 & 1 & 0 & 0 \\ -\sigma_{xy} & \sigma_{xx} & 1 & 0 \\ -\sigma_{xx} & -\sigma_{xy} & 0 & 1 \end{pmatrix} A(\eta) = \\ &= \frac{\eta}{2} \begin{pmatrix} -\eta\sigma_{xx} + 2 & -\eta\sigma_{xy} & -\eta\sigma_{xx} & -\eta\sigma_{xy} \\ \eta\sigma_{xy} & -\eta\sigma_{xx} + 2 & \eta\sigma_{xy} & -\eta\sigma_{xx} \\ \eta\sigma_{xx} & \eta\sigma_{xy} & \eta\sigma_{xx} + 2 & \eta\sigma_{xy} \\ -\eta\sigma_{xy} & \eta\sigma_{xx} & -\eta\sigma_{xy} & \eta\sigma_{xx} + 2 \end{pmatrix}. \end{aligned} \quad (2.25)$$

2.1.4 Transmission Through an Insulating Slab and a Metallic Film

The quantity we measure with the experimental procedure described below is the complex transmission through the sample of interest. Therefore, we are required to obtain the transmission formulas for the transfer matrices from the previous sections. It is very convenient to use transfer matrices to analyze the propagation of electromagnetic waves through a stratified medium. A system of various layers of materials can be simply represented as a system matrix, which is a product of all individual layer matrices. We first return to the basis of waves of electric field, propagating in left and right directions. Due to the off-diagonal terms in the transfer matrix for a metallic film, we are required to use a set of two orthogonal linearly-polarized waves. For a system transfer matrix M we can write:

$$\begin{pmatrix} E_x^+(d) \\ E_y^+(d) \\ E_x^-(d) \\ E_y^-(d) \end{pmatrix} = M \begin{pmatrix} E_x^+(0) \\ E_y^+(0) \\ E_x^-(0) \\ E_y^-(0) \end{pmatrix}. \quad (2.26)$$

To obtain the complex transmission coefficients for an incident wave, linearly polarized in the x -direction, we can write:

$$\begin{pmatrix} t_p \\ t_c \\ 0 \\ 0 \end{pmatrix} = M \begin{pmatrix} 1 \\ 0 \\ r_p \\ r_c \end{pmatrix}, \quad (2.27)$$

which present a system of four linear equations with four unknown variables t_p , t_c , r_p , and r_c , corresponding to the complex parallel and crossed transmission and reflection coefficients, respectively. If the external media is characterized by η , the solution of the system for t_p (obviously $t_c = 0$) of an insulating slab from Eq. (2.17), where $M = A^{-1}(\eta)M'_{IS}A(\eta)$, is as follows:

$$t_p = \frac{2i\eta\eta_1}{2i\eta\eta_1 \cos(kL) + (\eta^2 + \eta_1^2) \sin(kL)}. \quad (2.28)$$

For the metallic film, we already acknowledged the characteristic impedance of the outer medium, therefore $M = M_{MF}$ and it follows that:

$$\begin{aligned} t_p &= \frac{2\eta\sigma_{xx} + 4}{\eta^2\sigma_{xx}^2 + \eta^2\sigma_{xy}^2 + 4\eta\sigma_{xx} + 4}, \\ t_c &= \frac{2\eta\sigma_{xy}}{\eta^2\sigma_{xx}^2 + \eta^2\sigma_{xy}^2 + 4\eta\sigma_{xx} + 4}. \end{aligned} \quad (2.29)$$

The samples that are investigated in this thesis (see Chapter 4 for details) can be approximated with a structure of a dielectric slab and a thin conducting film surrounded by free space with the corresponding impedance of $\eta_0 = \sqrt{\mu_0/\epsilon_0}$. One can obtain an analytical solution for a corresponding transfer matrix $M = A^{-1}(\eta_0)M'_{MF}M'_{IS}A(\eta_0)$. For a system, where an insulating slab has a permittivity of ϵ_1 and length of L , we obtain the following formulas for transmission:

$$t_p = \frac{2a_{xx}}{a_{xx}^2 + a_{xy}^2}, \quad t_c = \frac{2a_{xy}}{a_{xx}^2 + a_{xy}^2}, \quad (2.30)$$

with:

$$\begin{aligned} a_{xx} &= (1 + \sigma_{xx}\eta_0)\left(\cos\beta - \frac{1}{\sqrt{\epsilon_1}}\sin\beta\right) + \cos\beta - i\sqrt{\epsilon_1}\sin\beta, \\ a_{xy} &= \sigma_{xy}\eta_0\left(\cos\beta - \frac{1}{\sqrt{\epsilon_1}}\sin\beta\right), \end{aligned}$$

where $\beta = \sqrt{\epsilon_1}\frac{\omega}{c_0}L$, the ω we know from before as the angular frequency of the incident radiation, and σ_{xx} , σ_{xy} are the components of the conductivity tensor of the metallic film.

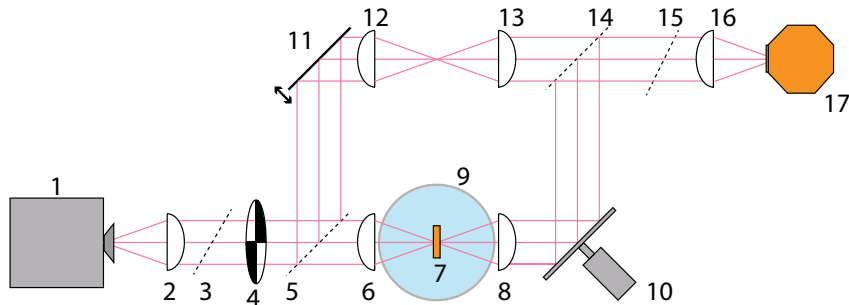


Figure 2.3: Illustration of the Mach-Zehnder interferometer for THz experiments. The elements of the interferometer are the following: (1) Source of radiation (Backward wave oscillator), (2,6,8,12,13,16) Dielectric lenses for focusing and collimation of the THz beam, (4) modulation chopper, (3,5,14,15) wire-grid polarizers, (9) helium-cooled magnet, (7) the investigated sample, (10) the movable mirror, (17) the detector, and (11) the modulation mirror. See text for details.

2.2 Submillimeter Continuous-Wave Spectroscopy

The main source of experimental data in this thesis is the submillimeter continuous-wave spectroscopy, or more specifically the Mach-Zehnder interferometer [16, 17]. This device allowed to measure the amplitude and phase shift of the transmitted radiation through a sample with controlled polarization [18, 19]. The operating frequency range, i.e., submillimeter or terahertz (THz) range, occupies the region between microwaves and infrared light in the electromagnetic spectrum. Its commonly regarded band of frequencies is between 0.3 to 3 THz, however, these boundaries are often subject to variation. The THz radiation can be guided in similar ways as in optical setups, however, the corresponding longer wavelengths require lenses, used for collimation and focusing the THz beams, that are made from specific dielectric materials, which have appropriate THz absorption and THz-refractive indices. Some of these materials are polytetrafluoroethylene (PTFE), high-density polyethylene (HDPE), polypropylene (PP) [20, 21]. Some are even 3D-printable, such as polystyrene or polylactide [22], but more about that in Section 2.3. It is interesting to note that these lenses are not transparent to the naked eye. Since THz range borders to the microwave region, the wavelengths of THz beams can take values up to a couple of millimeters. Accordingly, the measured samples, optical windows, and optical channels have to have appropriate sizes to avoid the diffraction limit. Below, the main experimental tool, the Mach-Zehnder Interferometer, will be explained in detail.

2.2.1 Mach-Zehnder Interferometer

An interferometer is a widely used experimental tool in various fields of science in which electromagnetic waves are superimposed. The measured result of this interference is used to extract valuable information about the paths of the beams or their characteristics. The illustration of the interferometer used in this thesis is sketched in Fig. 2.3. We shall now describe its elements, starting from the generation of radiation and all the way to its detection. The enumeration of elements in the text corresponds to the enumeration in Fig. 2.3.

The radiation used in our interferometer was produced by backward wave oscillators (BWOs) – compact, powerful, and tunable monochromatic generators (see Fig. 2.4(a)). Their design and principle of operation were developed in the 1960s [23]. Using heat, electrons are emitted from the cathode and are accelerated by a high electric field (up to 6 kV) through vacuum towards the anode. External magnetic field helps keeping the electronic beam collimated while they fly over an electrode with a comb-like structure. Since they experience a periodically varying potential, the electrons periodically group in bunches, which results in a backward traveling electromagnetic wave, which comes out of the device through a waveguide. The frequency and the power of the emitted radiation are determined by the accelerating voltage U . While the frequency approximately scales as a square root of the applied voltage, the output power produces a very complicated spectrum. The output frequency range is dependent on the design of each specific BWO, accordingly, in the experimental setup described below, several BWOs were used to cover the region between 38 GHz to 1.1 THz (see Fig. 2.4(b)).

Let us return to the Mach-Zehnder interferometer seen in Fig. 2.3. The radiation produced by the BWO (1), which is assumed to have a Gaussian transverse profile, is first collimated by a lens (2). After, the beam passes through two rotatable wire-grid polarizers (3,5), each consisting of an array of parallel metallic wires. These only allow the transmission of radiation with an electric field vector perpendicular to the direction of the wires and reflect all radiation with the electric field vector parallel to the wires. The first polarizer sets the polarization of the beam, while the second polarizer (beam-splitter) is used to split the beam into two orthogonal beams. The beams are directed through the "reference arm" and the "sample arm" of the interferometer. The intensities of the beams in both arms are adjusted by the first polarizer. In both beam paths, lenses (6,8,12,13) are used to focus the beams to a tight spot and convert them back to collimated ones. The investigated sample is placed into the focus of the sample arm, while the reference arm remains empty. The set of lenses (12,13) in the reference arm serve to ensure that the sample and the reference beam have an identical phase shift due to the optical thickness of the lenses.

The sample (7) is placed in a magneto-optic cryostat (9), which allows cooling the sample down to 1.8 K by pumping the sample chamber with liquid helium. A split-coil superconducting magnet can provide a magnetic field up to ± 7 T parallel (Faraday geometry) or perpendicular (Voigt geometry) to the k -vector of the THz radiation.

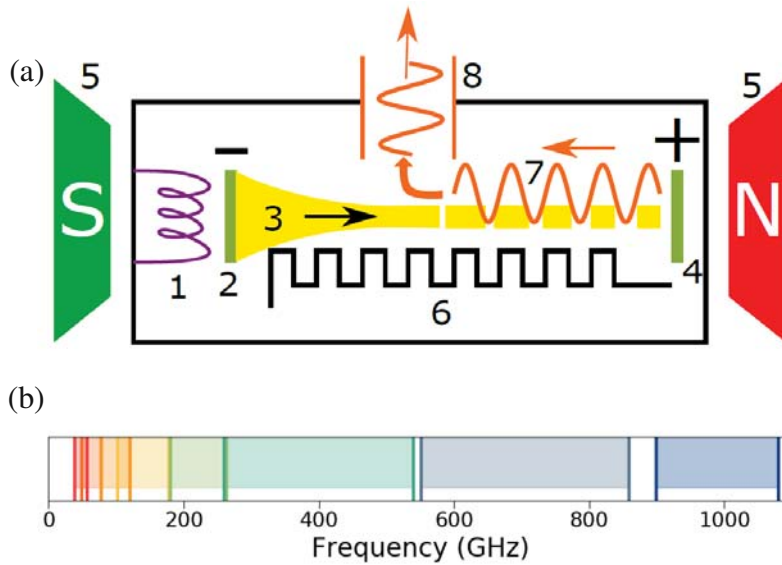


Figure 2.4: (a) Illustration of the BWO's principle of work. The heating (1) causes the electrons to emit from the cathode (2). The electrons travel towards the anode (4) and are collimated by the magnetic field (5). The electronic beam (3) get modulated by the periodic structure (6), which results in an electromagnetic wave (7) that is finally guided outside by the waveguide (8). (b) The operating frequency range of the available BWOs. Figure taken from Ref. [24].

In both arms of the interferometer, there is a mirror, reflecting the corresponding beam by 90° . The mirror (10) in the sample arm is put on a motorized translation stage, which allows movement in a range of 10 mm. In the reference arm, the position of the mirror (11) modulates with a low frequency of 28 Hz. As will be discussed ahead, the movable mirrors allow performing sensitive phase measurements.

Both beams are joined with the beam-splitter (14), which is rotated by 90° in respect to the first beam-splitter, i.e., the reference beam passes through and the sample beam is reflected. After, an additional analyzing polarizer (15) is used to interfere the two beams, merging them into a linearly-polarized beam, which is focused (16) into a liquid helium-cooled bolometer (17) with a high-frequency cut-off filter of 3 THz. The silicon plate in the bolometer is cooled to 4.2 K, where it has a very high temperature coefficient $\alpha = \frac{1}{R} \frac{dR}{dT}$. The device is very sensitive to heating due to incoming radiation, which results in a change of resistance $\Delta R = \alpha R \Delta T$. Since at low temperatures the change of resistance is mostly due to the heating of electrons, the time constant of the device is very short (\sim ms).

The interferometer can be used in several modes of operation, depending on what information about the sample one needs to extract. Transmission measurement mode, presented in Fig. 2.5(a), uses only the sample arm, and the reference beam is blocked. A modulation chopper (4) is inserted after the first lens (2), which periodically blocks

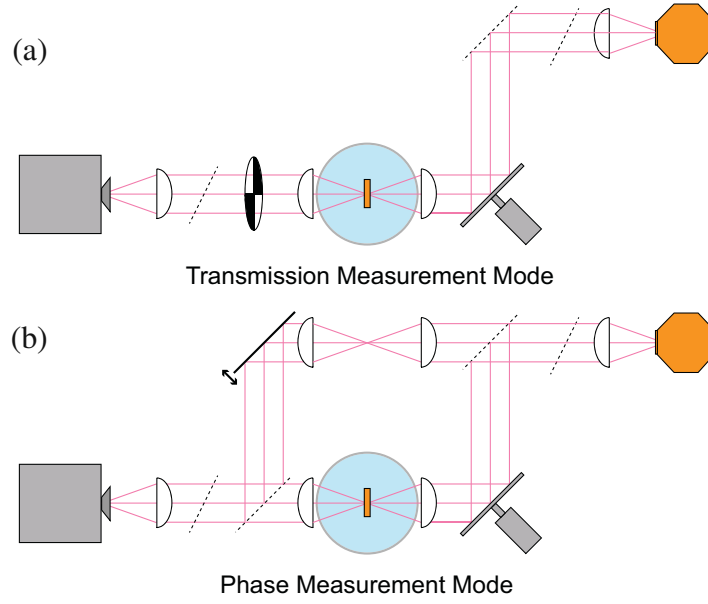


Figure 2.5: Illustration of the two measurement modes of the Mach-Zehnder interferometer. (a) Transmission measurement mode uses only the sample arm and the (b) phase measurement mode requires both, the sample and reference arm. See Fig. 2.3 and text for details.

the beam and therefore modulates the beam with a specific modulation frequency. The chopper includes a photo-sensor which produces an electric signal every time the beam is blocked by a blade of the chopper. These signal pulses are used as a reference signal for the lock-in detection system, which isolates the measured intensity of the beam from the noisy background, drastically increasing the signal-to-noise ratio.

To acquire the experimental data, it is necessary to measure the transmitted radiation intensity twice, once with the sample ($I_{sample}(\omega)$) and once without ($I_{ref}(\omega)$). The ratio of the measured intensities gives the squared absolute value of the complex transmission amplitude:

$$|t^2(\omega)| = \frac{I_{sample}(\omega)}{I_{ref}(\omega)}. \quad (2.31)$$

The other, phase measurement mode (Fig. 2.5(b)), requires that both, the reference and the sample beam, are opened and the chopper is removed. The reference beam is modulated by the oscillating mirror and the phase difference between the beams can be adjusted by the moving mirror in the sample arm of the interferometer. The intensity of the radiation at the bolometer can be written as the time average of the complex Poynting vector [25]:

$$\mathbf{I} = \langle \mathbf{S} \rangle = \langle \mathbf{E} \times \mathbf{H}^* \rangle = \frac{1}{2\eta} |\mathbf{E}|^2. \quad (2.32)$$

We have assumed that the electromagnetic vectors have plane-wave forms (see

Eq. (2.8)). The intensity of the interference between the sample beam with $E_{sam}e^{i(\varphi_{sam}-\omega t)}$ and the reference beam with $E_{ref}e^{i(\varphi_{ref}-\omega t)}$ can be written as:

$$I(t) = \frac{1}{2\eta_0} \left| E_{sam}e^{i(\varphi_{sam}-\omega t)} + E_{ref}e^{i(\varphi_{ref}-\omega t)} \right|^2 \quad (2.33)$$

Taking the time average gives us:

$$\begin{aligned} I &= \frac{1}{2\eta_0} \left(|E_{sam}|^2 + |E_{ref}|^2 + 2E_{sam}E_{ref} \cos(\varphi_{sam} - \varphi_{ref}) \right) \propto \\ &\propto const. + E_{sam}E_{ref} \cos(\varphi_{sam} - \varphi_{ref}). \end{aligned} \quad (2.34)$$

Above, only the interference term is not constant. If the modulation mirror oscillates with an amplitude δl and frequency Ω , it causes a phase modulation $\delta\varphi = \delta\varphi_0 \cos(\Omega t)$ of the reference beam, where $\delta\varphi_0 = \frac{2\pi\delta l}{\lambda}$. We can set $\Delta\varphi = \varphi_{sam} - \frac{2\pi}{\lambda}d - \frac{2\pi}{\lambda}\Delta l$ as the "static" phase difference between the two arms of the interferometer, which includes: a) the difference between the paths the light travels in both arms due to the displacement of the moving mirror by Δl , b) the optical thickness of the sample $\varphi_{sam}\lambda/c = nd$, where n is the sample's refractive index and d is its thickness, and c) the gained phase in the reference beam on the same distance as the thickness of the sample d . The modulation $\delta\varphi$ is set to be small, therefore, with a help of certain trigonometric identities, we can write:

$$\begin{aligned} I &\propto E_{sam}E_{ref} \cos(\varphi_{sam} - \varphi_{ref}) = E_{sam}E_{ref} \cos(\delta\varphi + \Delta\varphi) = \\ &= E_{sam}E_{ref} (\cos(\Delta\varphi) \cos(\delta\varphi) - \sin(\Delta\varphi) \sin(\delta\varphi)) \approx \\ &\approx E_{sam}E_{ref} \left(const. - \frac{\delta\varphi_0}{4} \cos(\Delta\varphi) \cos(2\Omega t) - \delta\varphi_0 \sin(\Delta\varphi) \cos(\Omega t) \right). \end{aligned} \quad (2.35)$$

A digital unit measures the detected signal on the bolometer as a function of time and tries to minimize the amplitude of the first harmonic component ($\cos(\Omega t)$) in the equation above. To ensure $\sin(\Delta\varphi) = 0$, the movable mirror has to move to either positive or negative Δl so that $\Delta\varphi = 2\pi N$, where the integer N is the interference order. In principal, any N suffice, but only the zeroth order is wavelength independent. To acquire the phase of the transmission, one first measures the mirror position for the zeroth order without the sample Δl_0 . Assuming that the refractive index n is constant in the operating frequency range, this "calibration" measurement could be used for any wavelength. However, in practice this condition is not enough. The Δl_0 needs to be measured for each selected frequency due to the standing waves between the elements of the quasi-optical setup, which modify the phase of light in each arm of the interferometer. After acquiring the $\Delta l_0(\lambda)$, the sample is inserted with the help of a sliding sample holder and the mirror position is measured as a function of a required variable, such as magnetic field, temperature, or gate. The phase shift of the transmitted radiation is then calculated

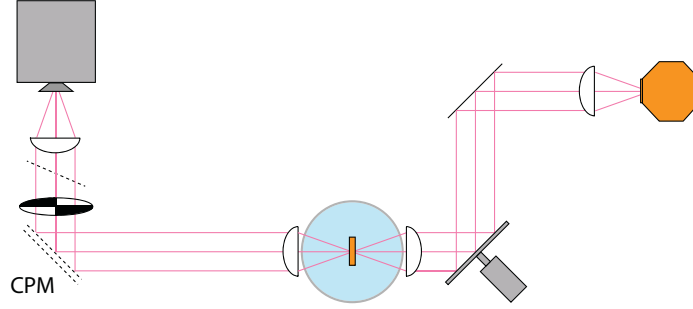


Figure 2.6: Illustration of the transmission measurement mode with circularly-polarized radiation which is achieved by the addition of the circular polarization mirror (CPM) into the optical path. See also Fig. 2.3 and text for details.

as:

$$\varphi = 2\pi(\Delta l_{sam} - \Delta l_0 + d)/\lambda. \quad (2.36)$$

The second harmonic in Eq. (2.35) becomes maximal when the first harmonic is zero. The measured amplitude of the second harmonic is proportional to E_{sam} , which allows obtaining the complex transmission of the sample $t(\omega) = cE_{sam}e^{i\varphi}$, where c is some constant. To acquire the scaling parameter c , results from the transmission measurement mode can be used as will be demonstrated later in Chapter 5.

In the phase measurement mode, shown in Fig. 2.5(b), the interferometer allows two measuring geometries: parallel and crossed. In parallel geometry, the polarizer (3) sets the ratio between the amplitudes of the beams in the sample and the reference arm. The second beam splitter (14) has to be rotated by 90° with respect to the first beam splitter (5). The analyzing polarizer (15) interferes the beams from both arms of the interferometer and the resulting linearly-polarized beam is detected by the detector. Effectively we measure the complex transmission through the sample parallel to the polarization of beam incident on the sample. In the second, crossed geometry, the previous setup is partially reconfigured. The second beam splitter (14) is set to be parallel to the first beam splitter (5). An additional polarizer is positioned between elements (13) and (14) which rotates the polarization of the reference beam so that at least part of the beam transmits through the beam splitter (14) and interferes with the sample beam. This mode is called crossed, since only the polarization, perpendicular to the polarization of the beam incident on the sample, is interfered with the reference beam and measured by the detector.

Several experiments in this thesis were also conducted with the use of a circularly-polarized beam. For a circularly-polarized beam $E_y/E_x = \pm i$, where the \mathbf{k} -vector of the beam is pointed along the z -axis. Since the BWO's output radiation is originally linearly polarized, one component of \mathbf{E} needs to be phase-shifted by half of the wavelength in comparison to the other component along the orthogonal axis. This is achieved by adding a circular polarization mirror in the interferometer as seen in Fig. 2.6. This element is composed of two parallel wire-grid polarizers with an adjustable distance

between them. The metallic arrays of the polarizers are set to be perpendicular to each other, which ensures that both components of the incoming beam are reflected. If the metallic arrays are pointed along 0 and 90° , the linear polarization of the incoming beam needs to be pointed along $\pm 45^\circ$ in order to ensure that the components of \mathbf{E} along the directions of both metallic arrays are equal. The polarization of the incoming beam is adjusted by an additional polarizer in front of the circular polarization mirror. A circularly-polarized wave is then achieved, if the distance between the wire grids in the circular polarization mirror equals $(M + 1/2)\lambda$, for some integer M . In order to guide the circularly-polarized beam to the detector, the beam splitter (14) needs to be replaced with a metallic mirror. It should be clear that with the addition of the circular polarization mirror only the transmission measurement mode is possible.

2.3 3D-Printed Wave Plates

In analogy to the situation in optics, elements to manipulate the intensity and shape of a beam are of crucial importance. An efficient way to design such elements is to combine the holographic principles with computer-supported calculations of the beam propagation [26–30]. Such an approach allows not only to manipulate a beam but moreover to generate pictures of real and imaginary objects on short timescales. Recently, optical meta-surfaces [31–34] added several interesting new ideas to the field, especially ways to miniaturize the optical units.

Alternatively, optical elements for picture generation may be produced based on phase control of light only. Such elements are often called phase holograms and they manipulate the incident wave by coordinate-dependent phase changes [35–39]. Well-known examples of phase holograms are dielectric Fresnel lenses or dielectric diffraction gratings. All such elements can be designed for frequencies as low as THz because the underlying Maxwell equations of light do not contain the wavelength as a parameter.

The goal of this section is to demonstrate that a very practical way to produce such phase holograms is to work with a commercially available 3D-printer. Additive manufacturing with 3D-printers has gained significant attention in recent years due to its versatility, accessibility, and generally because it presents a quick, easy-to-use, and cost-efficient technique to fabricate complex and high-precision structures. The layer height resolution of 3D-printers (~ 0.1 mm) and high transparency of the polymers used in 3D-printers [22] are ideally suited for printing devices that manipulate electromagnetic radiation in the THz region. Recent examples of 3D printed THz elements are diffraction gratings, lenses, optical waveguides, prisms, etc. [40–47]. Here we make a significant further step in the field of THz imaging by designing and 3D-printing dielectric plates which are able to reproduce the picture of an arbitrary object.

In our proof-of-principle demonstration, we modulate the phase profile of an incident asymmetric Gaussian beam with a wavelength of $\lambda_0 = 2.14$ mm ($\nu = 140$ GHz) at

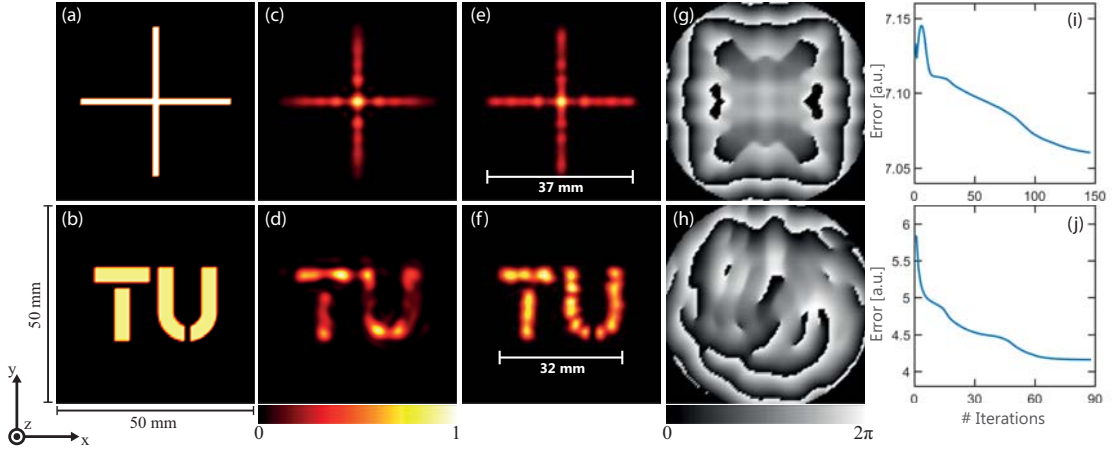


Figure 2.7: (a,b) The target intensity profiles used in present experiments. (c,d) Calculated intensity profiles at $z_i = 50$ mm after the first iteration step of the GS algorithm as compared to the result of the last (e,f) iteration step, respectively. (g,h) Calculated phase modulation profiles at $z_0 = 0$ mm. The frames are cropped to 50×50 cm² size for better comparison with the experiment. (i,j) Algorithm error (mean square deviation from the target profile) as a function of the iteration number.

$z_0 = 0$ mm with initially uniform zero phase profile (plane wave) in order to produce two distinct target intensity profiles (Fig. 2.7(a,b)) at the image plane at $z_i = 50$ mm, where the z -axis represents the optical axis. These two target profiles in the shape of a cross and of our university logo were represented on a Cartesian grid in a circular shape with a diameter of 53 mm. Equally spaced grid points were used with a nearest-neighbor distance of 0.53 mm. The incident beam was measured by scanning its intensity in the empty channel (see Fig. 2.8(b)) and was found to have a slightly asymmetric Gaussian profile with the widths of 13.4 and 16.6 mm along the x' and y' axes, respectively, which are rotated by 0.10 rad with respect to the x and y -axis of the optical system. These parameters were then used for calculating the profile of the phase plates explained below.

The required phase deformation of the collimated incident beam at z_0 was calculated using the Gerchberg-Saxton (GS) iterative algorithm [48]. This algorithm determines the phase of the optical wave function in the imaging system, whose intensity in the diffraction and the image plane of the system are known. The method typically assumes a Fourier Transform relation between the optical fields on both planes. Therefore, in order to move the image plane from far-field to a finite distance from the diffraction plane we considered a propagation function that linked the optical fields on both planes based on the Huygens principle. In this spirit the wavefront on the diffraction plane at z_0 , E^d , was represented as point emitters of spherical wavelets with respective coordinates (x, y) , amplitude $A_{(x,y)}$ and phase angle $\varphi_{(x,y)}$. The optical field on the image plane, E^i , was then calculated by summing up all contributions from every point emitter on (x, y)

for every point (x', y') of the grid on the distant image plane as:

$$E_{(x,y)}^d(x', y') = \frac{A_{(x,y)}}{r_{(x,y),(x',y')}} e^{-i\mathbf{k}\mathbf{r}_{(x,y),(x',y')} + i\varphi_{(x,y)}},$$

$$E_{(x',y')}^i = \sum_{(x,y)} E_{(x,y)}^d(x', y') [1 + \cos(\Omega)], \quad (2.37)$$

where \mathbf{r} represents the vector between the two points on different planes, \mathbf{k} is the wave vector and Ω is the angle between the normal of the diffraction plane and the vector \mathbf{r} . Eq. (2.37) corresponds to the Fresnel-Kirchhoff diffraction formula [49]. Due to the loss of the amplitude information of the optical field profiles during the GS algorithm, the pre-factors in Eq. (2.37) were left out. Note also that the part in square brackets represents the Fresnel inclination factor.

As the GS algorithm utilizes a subsequent back and forth propagation of the beam, the roles of the image and diffraction planes at z_i and z_0 , respectively, were interchanged in Eq. (2.37). We note that the reverse propagation requires the change of the sign in the exponent in Eq. (2.37).

Fig. 2.7(c,d) shows the calculated intensity profiles in the image plane for two targets after the first iteration step of the algorithm. Compared to the results after the final convergence of the algorithm (Fig. 2.7(e,f)), which is caused by the calculated beam phase deformation shown in Fig. 2.7(g,h) as grayscales, it can be seen that already the first iteration step produces reasonable intensity profiles. It should be noted here that the loss of the 4-fold symmetry of the phase profile in Fig. 2.7(g) is caused by the incident beam with a rotated asymmetric Gaussian shape described above. The calculated mean square deviations, shown in Fig. 2.7(i,j), demonstrate that final convergence of the GS algorithm is reached after about ~ 100 iterations which take about 4 hours of computer time on a commercial laptop. Analyzing the evolution of the errors with increasing iteration steps, we note that the relative improvement is rather small. This fact is due to a large amount of zero intensity points in the target, which masks the advancement of the image.

Based on the calculated phase profiles shown in Fig. 2.7(g,h) as grayscales, two optical elements (presented in Fig. 2.8(c)), corresponding to the two targets, were modeled by using the formula $z_{(x,y)} = \varphi_{(x,y)} \lambda_0 / [(\text{Re}(n) - 1)2\pi]$ to calculate the thickness of the optical elements at transverse positions (x, y) in order to achieve the correct phase-shift profile. The refractive index $n = 1.52 + 0.05i$ of polylactide (PLA) - the plastic filament of the commercial additive 3D-printer - was measured in a separate experiment at the operating wavelength. This material was used to print the elements using a commercially available 3D-printer with a nozzle diameter of 0.4 mm and spatial resolution of 0.1 mm. We calculated that in the case of the printed phase plates the complex refractive index n would lead to about 6 % of absorption and in addition 5 % of reflection at 140 GHz.

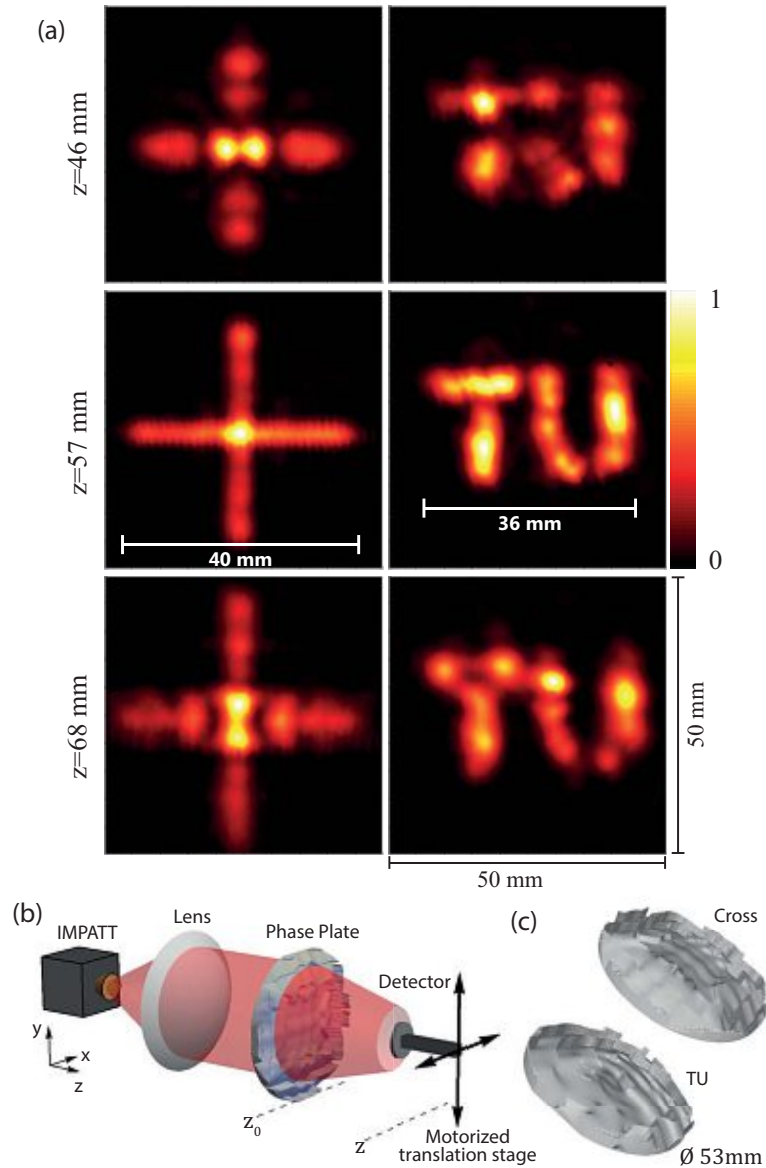


Figure 2.8: (a) Experimental intensity profiles of the optical field produced by an incident THz beam that was phase modulated by the two printed elements. The images appeared the sharpest at $z = 57$ mm. (b) Scheme of the optical setup used for measuring the intensity profiles of the field behind the printed phase plates that were fabricated according to the computer models shown in (c).

The printed elements were positioned into the path of the 140 GHz beam at the z_0 -value of the optical system as shown in Fig. 2.8(b). The incident beam was produced by an IMPATT diode with 30 mW power. The transverse intensity profile of the phase-modulated optical field behind the phase plates was then measured using a pyroelectric detector on a translator in the xy -plane with a scanning resolution of 0.5 mm and scan-

ning region size of $50 \times 50 \text{ mm}^2$. A sufficient signal-to-noise ratio was achieved by the implementation of a lock-in detection system. A sequence of intensity profiles was measured at various positions around the set image plane position z_i . In Fig. 2.8(a) we present the measured intensity profiles at three different positions z . We found that the sharpest images, which were the closest to the simulated profiles in Fig. 2.7(e,f), were located at $z = 57 \text{ mm}$, slightly deviating from the expected distance of 50 mm . Simultaneously, the effective shape size of the images is also increased compared to respective target images shown in Fig. 2.7(e,f) by approximately 10 %.

In order to find the reason for the variation of image size, we investigated the influence of the phase distribution of the incident beam. Indeed, in the real experiment, the phase profile of the beam deviates from an ideal plane wave and is better approximated with a spherical beam with a large but yet unknown curvature R . Assuming a finite wavefront radius for the phase part of the optical field of the Gaussian incident beam causes a displacement of the image plane at which the shape of the intensity profile appears the sharpest. In addition, the size of the image increases proportionally to the change in the optimal distance (see Fig. 2.9(b,c)).

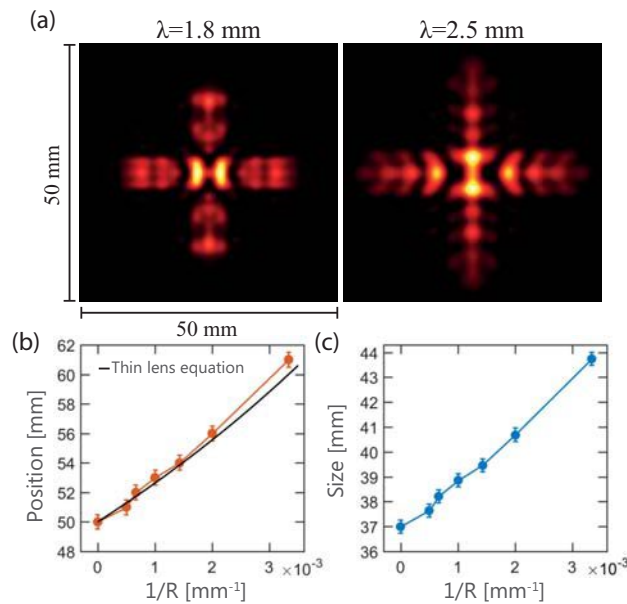


Figure 2.9: (a) Simulated intensity profiles of the optical wave function at the image plane, where the wavelength was set to 1.8 and 2.5 mm, respectively, and the incident beam was modulated by the waveplate in Fig. 2.7(g), optimized for $\lambda = 2.14 \text{ mm}$. (b,c) Position and size of the image as a function of the wavefront curvature (R^{-1}) of the incident beam including the values from Fig. 2.7, where $R = \infty$. Points mark the results from the simulations, the solid black line represents the thin lens formula with a focus set at $z_i = 50 \text{ mm}$.

For each value of R a set of intensity profiles at various positions z with a step size of $\Delta z = 1$ mm was simulated. From it, we were able to select the position z , at which the shape in the simulated intensity profile appeared focused, for each value of R (see Fig. 2.9(b)). Fig. 2.9 also shows that the dependence of image plane position on R coincides with the simple thin lens equation with the focus of z_i (depicted in black), in particular in the linear regime of the equation ($\frac{R}{z_0} \gg 1$). Effective sizes of the sharpest shapes in respect with R , shown in Fig. 2.9(c), follow the same trend as their positions. This may be expected as a result of linear dependence between the image plane position of the sharpest image and its position on the optical axis. For $R = 500$ mm we see in Fig. 2.9(b) that the sharpest image appears at $z = 56$ mm, relatively close to the position of the sharpest measured image in Fig. 2.8(a). In addition, the effective size of the sharpest image for $R = 500$ mm is comparable to the measured one and thus shows that an uncollimated beam with a similar curvature explains well the mismatch of the theoretical prediction and the experimental results, despite our optimization of the optical system.

We also investigated the effect of varying the wavelength of the incoming beam, while keeping the phase plate fixed to the one producing the cross-shaped intensity pattern (see Fig. 2.7(g)). Simulated intensity profiles at the image plane z_0 for two wavelengths around the value λ_0 are shown in Fig. 2.9(a). After comparing these results to Fig. 2.7(e) we conclude that a noticeable change of wavelength still produces intensity profiles that preserve the basic shape of the target yet it also shows that a specific spectral width of the radiation would influence the sharpness of the image.

We also mention parenthetically that we improved the propagation function in Eq. (2.37) by better taking into account the finite thickness of the phase plate. Instead of an instant change of the propagation phase (as for a waveplate with zero thickness), a finite height has been added to each emitter of the source plane with a value corresponding to the actual thickness at a point (x,y) . This improvement slightly corrected the simulated intensity profiles when compared to real results, yet the changes are barely seen directly and are therefore not shown here.

3. Electron Dynamics in a Two-Dimensional Crystal

Using precise epitaxial growth methods, semiconductor hetero-structures can be fabricated with few nanometer-thin layers. Combining layers of various materials with different electronic structures, bandgaps, and lattice constants can result in a potential well, which hosts electrons in a very narrow region in the direction perpendicular to the growth direction. The latter is often referred to as a two-dimensional electron gas.

In the following chapters, we will experimentally observe how the investigated samples, i.e., strained HgTe films, respond to applied magnetic and electric fields. These samples can be modeled as a system consisting of an insulating slab with a metallic film on top. In the previous chapter, we have formulated relations between the complex transmission of such a model and the 2D conductivity of the 2D metallic film. In this chapter, we will dive through the theoretical picture of a 2D crystal in electromagnetic fields, which will in turn allow us to connect the fundamental properties of the electronic configuration with the conductivity of the system.

We will begin with a fully classical description of an electron in a magnetic and electric field, which, in fact, does not quantitatively describe a realistic situation. The shortcoming of a fully classical approach will be corrected by applying a semiclassical model, which effectively includes the effect of the crystal structure. The latter will be followed up by a fully quantum mechanical description of electrons in magnetic fields, which will later in this thesis allow us to experimentally probe the concentrations of the active charge carriers.

3.1 The Drude Model

Three years after J.J. Thompson discovered the electron in 1897, P. Drude presented a theory of metallic conduction, which is still used today as a practical way to describe certain metallic compounds. Drude applied the kinetic theory of gases to metals, treating the mobile valence electrons (conduction electrons) as billiard balls, while the positive metallic ions play the role of immobile positive particles [14, 50]. Between collisions, the electron-electron and electron-ion interactions are neglected. These are known as the independent electron and the free electron approximations, respectively. Therefore, in the presence of electromagnetic fields, each electron with a mass of m and charge e behaves according to Newton's laws. The Drude model very loosely describes the

details of the collision events of an electron. All collisions are described by a single relaxation time τ which represents the average traveling time of an electron between scattering events, regardless of whether the scattering occurs on the underlying lattice, other electrons, the impurities, or a combination of all of the above. The equation of motion of a classically treated electron in a magnetic field \mathbf{B} and electric field \mathbf{E} is therefore as follows [14]:

$$m \frac{d\mathbf{v}}{dt} = -e(\mathbf{E} + \mathbf{v} \times \mathbf{B}) - \frac{m\mathbf{v}}{\tau} \quad (3.1)$$

On the right side of the equation, the first term represents the Lorentz force and the second is the damping term. The equation above can provide solutions for many systems with various forms of external conditions.

3.1.1 Two-Dimensional Electron Gas

Let us consider a specific situation in which the electrons are bound to two dimensions (xy -plane), with a constant magnetic field \mathbf{B} pointing in the z -direction. A plane electromagnetic wave with an angular frequency ω propagates parallel to \mathbf{B} , which is also known as the Faraday geometry. As presented in Section 2, an electromagnetic wave results in an oscillating $\mathbf{E}_{ext} = \mathbf{E}_{ext}(x, y)e^{-i\omega t}$ in the xy -plane. The wavelength λ of such wave is assumed to be much larger than the electronic mean free path, so the resulting force is uniform in space. This is surely the case when investigating metallic compounds with submillimeter radiation. From the experimental results gathered in this thesis, one can estimate that λ is larger by an order of $\sim 10^{20}$. Maxwell's theory shows that \mathbf{E} has to be accompanied by a perpendicular oscillating magnetic field. The magnetic contribution of the electromagnetic wave can be ignored due to two reasons: a) In realistic condition the amplitude of the magnetic field of an electromagnetic wave is negligible compared to B_0 , and b) The forces resulting from the oscillating magnetic field are by the factor of v/c smaller than the electric forces. These conditions are specifically selected since they effectively represent the experimental work described in detail below. The total electric field is $\mathbf{E} = \mathbf{E}_{ext} + \mathbf{E}_{int}$, where \mathbf{E}_{int} is the electric field induced by all other electrons, which also oscillates harmonically and, thus, $\mathbf{E} = \mathbf{E}(x, y)e^{-i\omega t}$.

The solution for the differential equation Eq. (3.1) can be found by setting $\mathbf{v} = \mathbf{v}(x, y)e^{-i\omega t}$, where $\mathbf{v}(x, y)$ is a constant complex vector. We obtain:

$$\left(\frac{1}{\tau} - i\omega\right)\mathbf{v}(x, y) - \frac{e}{m}\mathbf{v}(x, y) \times \mathbf{B} = \frac{e}{m}\mathbf{E}(x, y). \quad (3.2)$$

Without losing the generality, we can choose that $\mathbf{E} = \mathbf{E}(x)$. We can represent \mathbf{v} as a combination of two orthogonal projections on the axes parallel and perpendicular to $\mathbf{E}(x)$ (see Fig. 3.1):

$$\mathbf{v}(x, y) = \mathbf{v}_x + \mathbf{v}_y. \quad (3.3)$$

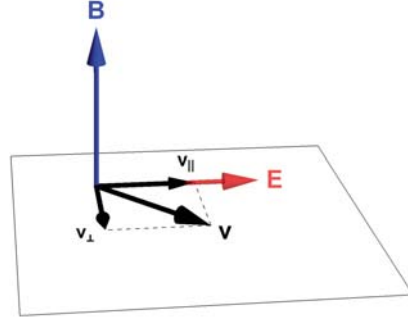


Figure 3.1: An illustration of the 2D system with \mathbf{E} , \mathbf{B} and \mathbf{v} .

This allows to obtain the following system of linear equations:

$$\begin{aligned} \left(\frac{1}{\tau} - i\omega\right)v_x - \Omega_c v_y &= \frac{e}{m}E, \\ \left(\frac{1}{\tau} - i\omega\right)v_y + \Omega_c v_x &= 0, \end{aligned} \quad (3.4)$$

where:

$$\Omega_c = \frac{eB}{m} \quad (3.5)$$

is the cyclotron frequency, i.e., the angular frequency of revolution of a free electron in magnetic field. If n_{2D} electrons per unit area move with a velocity of \mathbf{v} , they represent a flow of charge described by the vector of current density $\mathbf{j}_{2D} = -en_{2D}\mathbf{v}$, which is, in this specific case, defined in two dimensions. The reader should note here that in a metal the electrons always move in various directions with various velocities and thus \mathbf{v} is, in this case, the average electronic velocity. If the electric field is absent, all directions are equally probable and \mathbf{v} and \mathbf{j} equal zero. Let us continue by expressing the relation between two orthogonal projections of \mathbf{j} in respect to E :

$$\begin{aligned} j_x &= \sigma_{xx}E; & \sigma_{xx} &= \sigma_0 \frac{1 - i\omega\tau}{(1 - i\omega\tau)^2 + (\Omega_c\tau)^2}; \\ j_y &= \sigma_{xy}E; & \sigma_{xy} &= \sigma_0 \frac{\Omega_c\tau}{(1 - i\omega\tau)^2 + (\Omega_c\tau)^2}. \end{aligned} \quad (3.6)$$

Here, $\sigma_0 = ne^2\tau/m$ represents the Drude DC conductivity in the absence of the magnetic field. With a simple derivation, one can generalize the above expressions with the help of the 2D conductivity tensor $\hat{\sigma}$:

$$\mathbf{j} = \hat{\sigma}\mathbf{E} = \begin{pmatrix} \sigma_{xx} & \sigma_{xy} \\ -\sigma_{xy} & \sigma_{xx} \end{pmatrix} \begin{pmatrix} E_x \\ E_y \end{pmatrix}. \quad (3.7)$$

The equation above, without the specific form of the conductivity tensor, is also known

as the vector notation of Ohm's law, which we met already in Chapter 2 (Eq. (2.3)). The structure of the conductivity tensor with identical diagonal components and opposite off-diagonal components comes from the rotational invariance of the system. The off-diagonal components are also responsible for the well known Hall effect [51], a current flows as a consequence of two orthogonal vectors: the electric and magnetic field.

Additional information can be extracted from σ_{xy} . Assuming that the directions of fields and currents are known, it is possible to obtain the sign of the active charge carrier e . And surprisingly, in some compounds, such as Be, Mg, or Al, the charge carriers turn out to have a charge opposite to that of an electron. The latter certainly does not fit in the current description of an electrically neutral metal, i.e., a sea of conducting negatively charged electrons, on top of immobile ions. However, the explanation can be found if we disregard the free-electron approximation and, instead, look for a solution with the quantum mechanical description of solids. It shows, in fact, that the charge of an electron remains the same. However, the effective mass is not anymore limited to only positive values. This will be tackled in the following chapter.

3.2 The Semiclassical Model

The semiclassical model joins the classical Drude approach we described in Section 3.1 with the quantum mechanic description of electrons as Bloch states. In this model, the interaction of the electrons with the external fields is treated classically, while the interaction with the periodic field of the ions is treated quantum mechanically. While the classical approach was described above, the Bloch theory needs to be briefly presented in order to obtain the right tools that will allow us to continue with the semiclassical model.

3.2.1 Bloch Theory

Before we dive into the quantum mechanical addition to our model, let us quickly summarize the main results of the Bloch theory [14], which is the central approach to describe electrons in solids. It states that in a periodic potential $U(\mathbf{r})$, such as the one caused by the crystal lattice, the solutions to the Schrödinger equation are found in a form of plane waves modulated by a periodic function. These wave functions are called Bloch states and have a mathematical form of:

$$\psi_{l\mathbf{k}}(\mathbf{r}) = e^{i\mathbf{k}\mathbf{r}} u_{l\mathbf{k}}(\mathbf{r}); \quad u_{l\mathbf{k}}(\mathbf{r} + \mathbf{R}) = u_{l\mathbf{k}}(\mathbf{r}). \quad (3.8)$$

Here, the wave function $\psi(\mathbf{r})$ describes an electron with a band index l and a Bloch wavevector \mathbf{k} ; and $u_{l\mathbf{k}}(\mathbf{r})$ is a corresponding periodic function with the same periodicity \mathbf{R} as the crystal lattice. For each l , the Bloch vectors \mathbf{k} are restricted to the first Brillouin zone (BZ), the Wigner-Seitz primitive cell in the reciprocal lattice. Inserting the Bloch

states into a time-independent Schrödinger equation gives:

$$\begin{aligned}\hat{H}\psi_{l\mathbf{k}}(\mathbf{r}) &= \left(\frac{-\hbar^2}{2m}\Delta^2 + U(\mathbf{r}) \right) \psi_{l\mathbf{k}}(\mathbf{r}) = \epsilon_{l\mathbf{k}}\psi_{l\mathbf{k}}(\mathbf{r}), \\ \hat{H}u_{l\mathbf{k}}(\mathbf{r}) &= \left(\frac{\hbar^2}{2m}(-i\Delta + \mathbf{k})^2 + U(\mathbf{r}) \right) u_{l\mathbf{k}}(\mathbf{r}) = \epsilon_{l\mathbf{k}}u_{l\mathbf{k}}(\mathbf{r}).\end{aligned}\quad (3.9)$$

This provides the basic concept of an electronic band structure; the eigenvalues $\epsilon_{l\mathbf{k}}$ represent the electronic levels or energy bands in a crystal structures, which are characterized by two quantum numbers: the Bloch wave vector \mathbf{k} and the band index l . In fact, the electronic levels depend continuously on the parameter \mathbf{k} , therefore $\epsilon_{l\mathbf{k}} = \epsilon_l(\mathbf{k})$ and have the property or periodicity in the reciprocal lattice: $\epsilon_{l\mathbf{k}}(\mathbf{k} + \mathbf{K}) = \epsilon_{l\mathbf{k}}(\mathbf{k})$.

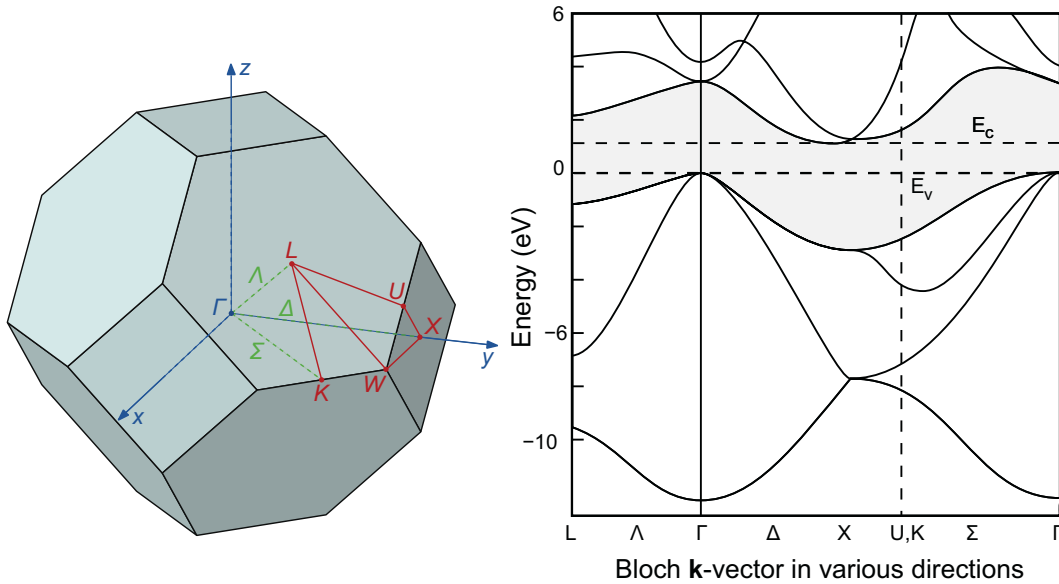


Figure 3.2: Band structure of silicon. Left: The first Brillouin zone of silicon with a diamond structure. Right: Result of the band structure calculation [52]. The figures are based on Refs. [53, 54].

Real compounds have typically several electrons per unit cell. According to the Pauli exclusion principle, since electrons are fermions (particles with a half-integer spin), there can only be one electron per quantum state. The number of quantum states is infinite but discrete. Although we have said that the energy levels continuously depend on \mathbf{k} , for a finite crystal there is only a finite number of available \mathbf{k} -vectors for each band. This follows from the fact that each particle occupies a volume of $\Delta k = (2\pi)^d/V$ in the reciprocal k -space, where d corresponds to the space dimensionality of the system and V is the volume of a lattice primitive cell. The second discrete quantum number is the band index l , which is an infinite set of discrete values. Additionally, the spin of the electron serves occasionally as the third quantum number. Assuming a spin-degenerate

electronic band, each state can be occupied by two electrons, one with a spin up and one with a spin down. The ground state of the many-body system is obtained by filling states with the lowest possible energy. The last occupied level with the highest energy is referred to as the Fermi level (or Fermi energy) ϵ_F . The latter holds true for a zero temperature system. When we are dealing with finite temperatures, the distribution of electrons over energy levels in a system is described by the Fermi-Dirac function:

$$f_0(\mathbf{k}) = \frac{1}{1 + e^{\frac{\epsilon_l(\mathbf{k}) - \mu}{k_b T}}}, \quad (3.10)$$

where k_b is the Boltzmann constant, T the absolute temperature and μ is the chemical potential. In the limit of near to zero temperatures, the distribution function can be approximated by the Heaviside function and $\epsilon_F = \mu(T = 0)$. With the help of the Fermi-Dirac function, we can obtain the density of electrons in an energy band l in two ways:

$$n_l = \frac{N}{V} = \int_0^\infty g_l(\epsilon) f_0(\epsilon) d\epsilon = \int_{l, BZ} D_l f_0(\mathbf{k}) \frac{d\mathbf{k}}{(2\pi)^d}, \quad (3.11)$$

where $g_n(\epsilon)$ represents the density of states (DOS) of the band l , i.e., the number of states which may be occupied in a certain energy interval in this band. Degeneracy $D_l = D_s D_v$ corresponds to the spin (s) and/or valley (v) degeneracy factor of the band. Valley degeneracy comes from the fact that multiple equivalent constant energy surfaces can be found in the first BZ and for a spin degenerate band $D_s = 2$.

Bloch's theory introduced the wavevector \mathbf{k} , which should not be confused with the wavevector \mathbf{k}_S in the Sommerfeld model (free electron model), where the electron momentum equals $\mathbf{p} = \hbar\mathbf{k}_S$. Bloch wavefunctions are not eigenstates of the momentum operator \hat{p} :

$$\hat{p}\psi_{n\mathbf{k}}(\mathbf{r}) = \frac{\hbar}{i}\nabla\psi_{n\mathbf{k}}(\mathbf{r}) = \frac{\hbar}{i}\nabla(e^{i\mathbf{k}\mathbf{r}}u_{n\mathbf{k}}(\mathbf{r})) \neq \hbar\mathbf{k}\psi_{n\mathbf{k}}(\mathbf{r}). \quad (3.12)$$

Instead, $\hbar\mathbf{k}$ is the crystal momentum. The evolution of the electrons momentum is governed by all forces on the electron, while the electron's crystal momentum is given by all external forces, except the periodic field of the lattice. In fact, the Bloch state represents a wavepacket, which is a superposition of a set of plane waves for which it is possible to obtain the average velocity in a particular energy level l as:

$$v_l(\mathbf{k}) = \frac{1}{\hbar} \frac{\partial \epsilon_l(\mathbf{k})}{\partial \mathbf{k}}. \quad (3.13)$$

While one should always be aware of what \mathbf{k} and \mathbf{v} truly represent, we will, from this point on, sometimes refer to the group velocity of the wavepacket simply as the electron velocity. The external force on an electron wavepacket with \mathbf{k} equals $\mathbf{F} = \hbar\dot{\mathbf{k}}$, which

allows us to write:

$$\dot{\mathbf{v}}_l(\mathbf{k}) = \frac{1}{\hbar} \frac{\partial^2 \epsilon_l(\mathbf{k})}{\partial \mathbf{k} \partial t} = \frac{1}{\hbar} \frac{\partial^2 \epsilon_l(\mathbf{k})}{\partial \mathbf{k}^2} \dot{\mathbf{k}} = \frac{\mathbf{F}}{m^*}, \quad (3.14)$$

where

$$\frac{1}{m^*} = \frac{1}{\hbar^2} \frac{\partial^2 \epsilon_l(\mathbf{k})}{\partial \mathbf{k}^2}, \quad (3.15)$$

is the effective mass, which is a tensor for anisotropic bands. We will see how useful this becomes at the end of this chapter.

From this point on and throughout this thesis, we will assume we are in the limit of very low temperatures. In this case, the Fermi-Dirac function becomes a Heaviside function and the current density equals:

$$\mathbf{j} = -en_l \mathbf{v}_l = -\frac{eD_l}{\hbar^2 (2\pi)^d} \int_{BZ} \left(d\mathbf{k} \frac{\partial(\epsilon_l(\mathbf{k}))}{\partial \mathbf{k}} \right) \Bigg|_{\epsilon_l(\mathbf{k})=\epsilon_f}, \quad (3.16)$$

showing that solely electrons at the Fermi level contribute in transport. The latter is of particular importance since it shows that the position of the Fermi energy is crucial for the optical and electrical properties of a crystal. If the Fermi energy is within a band or several bands, the energy of the electrons around the Fermi level can be increased with external fields due to the vacant states nearby. In this case, the crystal is a conductor. If we are dealing purely with only occupied and empty bands and the Fermi energy is located in a bandgap between the top filled band (the valence band) and the next vacant band (the conduction band), the material is an insulator or a semiconductor, depending on the size of the bandgap. Although the distinction between insulators and semiconductors is somewhat blurry, the common understanding is that due to the smaller bandgap in the case of semiconductors (see Fig. 3.2 for example), the "conducting" state can be conveniently reached. Changing the position of the Fermi level can be achieved by altering the density of electrons externally by gating or photo-illumination [55]. It can be also achieved internally by doping the crystal with other atoms in fabrication. Consequently, the versatility and adaptability have made semiconductors crucial for the industry of electronics.

3.2.2 Validity of the Semiclassical Model

To join the quantum mechanical arguments and the classical treatment of the electron in external fields, both, the position of the electron \mathbf{r} and its momentum $\hbar\mathbf{k}$ need to be accurately specified, without the violation of the uncertainty principle $\Delta r \Delta k > 1$.

Bloch wave functions are plane waves modulated by a periodic function and are characterized with a definite value of a \mathbf{k} -vector. The characteristic coordinate \mathbf{r} , however, is not fully defined. This has to be corrected in order to evaluate the uncertainty of position

Δr . The latter can be achieved if we consider a wave packet of Bloch electrons [14,56], where we sum up Bloch waves over a small interval Δk compared to the dimensions of the BZ. The spread of the wave packet corresponds to the Δr and has to be smaller than the mean free path r_0 of the corresponding electrons for an accurate assessment of r . Since the typical k is of the order of the inverse lattice constant $1/a$, we obtain with the help of the uncertainty principle:

$$\frac{1}{a} \sim k > \Delta k > \frac{1}{\Delta r} > \frac{1}{r_0}. \quad (3.17)$$

From here it follows that the position of the wave packet can be defined accurately if $r_0 > \Delta r$ and more importantly $r_0 \gg a$. It is obvious to claim, that the response of the electrons to the external fields can be described classically if the applied electric or magnetic fields vary very slowly in comparison to the spread of the wave packet and consequently even slower compared to the lattice constant. Fig. 3.3 shows a schematic presentation of the conditions that need to be satisfied in order for the semiclassical model to be valid.

To summarize, in the semiclassical model, applying external fields results in ordinary classical forces in the equation of motion of the wave packet. While the external fields are treated classically, the potential of the crystal lattice with a lattice constant smaller than the spread of the wavepacket is considered quantum mechanically.

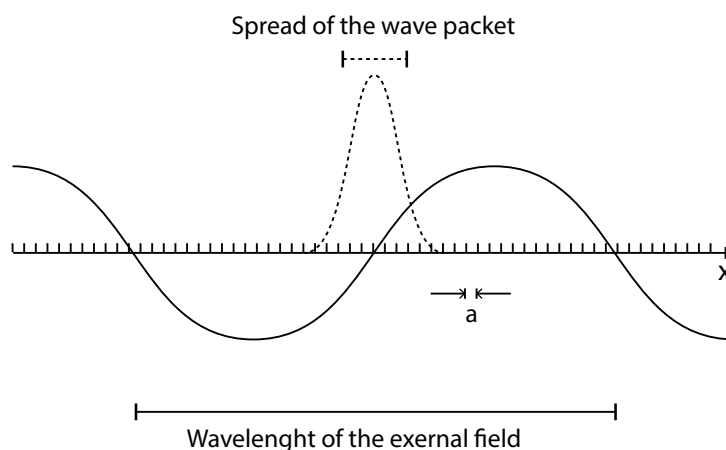


Figure 3.3: Scheme of the system for which the semiclassical approach is valid. The applied field varies slowly over the spread of the Bloch wave packet, where the latter is much larger than the lattice constant a .

The semiclassical model can now be used to determine the evolution of the position r and wavevector k of an electron (wave packet) in external electric and magnetic field. Here, we assume that the band structure of the compound is known. Each electron is characterized with a position r , wavevector k and a band index l . The equations of motion that determine the time evolution of the position and wavevector are the follow-

ing [14]:

$$\dot{\mathbf{r}} = \mathbf{v}_l(\mathbf{k}) = \frac{1}{\hbar} \frac{\partial \epsilon_l(\mathbf{k})}{\partial \mathbf{k}} \quad (3.18)$$

$$\hbar \dot{\mathbf{k}} = -e (\mathbf{E} + \mathbf{v}_l(\mathbf{k}) \times \mathbf{B}) \quad (3.19)$$

It is important to mention some additional assumptions or restrictions of the system, specifically in connection to the amplitudes of the applied fields. In the semiclassical model, the band index is a constant of motion, therefore the model ignores interband transitions. The energy of the electrons, when fields are applied, should not raise above the energetic limits of the corresponding band. In fact, these two conditions must be satisfied [14]:

$$eEa \ll \frac{\epsilon_{gap}(\mathbf{k})^2}{\epsilon_F}, \quad (3.20)$$

$$\hbar \Omega_c \ll \frac{\epsilon_{gap}(\mathbf{k})^2}{\epsilon_F}, \quad (3.21)$$

where $\epsilon_{gap}(\mathbf{k})$ is the size of the energy gap between $\epsilon_l(\mathbf{k})$ and the nearest band $\epsilon_{l\pm 1}(\mathbf{k})$ at a specific \mathbf{k} , and Ω_c is the cyclotron frequency, which is going to be described in the sections below. In practice, the first condition is quite difficult to break, while the second has to be generally treated a bit more carefully. Additionally, it should be pointed out that the angular frequency ω of the electromagnetic radiation must satisfy:

$$\hbar \omega \ll \epsilon_{gap}, \quad (3.22)$$

otherwise, single-photon excitation could cause an interband transition.

In connection with the Drude picture above, it is beneficial to discuss the collisions in the Bloch theory. The solutions of the Schrödinger equation within the Bloch theory are stationary waves in the presence of the periodic potential of the ions. We cannot assign the fixed periodic lattice of ions to be the source of scattering, since the electron-ion interaction has been fully introduced in the Bloch theory. In a model of a perfectly periodic crystal, the velocity of electrons persists forever, resulting in a metallic crystal having an infinite conductivity. However, that is surely not the case in nature. Every crystal has imperfections, such as impurities, defects, thermal vibration of ions (phonons), etc. And these perturbations of the periodicity are the source of the electronic scattering, introduced in Sec. 3.1 as the electronic relaxation time τ .

3.2.3 The Effective Cyclotron Mass

In this section, we are going to describe what happens with electrons in an electronic band, when a constant magnetic field is applied. We will discover soon the importance of the crystal structure on the effective outcome of the electron parameters, to be specific, the electron effective mass. The following serves as a crucial part of the technique to

experimentally obtain the band structures of 2D films, as will be shown later in this thesis. Let us begin by considering the semiclassical equations in an uniform magnetic field:

$$\hbar \dot{\mathbf{k}} = -e(\mathbf{v}_l(\mathbf{k}) \times \mathbf{B}), \quad (3.23)$$

$$\dot{\mathbf{r}} = \mathbf{v}_l(\mathbf{k}) = \frac{1}{\hbar} \frac{\partial \epsilon_l(\mathbf{k})}{\partial \mathbf{k}}. \quad (3.24)$$

One can notice that the component of \mathbf{k} along the direction of the applied magnetic field \mathbf{B} is a constant in time. Moreover, these equations show that in the reciprocal space, electrons move in orbits, similar to what we discovered in Section 3.1 in real space. However, here, the orbits are constrained to the intersection of the surface defined by the $\epsilon_l(\mathbf{k})$ and the plane perpendicular to the magnetic field as seen in Fig. 3.4. It can be easily seen in the equations above, that the direction of orbiting is fully determined by the gradient of $\epsilon_l(\mathbf{k})$ in the k -space. We will continue by exploring a very crucial and important consequence of this relation.

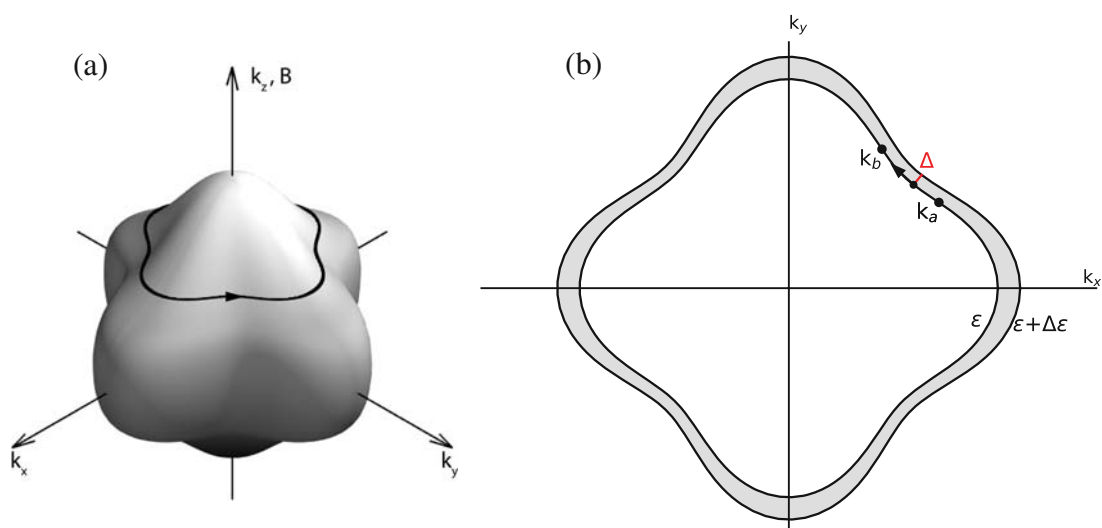


Figure 3.4: (a) Orbit of motion in k -space at some value of k_z , defined by the intersection between the surface of constant energy ϵ and a plane perpendicular to the applied field \mathbf{B} . The direction of motion is determined by the gradient of $\epsilon_n(\mathbf{k})$. In this specific case the states inside the enclosure have lower energy than the states outside of the object. (b) The intersection from (a) in $k_x k_y$ -plane with the addition of the orbit corresponding to $\epsilon + \Delta\epsilon$. See text for details.

Let us investigate the time an electron needs to travel around a certain part of an orbit at a constant values of energy ϵ and k_z , where the latter corresponds to the component of the wavevector \mathbf{k} in the direction of the applied magnetic field. We are also considering a single electronic band, therefore we are able to omit the band index l . The time needed

to span a part of the orbit between \mathbf{k}_a and \mathbf{k}_b equals:

$$t_{ab} = \int_{\mathbf{k}_a}^{\mathbf{k}_b} \frac{d\mathbf{k}}{|\dot{\mathbf{k}}|} = \frac{\hbar^2}{eB} \int_{\mathbf{k}_a}^{\mathbf{k}_b} \frac{d\mathbf{k}}{|(\partial\epsilon/\partial\mathbf{k})_{\perp}|}, \quad (3.25)$$

where we used the relations Eqs. (3.23) and (3.24) in order to rewrite $\dot{\mathbf{k}}$, and $(\partial\epsilon/\partial\mathbf{k})_{\perp}$ is the component of the gradient perpendicular to the applied field. We define a vector $\Delta(\mathbf{k})$, which is perpendicular to the orbit and connects the point \mathbf{k} with the other orbit corresponding to the energy $\epsilon + \Delta\epsilon$ (see Fig. 3.4(b)). At small values of $\Delta\epsilon$, we can write:

$$\Delta\epsilon = \left| \left(\frac{\partial\epsilon}{\partial\mathbf{k}} \right)_{\perp} \right| \Delta(\mathbf{k}), \quad (3.26)$$

where the absolute value of the gradient comes from the fact that $(\partial\epsilon/\partial\mathbf{k})_{\perp}$ and $\Delta(\mathbf{k})$ are parallel. Rewriting Eq. (3.25) results in:

$$t_{ab} = \frac{\hbar^2}{eB} \frac{1}{\Delta\epsilon} \int_{\mathbf{k}_a}^{\mathbf{k}_b} \Delta(\mathbf{k}) d\mathbf{k}. \quad (3.27)$$

Here, it should be noted that in terms of full generalization, the electronic orbits in k -space can in some cases be open curves (not closed orbits). This happens when a Fermi surface connects with a Fermi surface from the neighboring BZ. However, such situations are out of scope for this work and an avid reader can find more information in Ref. [14]. In the case of closed orbits, however, \mathbf{k} can perform a full revolution around the orbit, for which $\mathbf{k}_a = \mathbf{k}_b$. The integral in Eq. (3.27) gives the area between the orbits at energies ϵ and $\epsilon + \Delta\epsilon$ (gray area in 3.4(b)). Moreover, if we set $\Delta\epsilon \rightarrow 0$ and define A as the area in k -space enclosed by the orbit of constant energy ϵ at some k_z , we obtain for the time period of the orbit:

$$T = \frac{\hbar^2}{eB} \frac{\partial A(\epsilon, k_z)}{\partial \epsilon}. \quad (3.28)$$

Let us continue by rewriting Eq. (3.23) with the help of the $\mathbf{v} = \dot{\mathbf{r}} = d\mathbf{r}/dt$ and $\dot{\mathbf{k}} = d\mathbf{k}/dt$:

$$\hbar d\mathbf{k} = -e(d\mathbf{r} \times \mathbf{B}). \quad (3.29)$$

This relation in fact shows us that the orbit in real space is similar to the one in k -space, only rotated by 90° in the plane perpendicular to \mathbf{B} and scaled by \hbar/eB . This result benefits us greatly, since it confirms that the time period of an orbit is the same in real space and allows us to use the classical result of an orbiting electron in magnetic field from Eq. (3.5):

$$T = \frac{2\pi}{\Omega_c} = \frac{2\pi m}{eB} \quad (3.30)$$

and finally defining the effective cyclotron mass:

$$m_c(\epsilon, k_z) = \frac{\hbar^2}{2\pi} \frac{\partial A(\epsilon, k_z)}{\partial \epsilon}. \quad (3.31)$$

The latter result serves as the quantum mechanical addition to the Drude model (Eq. (3.6)), incorporating the effects of the periodic lattice of the ions through the effective cyclotron mass, which can strongly diverge from the electron rest mass m_e . In two dimensions, the same conclusion can be obtained by a stricter derivation with the use of the Boltzmann transport equation, which describes the statistical behavior of the system in the state out of equilibrium [57]. Besides, this approach shows that expressing the conductivity as Eq. (3.6) is only valid if one assumes rotational symmetry of the band structure. Therefore, at some fixed k_z , the energy $\epsilon(k_x, k_y) = \epsilon(k)$, where $k = \sqrt{k_x^2 + k_y^2}$. Since for $\epsilon(k)$ the velocity \mathbf{v} is always parallel to \mathbf{k} and, according to Eq. (3.23), $\dot{\mathbf{k}}$ is perpendicular to \mathbf{k} , this condition results in circular cyclotron orbits in both, real space and k -space.

One of the impressive consequences of Eq. (3.31) is the fact that effective cyclotron mass is not limited to having only positive values. A negative gradient $\partial A/\partial E$ gives a negative effective cyclotron mass. This results in an orbital motion in the opposite direction, compared to a positive effective mass with the same absolute value, and, effectively, giving an impression of a "positively" charged carrier or hole, i.e., a carrier that behaves like an electron, but has an opposite charge.

Holes are broadly used "fictitious" particles in solid state physics. The main idea comes from the fact that a fully occupied band carries no current. If one separates the band into two sections:

$$\begin{aligned} 0 &= (-e) \int_{\text{Full Band}} D \frac{d\mathbf{k}}{(2\pi)^d} \mathbf{v}(\mathbf{k}) = \\ &= (-e) \int_{\text{Section 1}} D \frac{d\mathbf{k}}{(2\pi)^d} \mathbf{v}(\mathbf{k}) + (-e) \int_{\text{Section 2}} D \frac{d\mathbf{k}}{(2\pi)^d} \mathbf{v}(\mathbf{k}), \end{aligned} \quad (3.32)$$

one can write for the current density of a partially occupied band:

$$j = (-e) \int_{\text{Occupied}} D \frac{d\mathbf{k}}{(2\pi)^d} \mathbf{v}(\mathbf{k}) = (+e) \int_{\text{Unoccupied}} D \frac{d\mathbf{k}}{(2\pi)^d} \mathbf{v}(\mathbf{k}). \quad (3.33)$$

The latter shows that the current produced by electrons that occupy a set of levels in a band is exactly the same as the current produced if the unoccupied set of levels were occupied with holes (particles with $+e$). The benefit is found in the sense that whenever it is more convenient, one can consider that the transport is carried out by the positive holes instead of the electrons.

3.3 Landau Quantization

The present chapter started with a fully classical description, which was followed by some quantum mechanical corrections using the semiclassical model. It is therefore reasonable that the last section of this chapter focuses on a fully quantum mechanical approach to describe electrons in a magnetic field. It turns out that the resulting formulations can be used to recover carrier concentrations from the detected quantum oscillations of the density of states, which will benefit us later in Chapter 7.

We begin by stating that we often investigate crystals that have either almost empty or almost full bands. This means that the electronic states of interest often lie close to the minima or maxima at \mathbf{k}_0 of the band dispersion, allowing us to do an expansion along the x -axis using Taylor series:

$$\epsilon(k_x) = \epsilon(k_{0x}) + \frac{\hbar^2}{2m_x^*} (k_x - k_{0x})^2. \quad (3.34)$$

In the same manner, we can write the expansion along the direction of the remaining axes. Here, the effective mass defined in Eq. (3.15) allowed us to conveniently include the characteristics of the band. Note that a parabolical shape of the energy dispersion results in a constant value of the effective mass and, in general terms, m^* can be a tensor due to an anisotropic $E(\mathbf{k})$, yielding $m_x^* \neq m_y^* \neq m_z^*$. Additionally, we see that in Eq. (3.34), electrons are treated as if they were free¹, however with an effective mass. The Hamiltonian for electrons in some band can be written as:

$$\hat{H} = \left(\frac{p_x \hat{\mathbf{e}}_x}{(2m_1^*)^{1/2}} + \frac{p_y \hat{\mathbf{e}}_y}{(2m_2^*)^{1/2}} + \frac{p_z \hat{\mathbf{e}}_z}{(2m_3^*)^{1/2}} \right)^2, \quad (3.35)$$

where p_i are momentum operators in the $i = x, y, z$ -axis and the band structure configuration in various directions has been implemented via the effective masses m_1^* , m_2^* and m_3^* . We have also set $\mathbf{k}_0 = 0$ for convenience. In the xy -plane the electrons are confined to an area $L_x L_y$. Since the effects of the band structure have been included in the Hamiltonian, a solution for ψ can be found in form of a plane wave. Similar to the previous section, a constant magnetic field \mathbf{B} is directed along the z -axis, which can be expressed in terms of the magnetic vector potential as $\mathbf{B} = \nabla \times \mathbf{A}$, where we can choose $\mathbf{A} = (0, Bx, 0)$. Since the Hamiltonian is gauge invariant, one of the ways to include the effect of the field is using the Landau gauge, where $p \rightarrow p + e\mathbf{A}$, which gives:

$$H = \left(\frac{p_x \hat{\mathbf{e}}_x}{(2m_x^*)^{1/2}} + \frac{(p_y + eBx) \hat{\mathbf{e}}_y}{(2m_y^*)^{1/2}} + \frac{p_z \hat{\mathbf{e}}_z}{(2m_z^*)^{1/2}} \right)^2. \quad (3.36)$$

¹Free in terms of the Sommerfeld free-electron model [14], where the energy dispersion equals $\epsilon(\mathbf{k}) = \hbar^2 \mathbf{k}^2 / 2m$.

Since \hat{p}_y commutes with this Hamiltonian, it can be replaced by its eigenvalue $\hbar k_y$ and it follows that:

$$\begin{aligned} H &= \left(\frac{p_x \hat{e}_x}{(2m_x^*)^{1/2}} + \frac{(\hbar k_y + eBx) \hat{e}_y}{(2m_y^*)^{1/2}} + \frac{p_z \hat{e}_z}{(2m_z^*)^{1/2}} \right)^2 = \\ &= \left(\frac{p_x^2}{2m_x^*} + \frac{(\hbar k_y + eBx)^2}{2m_y^*} \right) + \frac{p_z^2}{2m_z^*} \end{aligned} \quad (3.37)$$

The components in the brackets can be recognized as the Hamiltonian of the 1D harmonic oscillator for which the Hamiltonian and its eigenvalues are:

$$H_{HO} = \frac{p^2}{2m} + \frac{1}{2} m \omega^2 x^2, \quad E_n = \hbar \omega \left(l + \frac{1}{2} \right). \quad (3.38)$$

It can be seen that we are actually dealing with an Hamiltonian of a harmonic oscillator with the minimum of the potential shifted by $x_0 = \hbar k_y / eB$. Translating the harmonic oscillator does not affect its eigenvalues, therefore the electronic energy levels of the system are:

$$E(l, B, k_z) = \frac{p_z^2}{2m_z^*} + \hbar \omega \left(l + \frac{1}{2} \right), \quad (3.39)$$

where $l = 0, 1, 2, \dots$ and $\omega = eB / (m_x^* m_y^*)^{1/2}$. In fact, in this geometry $\sqrt{m_x^* m_y^*} = m_c$ defined by Eq. (3.31), since A in the present case has a form of an ellipse. From here it naturally follows that $\omega = \Omega_c$. The available energy levels for an electron are fully quantized in the plane perpendicular to the applied magnetic field and are known as the Landau levels (LL). Due to the confinement of space, k_y can only take values of $k_y = 2\pi N / L_y$, where $N = 0, 1, 2, \dots, N_{max}$. The maximum value of integer N is limited by $x_0 \leq L_x$, which gives us the maximum number of states in a single LL:

$$N_{max} = \frac{L_x L_y eB}{h}. \quad (3.40)$$

If l LLs are filled, the 2D carrier density of the system equals:

$$n = \frac{l D N_{max}}{L_x L_y} = l D \frac{eB}{h}, \quad (3.41)$$

where D represent the degeneracy of the electronic band in zero field. The eigenvalue of p_z is continuous ($E_z = \hbar^2 k_z^2 / 2m_z^*$) if the system is unbounded in z -axis. In this work, we are going to investigate 2D films, therefore the electronic systems are confined also in the z -direction. In this case, the eigenvalues of p_z become discrete. As will be seen below, the spacing between these discrete energies E_z is much larger than $\hbar \omega$.

In the derivation above, the directions x and y have no physical differences. The derivation above can be easily accomplished by interchanging the two coordinates. It

should come as no surprise that the allowed k -values are represented by closed orbits in the k -space perpendicular to the applied field. Since the allowed k -space is quantized, this results in a splitting of the Fermi Surface into Landau tubes and the allowed orbits lie on the intersection of the tubes with a plane perpendicular to the field \mathbf{B} . An example of how a Fermi sphere splits into Landau Tubes is presented in Fig. 3.5.

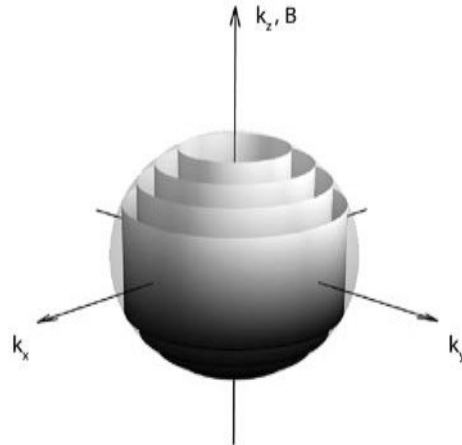


Figure 3.5: An illustration of a Fermi sphere splitting into Landau tubes when magnetic field in z -axis is applied.

Let us briefly consider the situation when the energy dispersion is not simply parabolic, which is generally the case in real compounds. We have learned that the Landau levels split the Fermi surface, whatever shape it may be. An arbitrarily shaped electronic band, however, does not necessarily result in an equally spaced set of energy levels as we have seen in a simple parabolic dispersion above. For a general solution we can use the Onsager relation [58] that states that the area A_l enclosed by the electron orbit in k -space has to be quantized:

$$A_l = (l + \gamma) \frac{2\pi e}{\hbar} B. \quad (3.42)$$

This relation is derived from the Bohr-Sommerfeld quantization, which states that for $l \gg 1$ the orbit in real space must satisfy: $\oint \mathbf{p} dr = h(l + \gamma)$, where $p = \hbar\mathbf{k} - e\mathbf{A}$ is the canonical momentum. The phase constant γ is equal $\frac{1}{2}$ for free electron, however in real metals it deviates from this value. Since the condition $l \gg 1$ needs to be satisfied, γ can easily be neglected. Since there is a large filling of Landau levels, a small change in B will change the number of occupied Landau levels by $\Delta l \gg 1$. Moreover, a large set of Landau tubes, with a very narrow spacing between them ($\hbar\omega \ll \epsilon_F$), effectively map out the Fermi energy surface at zero magnetic field and therefore dE/dA_l does not depend on B . For example, imagine that in Fig. 3.5, the number of LL would be 100

instead of 4. We can write:

$$\frac{dE}{dl} = \frac{dE}{dA_l} \frac{dA_l}{dl} = \frac{dE}{dA_l} \frac{2\pi e}{\hbar} B = \frac{e\hbar}{m_c} B = \hbar\omega, \quad (3.43)$$

which in fact proves that with $l \gg 1$ the linear relation $\omega = \Omega_c = eB/m_c$ is valid. Large filling values l are achieved at small values of B , where the absolute limit of B fully depends on the characteristics of the electronic band. If the maximal cross section of the Fermi surface equals A_F , then it follows that:

$$A_F = A_i(B) = A_{i-1}(B'). \quad (3.44)$$

Eqs. (3.42) and (3.44) show that some Landau tube will directly overlap with A_F each time $1/B$ increases by $\Delta(1/B) = 2\pi e/\hbar A_F$. For a 2D system, $n_{2D} = A_F/(2\pi)^2$, therefore we obtain:

$$\Delta(1/B) = \frac{De}{n_{2D}\hbar}, \quad (3.45)$$

where we added the degeneracy D of the electronic band in zero field. See that Eq. (3.45) fully agrees with the result Eq. (3.41), where the dispersion is parabolic.

The DOS $g(\epsilon)$, presenting the number of states which may be occupied in an energy interval, splits into multiple Dirac delta functions when the magnetic field is applied. The positions of the Dirac delta function are defined by the allowed LLs of the system. Let us imagine that we slowly change the magnitude of \mathbf{B} . The sequential crossing of Landau tubes with the Fermi surface results in a modulation of the DOS at the Fermi level. It is important to mention that in realistic conditions LLs are in fact smeared in energy. For example, in Fig. 3.6 a splitting of a constant $g(\epsilon)$ is illustrated. Some of the reasons are the thermal broadening of the Fermi surface, defects in samples, scattering of the particles, etc. We have discussed above that low magnetic fields are required for the valid use of the semiclassical model since it introduces a high number of LL below the Fermi energy. At low magnetic field limit, the distortion of the DOS results in superimposed oscillations on top of the unperturbed DOS that have an amplitude smaller than the DOS at the Fermi level (see Fig. 3.6(b)). This phenomenon is called the Shubnikov–de Haas effect (SdH) [59]. Since most electrical properties depend on the DOS, this can result in detectable oscillations with respect to $1/B$ with a frequency of

$$f = \frac{n_{2D}\hbar}{De}. \quad (3.46)$$

The "classical" electrical properties of the system remain almost the same in low magnetic fields. However, if a measuring technique allows a sufficient signal-to-noise ratio, the density oscillations can also be detected. With the help of lock-in detectors, this can often be the case in resistivity and capacitance studies through the electrical contacts to the system, as will be presented in Sections 7.1 and 7.2. While the quantum part of capacitance has a simple relation to the DOS: $C_Q = e^2 g(\epsilon)$ [60], the derivation of

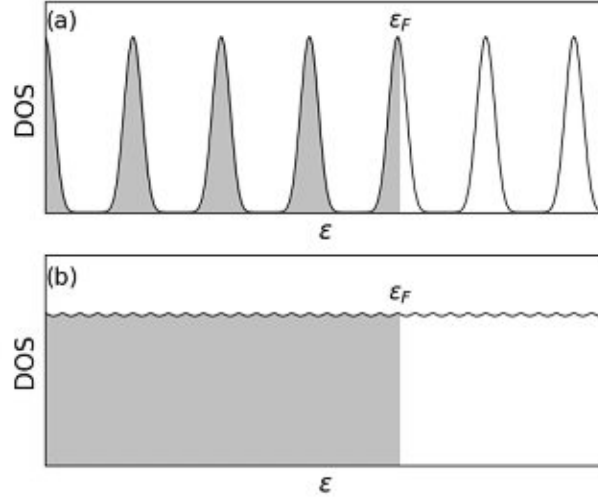


Figure 3.6: Splitting of a constant DOS into smeared Landau levels. If the number of filled LL is low (a), some energy regions have zero allowed electronic states. In the other case, when multiple LL are filled (b), the smeared Landau peaks overlap, which results in a harmonically oscillating DOS.

resistivity from DOS is certainly not as straightforward [61].

Nevertheless, one can analyse the field-dependence of both, capacitance or resistivity measurements of the sample, by applying the Lifshits-Kosevich model of i charge carriers in the system [62] (as done previously in Refs. [63, 64]):

$$\frac{\Delta A}{A_0} = \sum_i A_i D(X) \exp\left(\frac{-\pi}{\mu_{qi} B}\right) \cos\left(\frac{2\pi f_i}{B} + \phi_i\right), \quad (3.47)$$

where A_0 is the monotone part of capacitance or resistivity A . The oscillating part $\Delta A = A - A_0$, $D(X) = X/\sinh(X)$ is the thermal damping factor, where $X = 2\pi^2 k_B T / \hbar \Omega_c$; k_B is the Boltzmann constant, Ω_c is the cyclotron frequency, A_i and ϕ_i are some constants and $\mu_{qi} = e\tau_q/m_c$ is the quantum mobility, where τ_q is the quantum single-particle relaxation time, which determines the LL broadening and has no direct relation to τ (see Refs. [65, 66] for details). Finally, the Lifshits-Kosevich formula can be used to extract the carrier properties from the oscillation period as Eq. (3.46).

4. Mercury Telluride

Mercury telluride (HgTe) has been known for decades for having a zero-gap semi-metallic band structure. Many alloys can be formed from HgTe and other compounds within the same columns of the periodic table. One example is the chemical compound of HgTe and cadmium telluride (CdTe). The alloy $\text{Cd}_x\text{Hg}_{1-x}\text{Te}$ has been for more than sixty years one of the most crucial materials for the industry of infrared detectors [67, 68]. Besides the optimal efficiency of detection, the most essential property of this alloy is the adjustable bandgap. Due to the approximately 1.5 eV bandgap [69] in bulk CdTe, the bandgap in $\text{Cd}_x\text{Hg}_{1-x}\text{Te}$ can be tuned from -0.3 to 1.5 eV by varying the composition ratio x . This allows the production of detectors for the regions between short-wave infrared to very long-wave infrared radiation. We will soon discover that the negative bandgap above is not a typo, but an indication of the inverted band structure, which made HgTe one of the most important compounds for the emerging field of topology in condensed matter.

In 1980, von Klitzing discovered the quantum Hall effect (QHE) [6] in a high-mobility 2D semiconductor at low temperatures. He showed that the Landau quantization (see Section 3.3) results in a vanishing longitudinal conductivity σ_{xx} and quantization of the Hall conductivity σ_{xy} to integer multiples of e^2/h . It was later recognized that this phenomenon of quantization can be characterized by an integer topological invariant [4, 5]. The QHE became the first observed topological state. This marked a very important historical point in the field of topology in condensed matter and drove many researchers into the pursuit of other topological phases. In 2005, a new topological state, a quantum spin Hall system, was proposed [7] and then observed in 2007 in a HgTe quantum well [8]. In contrast to QHE, this state appears only without a magnetic field and consists of two counter-propagating edge states with opposite spins, which makes this very attractive for the field of spintronics. Moreover, if the HgTe quantum well has the correct width (critical thickness), the band structure forms a Dirac cone, i.e., a linear dispersion of the bands [10, 11], which results in unusual electrodynamic properties [57, 70, 71]. HgTe quantum wells above the critical thickness represent unique examples of 2D systems, in which electrons and holes coexist simultaneously, i.e., 2D semimetals [9]. Finally and surely as much important, even wider quantum wells, well above the critical thickness, have shown to be 3D topological insulators (TIs) [12]. A TI is a state of matter in which the bulk of the material is insulating and the surfaces (or edges in 2D) are conducting. The surface states in TIs have a non-degenerate Dirac-like dispersion with electron spin locked to the direction of the momentum. The conducting surfaces appear because there are always zero energy states on the border between two

materials with different characteristic topological invariants. All these exotic properties can be observed in HgTe quantum wells due to the unique inverted band structure of bulk HgTe, which makes the compound topologically non-trivial. The field of topology will not be further discussed in this thesis, an avid reader is invited to find further information in Refs. [72–75].

4.1 The Inverted Band Structure of HgTe

Similar to other II-VI¹ and III-V compounds, mercury (group II) and tellurium (group VI) form HgTe in a zinc-blende (sphalerite) structure [76]. This compound forms due to the bonding between mercury's two valence electrons from the subshell 6s and tellurium's six valence electrons from the subshells 5s and partially filled subshell 5p. Consequently a sp^3 state forms, where one valence electron is in the s state and three of them in the p state. In this family of semiconductors, it is common that in the vicinity of the Fermi energy, the band structure consists of a conduction band Γ_6 and a valence band Γ_8 , separated by a non-zero bandgap. With the increasing atomic number of the constituent atoms, the bandgap between the bands starts to decrease, and in the case of HgTe, it even becomes negative. Let us explain what a negative bandgap actually represents. Due to relatively large nuclear charges of mercury and tellurium atoms, relativistic effects need to be considered in the total Hamiltonian for an accurate calculation of the band structure [76, 77]. The effect of the relativistic corrections, including the Darwin correction (H_D), relativistic mass velocity correction (H_R), and the spin-orbit operator (H_{SO}), can be seen in Fig. 4.1, where the evolution of bands of HgTe and CdTe at the Γ -point is compared. Darwin correction corresponds to the interaction of the s electrons with the nucleus and the relativistic mass velocity term is the correction to the kinetic energy operator due to an increase in the mass of the particle with its velocity. These two terms shift the energy positions of the electronic bands. While the Darwin term has a similar effect on both compounds, it can be seen that due to the different nuclear charges of Hg and Cd, the relativistic mass velocity correction is much stronger for HgTe and results in lowering the Γ_6 band close to the Γ_8 band. Lastly, the spin-orbit interaction splits the degenerate p-states of the Te atoms into two Γ_8 subbands and one Γ_7 band. In the case of CdTe, the total splitting forms a heavy- and a light-hole Γ_8 subband and an electronic Γ_6 band. This represents a conventional semiconductor band structure, i.e., Γ_6 is the first conduction band and the Γ_8 subbands are the valence bands. In the case of HgTe, the Γ_8 band is lifted above the Γ_6 band. Γ_6 becomes a completely filled second valence band, the heavy-hole subband of Γ_8 becomes the first valence band and the light-hole Γ_8 subband now becomes the first conduction band. As a result of the relativistic corrections, HgTe is characterized by an inverted band structure (see Fig. 4.2 left), compared to the normal band ordering in CdTe. Since the light- and heavy-holes subbands are de-

¹Group in the Mendeleev's periodic table of elements.

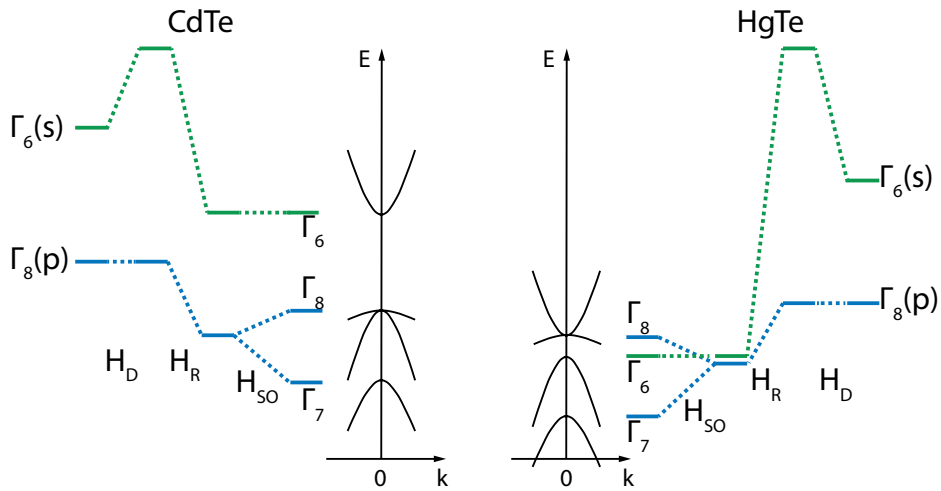


Figure 4.1: An illustration of the impact of the relativistic corrections on the band structures of CdTe (left) and HgTe (right) at the Γ -point. The unperturbed bands are modified by the Darwin correction (H_D), relativistic mass velocity correction (H_R), and lastly the spin-orbit interaction (H_{SO}). Since Hg is much heavier than Cd, the mass velocity correction leads to an inverted band structure in HgTe. Data for the figure was taken from [76].

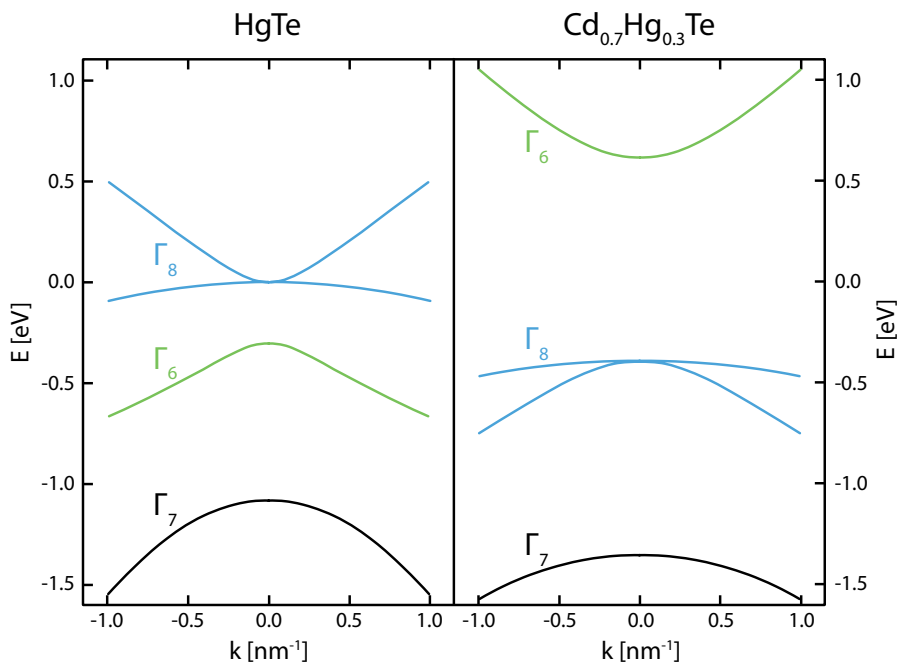


Figure 4.2: Band structures of HgTe and $\text{Cd}_{0.7}\text{Hg}_{0.3}\text{Te}$. Data for figure taken from [78].

generate at the center of the BZ, this represents a zero-gap semiconductor (sometimes also referred to as a semi-metal) [76, 77]. The inverted band structure makes the HgTe topologically non-trivial, making the compound an outstanding playground of various exotic phenomena.

4.2 Strained HgTe Films

The unstrained single-crystalline mercury telluride (HgTe) is a gapless semimetal with the conduction and valence bands formed by Γ_8 bands. If grown in the form of a thin film sandwiched between two thick layers of $\text{Cd}_{0.7}\text{Hg}_{0.3}\text{Te}$, HgTe is subject to a tensile strain due to lattice mismatch between HgTe and CdTe [79]. This strain lifts the degeneracy of Γ_8 at the Γ -point and opens up a bandgap between the light- and heavy-hole Γ_8 subbands [12, 79]. As seen in Fig. 4.2, the band structure of bulk $\text{Cd}_{0.7}\text{Hg}_{0.3}\text{Te}$ shows a conventional band structure with a gap of around 1 eV between the upper Γ_6 and lower light-hole Γ_8 subband. The band profile of the resulting quantum well is strongly dependent on the thickness of the HgTe layer (see Fig. 4.3). The narrower the quantum well, the stronger is the confinement strength. The evolution of the subband order in respect to the varying HgTe layer thickness is presented in Fig. 4.3(a). Subbands E_i and H_i are the result of the confinement quantization and originate from Γ_6 and Γ_8 bands, respectively (see Fig. 4.3(b)). Thicker HgTe layers are characterized by the same band inversion as the bulk HgTe. H_1 , originating from Γ_8 , is above the E_1 , which comes from the Γ_6 band. On the other side, for very thin samples, the quantum well adopts the normal band ordering, where E_1 becomes the first conduction band and H_1 the first valence band. Quantum wells below the critical thickness of 6.3 nm are therefore topologically trivial, while thicker samples have the topologically non-trivial inverted band structure.

When the quantum well has exactly the critical thickness, the bandgap collapses and a zero gap-state is formed, resulting in a 2D electron gas with a Dirac cone dispersion [10, 11, 80]. Compared to graphene [81], which is characterized by a fourfold degenerate Dirac cone, the Dirac cone in HgTe is double degenerate, making HgTe therefore even more attractive.

Let us return to the samples with thickness above the critical value. Due to the inverted band structure inside the quantum well, the topological invariant changes on the borders between HgTe and $\text{Cd}_{0.7}\text{Hg}_{0.3}\text{Te}$, as shown in Fig. 4.3(b). This results in topologically protected zero-energy states on the interface surfaces and the so-called TI phase. If the Fermi level is in between the E_1 and H_1 subband, the bulk HgTe is insulating, however, its surfaces are conducting. It should be noted, that since the surface states arise in about 10-20 nm thick layer close to the boundary, a fully insulating bulk is only expected in quantum wells with thicknesses above ~ 50 nm. While it may sound conflicting, a 2D film of HgTe can actually be a 3D TI. The dimensionality of the HgTe film is characterized by the obvious number quantization of the electronic bands due to

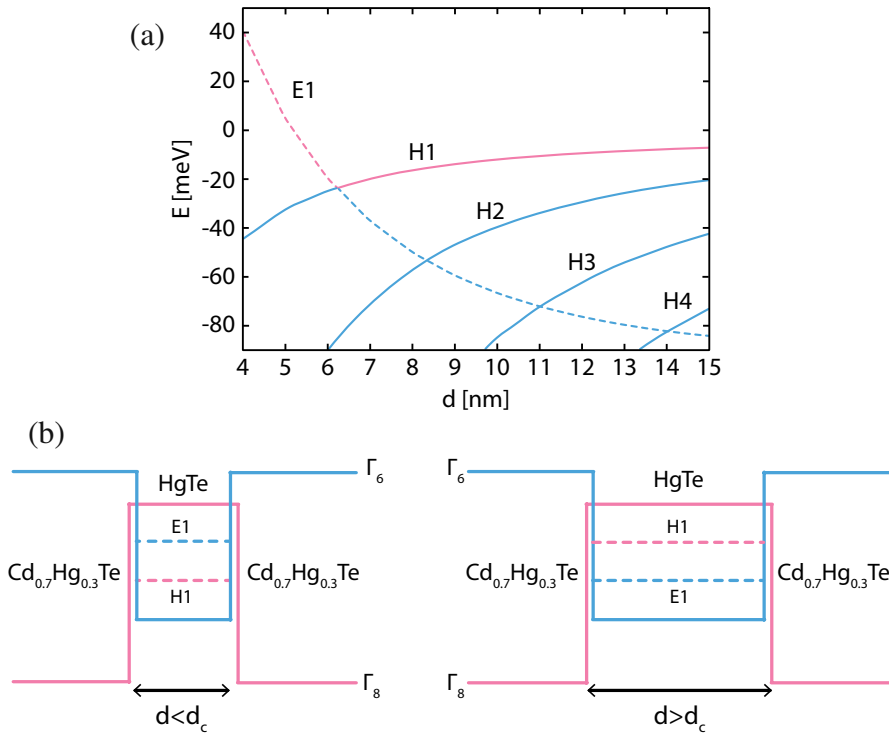


Figure 4.3: Subband ordering in the HgTe/CdHgTe quantum wells in respect to the thickness of the HgTe layer. E subbands originate from the bulk Γ_6 band and H from the bulk Γ_8 band. (a) The energy of the subbands at the γ -point in respect to the quantum well width. Colors indicate conducting (pink) or valence (blue) behavior. (b) The quantum well in the normal regime ($d < d_c$) and the inverted band structure regime ($d > d_c$), where, due to the inversion of the bands, surface states appear at the interface. Data for figures taken from Refs. [10, 11].

the confinement in the z -axis, while the 3D TI is characterized by conducting states on the borders of the confinement.

4.3 Sample Preparation

The HgTe/CdHgTe samples, experimentally studied in the chapter ahead, have been grown by molecular-beam epitaxy (MBE) on a GaAs substrate with a lateral size of 5×5 mm [82–86]. The hetero-structure of the sample is sketched in Fig. 4.4(a). The dielectric constant of the approximately 0.5 mm-thick substrate is $\epsilon_{\text{GaAs}} = 12.75$ in the whole frequency range of the study. Between the layered structure and the GaAs substrate a $5\text{--}6 \mu\text{m}$ thick CdTe buffer layer was placed, whose lattice fully relaxes due to its thickness. The CdHgTe/HgTe/CdHgTe layers above the CdTe buffer layer adopt the underlying CdTe lattice constant, resulting in a tensile strain in the HgTe film due to

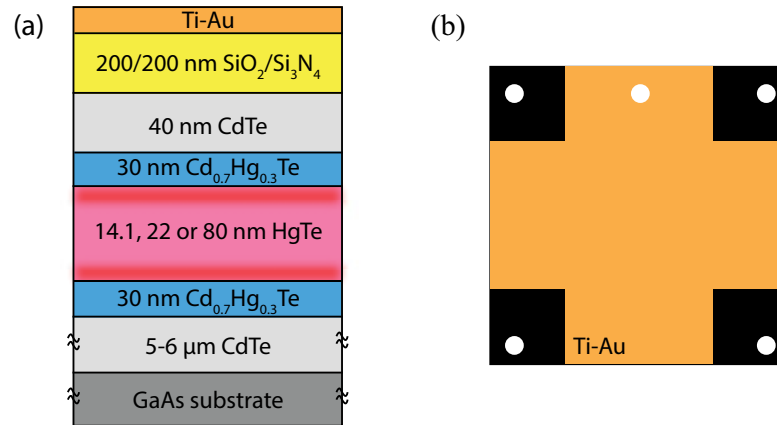


Figure 4.4: (a) Cross-section of the hetero-structured HgTe/CdHgTe samples. The surface states are indicated with bright red. (b) Illustration of the top of the sample with a cross-shaped gate, which allowed simultaneous magneto-optic experiments and transport measurements through the indium contacts (white dots).

the lattice constant mismatch of about 0.3%. The strain results in the opening of the topological bandgap as discussed in the previous chapter. This sandwich structure ensures that the lattice variation is not abrupt, in turn reducing the influence of dislocations and allowing very high electron mobilities. The analysis of the cyclotron resonance corresponding to the upper surface state of the 80-nm sample (Section 7.1) revealed the mobility to be up to $\mu = e\tau/m_e = 5 \cdot 10^5 \text{ cm}^2/\text{Vs}$, which is the current record value for a 3D TI [84]. To produce the semitransparent gate electrode, the film was covered on top by a multi-layer insulator of $\text{SiO}_2/\text{Si}_3\text{N}_4$ and a semitransparent metallic Ti-Au layer. The top-gate electrode allows to control the total charge density and therefore the variation of the Fermi energy in the system [19, 80, 85]. Due to the low mobility of carriers in the Ti-Au layer, the gate showed no measurable magnetic field or radiation frequency dependence [57]. The shape of the gate electrode (see Fig. 4.4(b)) allowed a fully covered center of the sample for THz transmission measurements and four contacts at the corners of the sample to acquire simultaneous information about the electrical conductivity in the system (see Fig. 5.2). The samples in this study had substrates with orientations (013) and (100)². Thermodynamic analysis showed that during the MBE growth of CdHgTe, evaporated Te_2 molecules reach the surface of the sample and can either form CdHgTe or a polycrystalline Te. Formation of the latter form degrades the purity of the CdHgTe layer. However, if the substrate has steps as in the case of the (013) surface, crystallization of tellurium is less probable, resulting in a reduced number of defects and improved quality of the hetero-structure [82, 87]. Samples with a (013) substrate can therefore be of better quality than the ones with (100) surface orientation, on the other hand, (100) substrate does not break the symmetry of the HgTe layer and allows investigation of the purer HgTe form besides an easier theoretical approach for

²This Miller index of the substrate is parallel to the normal of the plane.

calculating its band structure.

In this study, four samples of HgTe/CdHgTe quantum wells were investigated. Two semi-metallic samples with 14.1- and 22-nm thick HgTe layers and a (013) surface orientation and two 3D TIs with 80-nm-thick strained HgTe layers with a (100) substrate. A study of the superradiance effect in a strained 80-nm-HgTe sample will be presented in Chapter 6. In Chapter 7, we will describe a procedure for directly obtaining the band structure of a 2D thin film, specifically, band structures of the 14.1-, 22-, and 80-nm samples.

5. Experimental Investigation of HgTe Samples

Chapter 3 was devoted to the response of a 2D electron gas when it is subject to applied electromagnetic fields. We have discussed the semiclassical behavior of electrons in their characteristic band structure and, as well, the quantization of the system when, at very low temperatures, higher magnetic fields are applied. This should serve as a very good indication that experiments with electromagnetic fields present a very powerful tool for understanding the electronic structure of a studied system. In this thesis, we predominately focus on 2D systems, therefore, we surely only graze the surface of all the possibilities of how various systems respond to applied electromagnetic fields [14, 88–90].

In the present study, we focus on magneto-optics. There is an endless selection of published studies, which have shown the success of magneto-optical experiments when investigating the charge dynamics in metals and semiconductors. It should be stressed that measurements of magneto-transport serve as a very powerful tool, however, optical experiments have the advantage of being contact-free and provide a very accurate assessment of the charge carrier masses via the cyclotron resonance studies. As will be discussed in Chapter 7, measurement of the field-dependent cyclotron frequency gives direct relation to the band structure of the studied material. Recently, several magneto-optical experiments in the THz range were successfully applied to graphene [91, 92], topologically insulating Bi_2Se_3 [93, 94], and, most importantly, HgTe/CdHgTe quantum wells [69, 83, 95–97].

In this section, we will briefly describe the sequential order of performed magneto-optic measurements on HgTe quantum well samples and later go through the process of the analysis of the transmission spectra, which were acquired while the following parameters were varied: gate voltage, external magnetic field, and frequency of radiation. The variation of gate voltage allowed changing the total charge density in the sample, therefore moving the Fermi energy from the valence to the conduction states.

5.1 Cyclotron Resonance Experiments

Magneto-optical transmission experiments were carried out in the Mach-Zehnder interferometer (Section 2.2.1) using several BWO sources, which cover various frequency regions between 40 – 1000 GHz (see Fig. 2.4). The sample was mounted on a sample

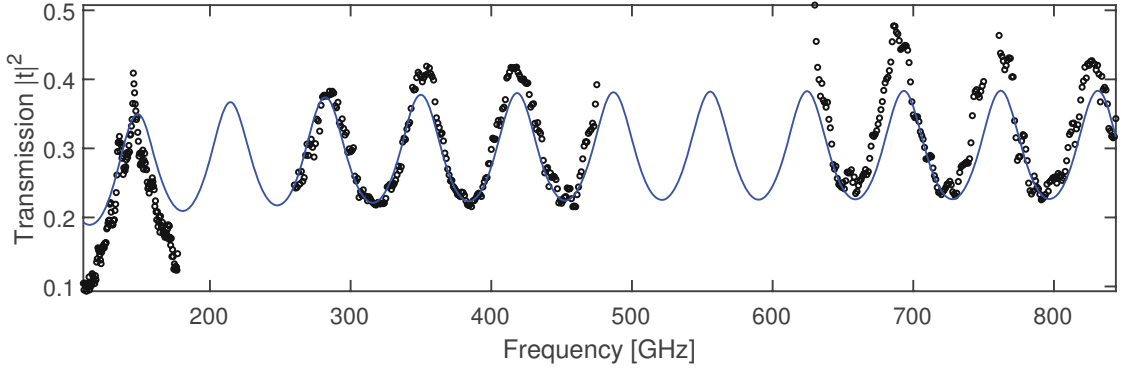


Figure 5.1: Frequency dependent intensity of transmission of the 80-nm HgTe film in zero magnetic field and at $T = 1.8$ K. Open black circles - experiment, blue curve - fit using transmission formulas and the Drude model. Substrate parameters are: thickness $d = 0.608$ mm, refractive index $n = 3.57$.

holder (Fig. 5.2(a)) and inserted into the cryostat, where it was cooled to 1.8 K. Transmission experiments were carried with a split-coil superconducting magnet that provided an external magnetic field up to 7 T in the Faraday geometry; i.e., a magnetic field was applied along the propagation direction of the radiation (see Fig. 5.5). The experimental procedure was as follows. A BWO source was selected and adjusted in the optical setup shown in Fig. 2.3. This was followed by a frequency-dependent transmission measurement of the sample (at zero gate voltage and zero magnetic field) which showed pronounced Fabry-Perot interference [98] due to the reflections within the substrate. These measurements were performed in the transmission measuring mode and with linearly-polarized light in the parallel geometry of the interferometer. For each BWO, the measurement was repeated with the empty channel (without the sample) in order to obtain the absolute unit of the amplitude: $|t_p(\nu)| = t_{\text{sample}}/t_{\text{ref}}$. These measurements will be labeled as "frequency scans". In Fig. 5.1 the spectrum of the 80-nm sample (Section 7.1) measured by three different BWO sources is plotted. It clearly demonstrates the multiple reflections within the GaAs substrate with a thickness of $d = 0.608$ mm. We can also notice a slight decrease of amplitude at lower frequencies, which is related to the relaxation rate τ of the charge carriers in the system. From the acquired frequency spectrum, a set of frequencies ν_j is selected for detailed magneto-optic measurements. The process of selection is strongly affected by the transmission amplitude. If the transmission is high, the detected signal is stronger and, therefore, a higher signal-to-noise ratio is assured. Moreover, the additional aim was to find frequencies that most uniformly cover the whole range of our spectrometer.

The setup presented in Fig. 5.2(b) allowed us to measure 4-point resistivity in the xx -configuration. Right before or right after running the field-dependent transmission scan at zero gate voltage, a gate-dependent measurement of 4-point resistivity was performed in order to evaluate the electronic state of the sample with respect to the position of the charge neutrality point - resistivity reaches its maximum due to the equal den-

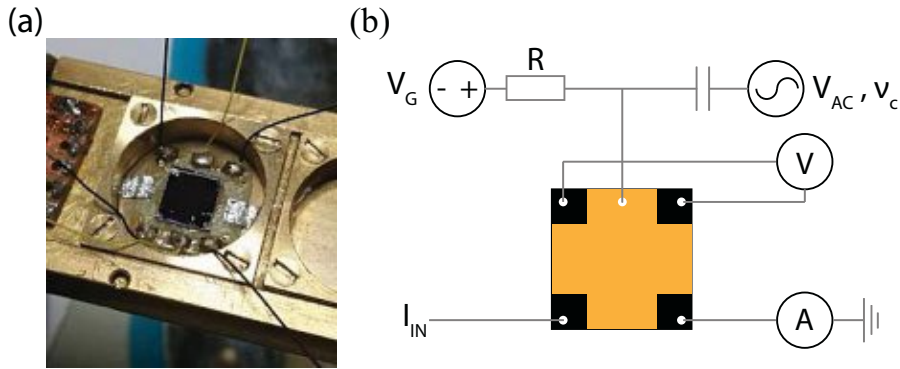


Figure 5.2: (a) The sample mounted on the sample holder. (b) A schematic of the electrical circuits connected to the sample with silver paste. With the use of two isolated frequency lock-in detection systems this setup allowed simultaneous measurements of the 4-point resistance (V) and capacitance (A).

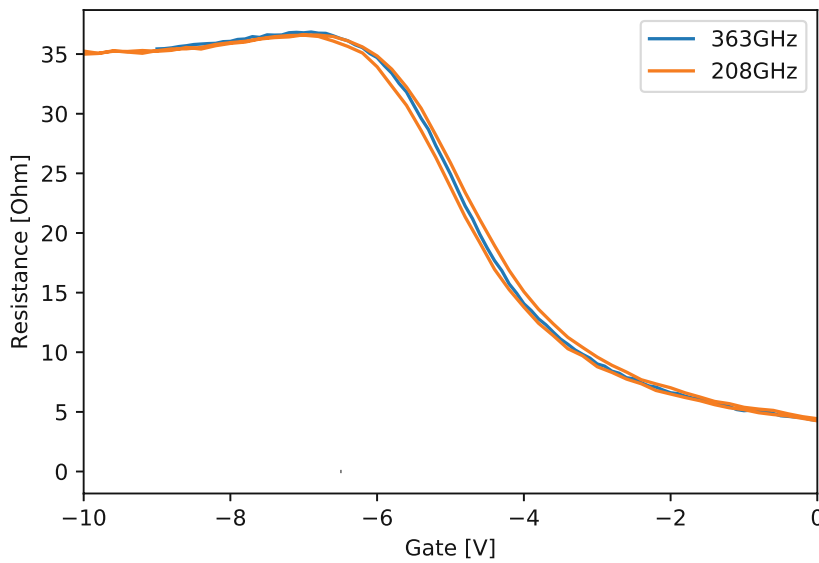


Figure 5.3: Gate-dependence of the 4-point resistance in the xx -configuration in case of the 22-nm sample from Section 7.2. The position of the maximum resistance at around -7 V marks the charge neutrality point (CNP).

sities of electrons and holes. The aim was to ensure that the sample was in the same electronic state when zero gate voltage measurements were performed with different BWO sources. Fig. 5.3 shows how the gate successfully altered the charge density in the 22-nm sample from Section 7.2. Generally, the position of the neutrality point was observed to be dependent on the history of the applied gate voltage in a specific cooling cycle. Warming the sample to ~ 150 K and back to 1.8 K returned the position of the

charge neutrality point to the initial value.

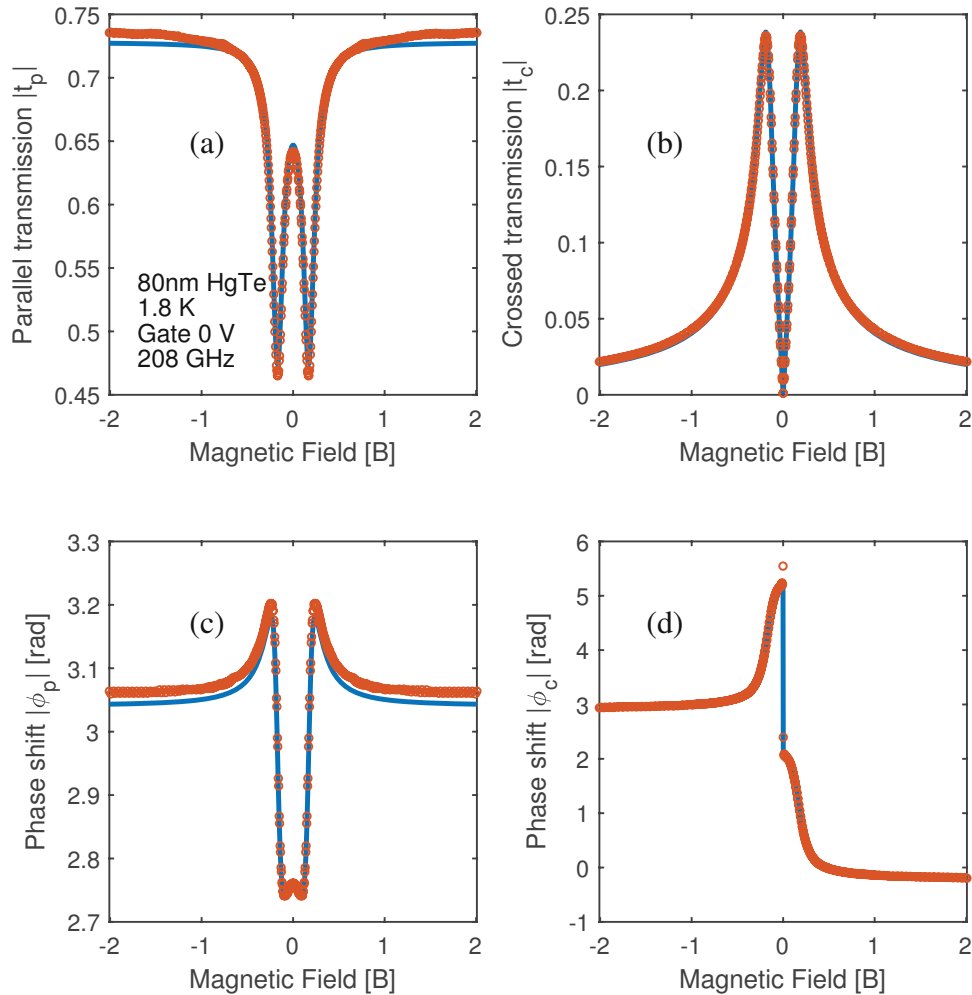


Figure 5.4: Field dependency of the parallel and crossed transmission through the 80-nm-HgTe sample, which is in detailed discussed in Chapter 6. The frequency of incident radiation was 208 GHz and the gate of the sample was set to 0 V. (a,c) Absolute value and phase of the transmission in the parallel geometry. (b,d) Absolute value and phase of the transmission in the crossed geometry. Orange circles - experimental data, solid blue lines - fits using the transmission formulas and the Drude model as described in text.

After the frequency scans, the frequency was fixed at each of the selected values ν_j . For each ν_j , the field-dependent transmission through the sample was measured at different gate voltages. The polarization of the radiation incident on the sample was either linear or circular. We will label these measurements as the "field scans".

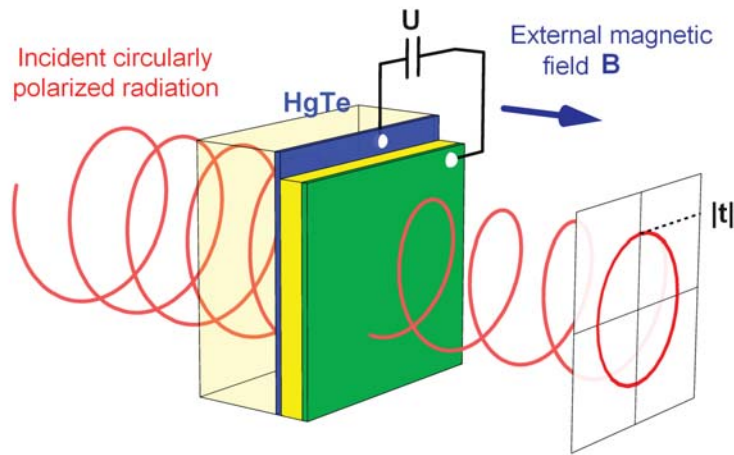


Figure 5.5: Illustration of the magneto-optical experiment with circularly-polarized radiation.

In case that the linear polarization of radiation was picked for fixed-frequency field scans, the complex transmission was measured in both, parallel and crossed geometry. In order to obtain the fully complex transmission, the measurements were performed in the phase measurement mode of the interferometer. A typical example of the measured data of an HgTe film is shown in Fig. 5.4. The two symmetrical minima in the absolute parallel transmission (Fig. 5.4(a)) and maxima in absolute crossed transmission (Fig. 5.4(b)) correspond to the cyclotron resonances of the charge carriers in the HgTe film. The resonances reach their extreme values when the cyclotron resonance (Eq. (3.5)) condition is satisfied and $\omega = eB/m_c$, where $\omega = 2\pi\nu$ and the frequency of the radiation is $\nu = 208$ GHz. The resonances reach their extreme at around ± 0.16 T, which gives $m_c = 0.022 m_e$. Here, $m_e = 9.109 \cdot 10^{-31}$ kg is the electron rest mass. The absolute crossed transmission reaches zero at zero magnetic field, increases until the cyclotron resonance condition is satisfied, and then decreases to zero again. This suggests that at the resonance frequency the polarization of the radiation is rotated. The phase (Fig. 5.4(c,d)) of the measured complex transmission in both geometries shows that the optical thickness of the sample changes. While the change of parallel transmission phase is relatively small, the "crossed" phase changes drastically. An abrupt change of the "crossed" phase at zero magnetic field indicated that the crossed signal changes its sign. In fact, we can conclude that not only the polarization of the incident beam rotates, the beam also obtains an elliptical character.

The main drawback of measurements with linear polarization is the following. With the fixed frequency, the elements of the quasi-optical setup need to be optimized in either linear or crossed geometry. After, the field scan is measured for each value of the selected gate voltage range. The setup is then rearranged into the other geometry (linear

or crossed) and the measurements are repeated. The parallel and crossed field scans at a specific gate voltage are usually measured with large time delays (hours or sometimes even days) and even in different cooling cycles. This does not necessarily ensure the exact same state of the sample.

This problem is averted with the use of the much simpler experimental procedure with the circularly-polarized beam (see Fig. 5.5), which is carried out with the Mach-Zehnder interferometer in the transmission measuring mode and set in the configuration shown in Fig. 2.6. Here, only one field scan at each state of the sample is necessary. The additional advantage of geometry with circularly-polarized radiation is the clear separation of the electron and hole resonances as they are observed for positive and negative external magnetic fields, as will be shown in the section ahead. It should be noted that the circular polarization gives only limited information about the complex transmission of the system. As we will see below, it provides enough data to obtain properties of the charge carriers in the system. However, if the study requires a detailed analysis of the Hall conductivity, data obtained from circularly-polarized transmission does not suffice. In this case, parallel and crossed geometry are crucial, since they provide the full complex transmission of the system.

5.2 The Drude Analysis

The analysis of the magneto-optical data obtained from the interferometer was done with the help of the Drude model (Section 3.1), which previously provided a great tool to obtain the required information about the investigated system [18,57,69,97,99,100]. The HgTe samples were composed of a layered structure on a dielectric GaAs substrate (see Fig. 4.4(a)). In the layered structure, only the HgTe layer and the gate have a metallic character. The section containing conducting layers is less than $0.5 \cdot 10^{-3}$ mm thick, while the thickness of the substrate is around 0.5 mm. Since the shortest achievable wavelength in our spectrometer is around 0.3 mm, in terms of the available resolution and maximal energy of the radiation, the sample can be efficiently represented as an isotropic dielectric slab with a metallic infinitely-thin film on top. An analytic solution for the complex transmission in terms of t_p and t_c through such system was presented with Eq. (2.30). Let us rewrite the result and remember the definitions of the parameters:

$$t_p = \frac{2a_{xx}}{a_{xx}^2 + a_{xy}^2}, \quad t_c = \frac{2a_{xy}}{a_{xx}^2 + a_{xy}^2}, \quad (5.1)$$

with:

$$a_{xx} = (1 + \sigma_{xx}\eta_0) \left(\cos \beta - \frac{1}{\sqrt{\epsilon_{\text{GaAs}}}} \sin \beta \right) + \cos \beta - i\sqrt{\epsilon_{\text{GaAs}}} \sin \beta,$$

$$a_{xy} = \sigma_{xy}\eta_0 \left(\cos \beta - \frac{1}{\sqrt{\epsilon_{\text{GaAs}}}} \sin \beta \right),$$

$$\beta = \sqrt{\epsilon_{\text{GaAs}}} \frac{\omega}{c_0} L,$$

where L is the substrate thickness, $\epsilon_{\text{GaAs}} = 12.75$ (Section 4.3), η_0 is the impedance of free space and $\omega = 2\pi\nu$ is the angular frequency, with ν being the frequency of the incident radiation. The components of the 2D conductivity tensor σ are calculated in terms of the Drude model, as defined in Eq. (3.6) (see also Eq. (3.7)). The conductivity of the system involving multiple charge carriers i can be written as:

$$\begin{aligned} \sigma_{xx} &= \sum_i \sigma_{xx,i} + \sigma_{\text{Gate}} \\ \sigma_{xy} &= \sum_i \sigma_{xy,i}, \end{aligned} \quad (5.2)$$

where σ_{Gate} corresponds to the gate conductivity, which is field- and frequency-independent and $\sigma_{xx,i}$, $\sigma_{xy,i}$ correspond to each individual charge carrier i , where

$$\begin{aligned} \sigma_{xx,i} &= \sigma_{0,i} \frac{1 - i\omega\tau_i}{(1 - i\omega\tau_i)^2 + (\Omega_{c,i}\tau_i)^2}; \\ \sigma_{xy,i} &= \sigma_{0,i} \frac{\Omega_{c,i}\tau_i}{(1 - i\omega\tau_i)^2 + (\Omega_{c,i}\tau_i)^2}; \\ \Omega_{c,i} &= \frac{eB}{m_i}; \quad \sigma_{0,i} = \frac{n_i e^2 \tau_i}{m_i}. \end{aligned} \quad (5.3)$$

Each carrier i is characterized by its effective cyclotron mass m_i , scattering time τ_i and 2D charge density n_i ¹. For a circularly-polarized wave, we can write $t_{\pm} = t_p \pm it_c$, where \pm denotes the clockwise or anticlockwise circularly-polarized wave. Similarly, circular conductivity can be defined as: $\sigma_{\pm} = \sigma_{xx} \pm i\sigma_{xy}$. The circular transmission coefficient can be finally written as:

$$t_{\pm} = \frac{2}{a_{\pm}}, \quad (5.4)$$

where $a_{\pm} = a_{xx} \pm ia_{xy}$. In fact, it can be easily seen that t_+ depends purely on σ_+ and t_- depends purely on σ_- , thus the cyclotron resonance can only be seen with either positive or negative magnetic fields, depending on the "charge" of the carrier.

In case the circularly-polarized radiation is set for magneto-optic measurements, we experimentally obtain: (a) the frequency scan $|t_p^{\text{exp}}(\nu)|$ at zero magnetic field, zero gate voltage and measured by all selected BWOs, and (b) a set of field scans $A_j |t_{+,-}^{\text{exp}}(\nu_j, B, U_g)|$, where U_g is the applied gate voltage, ν_j are the selected frequencies for field scans, and A_j is an unknown real constant. We begin the analysis by gathering all the data at zero gate voltage. A Hooke-Jeeves algorithm [101] was used to minimize

¹In terms of simplicity, we will, from here on, omit the c in m_c and the $2D$ in n_{2D} . However, the same definitions still apply.

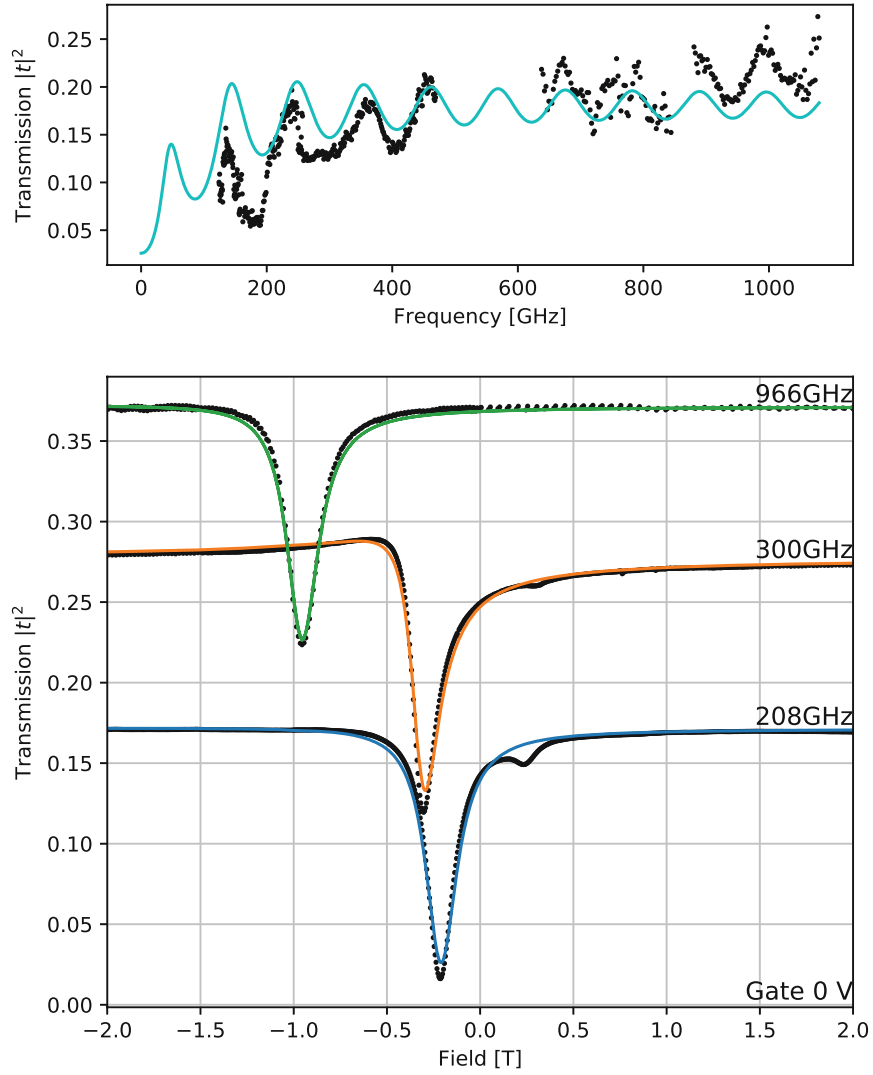


Figure 5.6: Data analysis in order to obtain initial parameters of the 22-nm sample. (Above) Frequency-dependent absolute transmission through the sample at zero magnetic field and zero gate voltage. Black points - experimental data, colored curve - fit using the transmission formulas and the Drude model described in text. (Bottom) Field-dependent absolute transmission at zero gate voltage for three frequencies of incident radiation. Black points - experimental data, colored curves - fit using the Drude model described in text. The absolute scales refer to the lowest curves, others are shifted for clarity.

the following function:

$$\begin{aligned}
 f(A_j, \sigma_{\text{Gate}}, C_{\text{Par}}) = & \alpha_\nu \sum_v (|t_p^{\text{exp}}(\nu)| - |t_p(\nu, B = 0, \epsilon_{\text{GaAs}}, \sigma_{\text{Gate}}, C_{\text{Par}}, L)|)^2 \\
 & + \sum_j \sum_B (A_j |t_{+,-}^{\text{exp}}(\nu_j, B, U_g = 0)| - |t_{+,-}(\nu_j, B, \epsilon_{\text{GaAs}}, \sigma_{\text{Gate}}, C_{\text{Par}}, L)|)^2
 \end{aligned} \tag{5.5}$$

where $C_{\text{Par}} = ([m_1, n_1, \tau_1], [m_2, n_2, \tau_2], \dots)$ is a list of carrier parameters; and L and ϵ_{GaAs} are known. Here, α_ν adjusts the weight of the spectrum for the optimization process and was usually set to 0.1. The optimization process finds the fitting parameters A_j , $\sigma_g(U_g = 0)$ and $C_{\text{Par}}(U_g = 0)$ for the sample at zero gate ($U_g = 0$). The result, corresponding to the 22-nm-HgTe sample from Section 7.2, can be seen in Fig. 5.6. Only a single resonance was observed, indicating a single active charge carrier. The Drude formula confirms that the minimum of transmission is achieved when the cyclotron frequency matches the frequency of the incident radiation. The position of the resonances therefore correspond to the m of the charge carrier, while the width and the amplitude are related to the τ and n , respectively. However, due to the complexity of the fitting function, an analytic relations are not available. When the frequency of radiation matches the cyclotron frequency, one can imagine that in a coordinate system, which is rotating around the same axis, this situation effectively resembles a metal and, thus, most of the radiation is blocked. The drop of signal at lower frequencies is due to the Drude resonance with the center at zero (due to zero magnetic field). The decrease of signal is therefore related to the scattering rate τ . To obtain the fitting parameters from experimental data acquired at non-zero value of gate, an additional analysis is performed. For each frequency ν_j and each value U_g from the set of applied gate voltages, the following function is minimized:

$$f(\sigma_{\text{Gate}}(U_g), C_{\text{Par}}(U_g, \nu_j)) = \sum_B (A_j |t_{+,-}^{\text{exp}}(\nu_j, B, U_g) - |t_{+,-}(\nu_j, B, \epsilon_{\text{GaAs}}, \sigma_{\text{Gate}}(U_g), C_{\text{Par}}(U_g), L)|)^2, \quad (5.6)$$

where the scaling coefficient A_j is now a fixed parameter, since it was obtained before. Carrier parameters were set as free parameters, including the gate conductivity σ_g , which is expected to change only slightly with the applied voltage. This process of analysis is similar for experiments with linear polarization. The second sum in Eq. (5.5) is replaced with two summations corresponding to parallel and crossed data, where the crossed summation is weighted with α_C . Since the measurements include phase, we require two complex scaling coefficients $A_{j,p}$ and $A_{j,c}$. Similar follows for Eq. (5.6). This process allows us to obtain the Drude parameters of the active charge carriers in the system $C_{\text{Par}}(\nu_j, U_g)$, which are obtained at various values of the applied gate voltage U_g and the frequencies of radiation ν_j .

6. Superradiance in HgTe

The phenomenon of superradiance occurs when several emitters become coupled and, as a consequence, they start to radiate coherently [102, 103]. In such a case, the intensity of the emitted radiation is strongly enhanced as it is scaled as a square of the number of sources in contrast to simple proportionality without coherence. Superradiance was first predicted theoretically by Dicke [102] for an ensemble of two-level atoms and has been later on observed experimentally in various materials [104–106] and metamaterials [107, 108], see Ref. [109] for a review.

Recently, superradiant effects in two-dimensional electron gases (2DEGs) have been brought into attention [110–116]. In the original Dicke model, the coherence is obtained because single sources are within a distance smaller than the wavelength of the radiation. An important difference especially compared to the case of the cyclotron resonance in 2DEGs is that the size limitation is lifted in the latter case. The resonance of a single electron is excited coherently by an incident electromagnetic wave. Therefore, independently of the sample size, they re-emit a coherent secondary wave. We recall that the consideration of the secondary waves is a standard procedure to calculate the interaction between electromagnetic waves and matter [117]. In addition to the radiative losses, usual scattering processes, like impurity scattering, contribute to the lifetime of the cyclotron resonance as already discussed in Section 3.1. In 2DEGs the effects of the superradiance may be easily monitored experimentally, e.g. by varying the temperature or gate voltage.

The results of this chapter have been published in Ref. [118].

6.1 Superradiant Decay and the Drude Model

As extensively discussed previously, the superradiance effects in 2DEGs may be well explained via the classical picture [119–121]. Indeed, although the cyclotron resonance is the transition between quantized Landau levels, for not too high fields a quasi-classical approach is sufficient because several levels take part in the transition process (see Chapter 3). In this case, the cyclotron resonance is scaled linearly with the magnetic field regardless of the details of the band structure. In the following, we reproduce briefly the main expressions describing the cyclotron resonance in 2DEGs including the effects of the radiation losses (superradiance).

We consider a geometry with the external magnetic field and the propagation direction of the incident wave being perpendicular to the film surface. The film is assumed

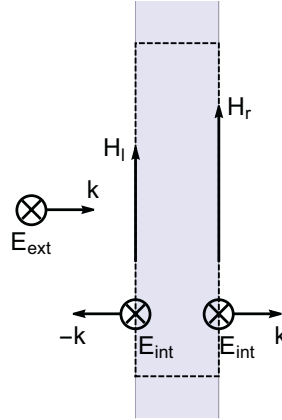


Figure 6.1: Radiation of a 2D electron gas. The electrons are driven by \mathbf{E}_{ext} . Two plane electromagnetic waves (E_{int}) are therefore radiated in both directions parallel to the normal of the film.

to be thin compared to the radiation wavelength inside the sample and, finally, in this section we neglect the effect of the substrate for simplicity. We note that explicitly including the dielectric substrate into account [18, 55, 97] (as in Section 2) produces only marginal changes in the spectra.

In order to explicitly include the radiation losses, the electric field inside the film \mathbf{E} must be connected to the fields of the electromagnetic waves outside the film. Very similar to the procedure in Section 2.1.3, the thin film approximation considers the electric field as homogeneous across the sample. Inside the film the total electric field equals $\mathbf{E} = \mathbf{E}_{ext} + \mathbf{E}_{int}$, where \mathbf{E}_{int} is the field induced by the electrons, and \mathbf{E}_{ext} is the electric field due to the (plane) linearly-polarized external electromagnetic wave. The electrons are driven by \mathbf{E}_{ext} , thus radiating two plane electromagnetic waves in both directions parallel to the normal of the film $\hat{\mathbf{n}}$ as shown in Fig. 6.1. From Eq. (2.2), we obtain the following relations: $H_l = \eta_0^{-1}(E_{ext} - E_{int})$ and $H_r = \eta_0^{-1}(E_{ext} + E_{int})$. The boundary condition for the magnetic fields in the case of thin conducting film is obtained via Eq. (2.7), which leads to the following relation between the tangential magnetic fields on the left and right sides of the film, respectively: $\hat{\mathbf{n}} \times (\mathbf{H}_r - \mathbf{H}_l) = \mathbf{j}_{2D} = -nev$. The reader should note that the conductivity tensor σ , current density \mathbf{j}_{2D} and carrier density n are here two-dimensional. Combining both boundary conditions gives $-\eta_0^{-1}2\mathbf{E}_{int} = nev$, thus allowing to modify Eqs. (3.1) and (3.2) as a function of the incident wave in the following way:

$$d\mathbf{v}/dt + \left(\frac{1}{\tau} + \frac{1}{\tau_{SR}}\right)\mathbf{v} - \frac{e}{m}\mathbf{v} \times \mathbf{B} = \frac{e}{m}\mathbf{E}_{ext}e^{-i\omega t}, \quad (6.1)$$

where $1/\tau_{SR} = ne^2\eta_0/2m$ now takes into account the radiation losses explicitly. Here, we already know η_0 as the impedance of the free space. Equation (6.1) demonstrates that

the losses in a thin film can be represented as a sum of two contributions, given by the transport and radiative lifetimes.

Similar to Section 5.2, where we have inserted the Drude model from Eq. (3.6) into the transmission coefficients from Eq. (2.30), we can assume a single charge carrier and set $L = 0$. After a usual algebra, we can write the following expressions for transmission through the film in terms of the superradiant scattering time τ_{SR} :

$$t_p = 1 - \frac{i}{\tau_{\text{SR}}} \frac{\omega + i\Gamma}{(\omega + i\Gamma)^2 - \Omega_c^2}, \quad (6.2)$$

$$t_c = \frac{1}{\tau_{\text{SR}}} \frac{\Omega_c}{\Omega_c^2 - (\omega + i\Gamma)^2}, \quad (6.3)$$

where $\Gamma = 1/\tau + 1/\tau_{\text{SR}}$ is the "total" scattering rate.

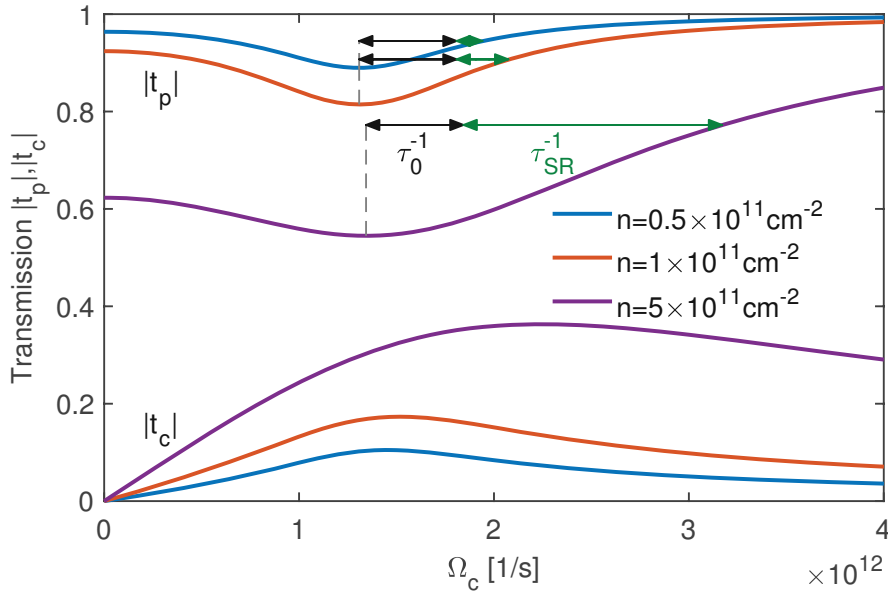


Figure 6.2: Calculated amplitudes of parallel $|t_p|$ and crossed $|t_c|$ magneto-optical transmission at $\nu = 208$ GHz using Eqs. (6.2,6.3). The spectra corresponds to a thin film with electronic carriers with the cyclotron mass $m = 0.02 m_e$, scattering time $\tau = 2 \cdot 10^{-12}$ s, and with varied density as indicated. The apparent width of the cyclotron resonance is determined by $\Gamma = 1/\tau + 1/\tau_{\text{SR}}$ (see text). At low 2D densities n , the intrinsic scattering $1/\tau$ determines the resonance width. By increasing the density the superradiant decay becomes the dominating mechanism for the energy loss in the film.

Figure 6.2 shows the calculated parallel and crossed transmission spectra of a conductive film with typical parameters ($\tau = 2 \cdot 10^{-12}$ s, $m = 0.02 m_e$) at the frequency $\nu = 208$ GHz and for varied electron densities. This frequency was taken to match that of the experiments. It is clear that the denominators in Eq. (6.2) and Eq. (6.3) lead to a resonance-like form of the transmission spectra at $\omega = \Omega_c$ and with the width de-

terminated by τ and τ_{SR} . Here, the electron density n was the only varied parameter, while others, including the scattering time τ , were fixed. With the help of green and black arrows in Fig. 6.2, indicating the amplitude of inverse τ_{SR} and τ , we can see a direct correlation between the width of the resonance with the "total" scattering rate Γ . At low electron densities n the total scattering rate and, consequently, the resonance width is characterized by intrinsic losses only. With increasing n , the energy loss of the system becomes more and more dominated by radiative losses (see data corresponding to $n = 5 \cdot 10^{11} \text{ cm}^{-2}$ in Fig. 6.2). It is important to note that the radiative losses $1/\tau_{\text{SR}} = ne^2\eta_0/2m$ do not add further free parameters to the experiment, because the electron density and the cyclotron mass are independently determined via fitting the transmission spectra as described in the next section.

6.2 Superradiance in a HgTe-Based TI

3D TIs represent a class of materials that are insulating in the bulk but reveal conducting 2D surface states [70, 73]. The surface states in TI have a non-degenerate Dirac-like dispersion with electron spin locked to the direction of the momentum. In the 3D TIs based on HgTe quantum wells, the inversion of the Γ_6 and Γ_8 bands in the dispersion of the bulk HgTe leads to Dirac-like surface states at the interface. Applying strain with the HgTe/CdHgTe structure forms an insulating gap [79, 122] (above 10 meV) between the light-hole and heavy-hole Γ_8 bands, making the strained HgTe a 3D TI. Since the Fermi level of the ungated sample lies in the bulk bandgap between the light-hole conduction and heavy-hole valence band, the electrodynamics of the system is governed only by a 2D surface states, with negligible effects from the bulk carriers at low-temperatures [79, 123]. The Dirac-point of the surface states is presumed to be located deep below the heavy-hole band [97].

As described in Chapter 5, the experiments were carried out on a strained 80-nm-thick HgTe sample, presented in Chapter 4, which was grown by molecular-beam epitaxy on a (100)-oriented GaAs substrate. The sample was investigated in a Mach-Zehnder interferometer shown in Section 2.2.1, which allowed us to acquire the amplitude and the phase shift of the transmitted electromagnetic radiation in parallel and crossed polarizer geometries. The experimental results in this work were obtained at a fixed frequency of 208 GHz in sweeping magnetic fields. Additional information about the charge carriers was also obtained from the frequency-dependent spectra in zero magnetic field. Transmission experiments were carried out at 1.8 K in a split-coil superconducting magnet that provided an external magnetic field up to 7 T in the Faraday geometry; i.e., a magnetic field was applied along the propagation direction of the radiation. The experiments and the analysis were performed as discussed in Chapter 5.

The implementation of the transparent metallic gate on top of the HgTe film enabled us to systematically vary the 2D charge density in this system. The voltage applied to the gate ranged between -2 V and $+12 \text{ V}$ and resulted in magneto-optical transmission

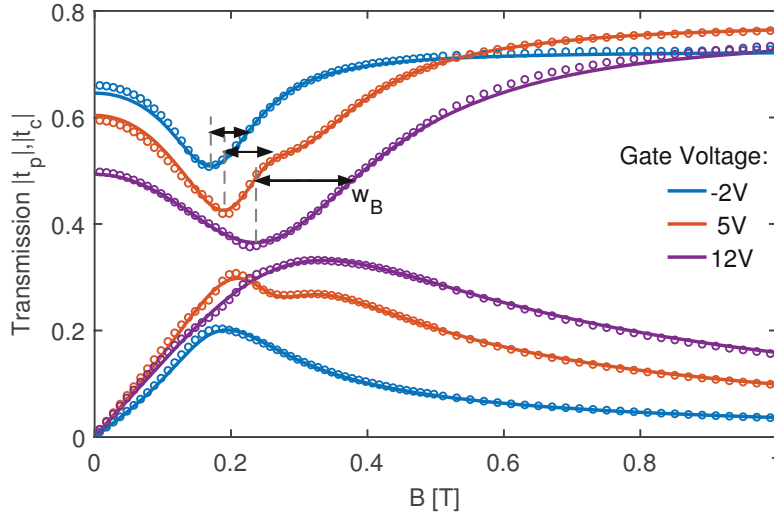


Figure 6.3: Experimental amplitudes of parallel $|t_p|$ and crossed $|t_c|$ magneto-optical transmission at $\nu = 208$ GHz through HgTe film on a GaAs substrate and for different gate voltages. Symbols: experimental data, lines: model fit using the Drude conductivity. Black arrows and w_B represent the apparent width of the resonance curves.

spectra shown in Fig. 6.3.

The magnetic field-dependence in the whole gate voltage range is dominated by a strong cyclotron resonance of the Dirac-like surface electrons located in the bandgap [18]. With increasing the gate voltage the response of such states becomes stronger, and the resonance is getting broader. These spectra qualitatively resemble that in Fig. 6.2, where the broadening is due to increased density only. In addition, for the gate voltage range between 1.5 V and 9.0 V we observed the appearance of a second weaker signal (see double resonance response at 5 V in Fig. 6.3) that corresponds to effective masses of about $0.033 m_e$. According to the band structure calculation for the 3D HgTe films [97] (see also Section 7.1), we attribute this effect to the bulk conduction band. Indeed, this effective mass agrees well with the cyclotron mass of thick unstrained HgTe films [18, 76] ($m \approx 0.03 m_e$). As the additional signal is weak, its properties do not affect the present discussion.

The measured transmission spectra can be fitted well within a Drude model, as described in Section 5.2. From the conductivity tensor, one can obtain an explicit analytical formula for the transmission matrix for the case of a thin film on a substrate that accounts for the Fabry-Pérot interferences in the substrate (see Section 5.2). For each applied gate voltage we simultaneously fit the field dependencies of the amplitude and the phase shift of both, parallel and crossed transmissions, where n , τ and m , characterized by the surface states, were set as free fitting parameters.

The electrodynamic parameters of the surface charge carriers obtained from the fitting of the magneto-optical data are shown in Fig. 6.4. As may be expected, the electron

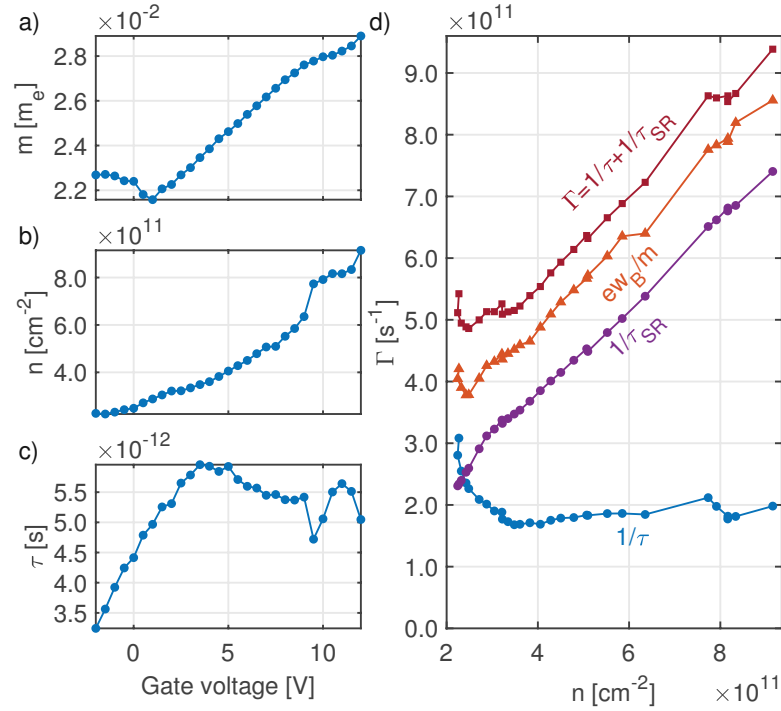


Figure 6.4: Parameters of the surface states obtained from fitting the experimental data in Fig. 6.3. The effective mass m^* (a), 2D density n (b), and the transport scattering time constant τ (c) are plotted with respect to the applied gate voltage. (d) Solid circles: transport scattering rate $1/\tau$ and radiative scattering rate obtained via $1/\tau_{SR} = ne^2\eta_0/(1 + n_{GaAs})m$. Solid squares: "total" scattering rate Γ as compared to the scattering rate calculated directly from the estimated widths w_B of the resonances in Fig. 6.3 (solid triangles).

density of the surface states in Fig. 6.4(b) roughly linearly increases with the gate voltage. On the contrary, the cyclotron mass and the intrinsic scattering time τ show much weaker changes. The surface cyclotron mass of about $0.027 m_e$ is smaller but similar to the bulk mass in HgTe [18]. This similarity is due to strong hybridization of the bulk and surface states [79].

The intrinsic scattering time τ experiences a maximum as a function of the applied gate voltage, which we attribute to the competition of two scattering mechanisms [124, 125]. At first, increasing applied gate voltage causes scattering to decrease (an increase of τ) due to the screening of impurities by higher electron density. The decrease of τ at higher densities (gate voltage above 5 V), where the impurity scattering weakens, is associated with the increasing scattering on the fluctuations of the quantum well width. The resulting fluctuations of the bandgap create mass disorder for Dirac-like states in the system. The material parameters in Fig. 6.4 (a-c) are sufficient to calculate the radiative losses via $1/\tau_{SR} = ne^2\eta_0/(1 + n_{GaAs})m$, a modified version of the formula presented in Section 6.1, which also considers the HgTe film being enclosed by vacuum on one

side and the GaAs substrate with the refractive index of $n_{\text{GaAs}} = 3.57$ on the other side. The values thus obtained are plotted in Fig. 6.4(d) as a function of the electron density. We see that in the present experiment two regimes can be obtained using the gate voltage, one being below $n \approx 3 \cdot 10^{11} \text{ cm}^{-2}$ with a comparable contribution from both mechanisms to the system losses ($\tau^{-1} \sim \tau_{\text{SR}}^{-1}$) and the other at higher electron densities, where the radiative losses are dominant $\tau^{-1} < \tau_{\text{SR}}^{-1}$.

We recall that the width of the resonance curves (Figs. 6.2, 6.3) depends upon the total scattering rate Γ . This fact is confirmed in Fig. 6.4(d) directly comparing the total scattering rate Γ (squares) with the width of the resonance ew_{B}/m (triangles). We note a good agreement between both data sets. These data demonstrate that internal and radiative losses can be seen in the continuous-wave spectra directly. Finally, in the present experiments, the obvious broadening of the observed cyclotron resonance curves is purely due to the increase of the radiative losses.

6.3 Summary

Using THz magneto-spectroscopy we investigated the cyclotron resonance in a 3D TI HgTe with conducting surface states. From the analysis of the complex transmission coefficients the radiative and transport lifetimes can be well separated in the continuous-wave spectra. We have shown experimentally that at high carrier densities the super-resonant radiation dominates the energy losses in the system and that it can be well explained via a classical electrodynamic picture. Within this approach, the coherent emission is established via the coherent interaction of the incident radiation with a thin-film sample that is not sensitive to the details of the band structure. These results demonstrate that the superradiance in semiconducting thin films should be interpreted as a fully classical effect.

7. Band Structure Mapping of 2D Crystals

The electronic band structure provides an important fingerprint of a material in the reciprocal space. In case the surface of the sample is accessible experimentally, the standard technique of angle-resolved photoemission spectroscopy (ARPES) [3] is an established way to obtain the necessary information. However, in several cases, especially in 2D hetero-structures, several buffer or capping layers prevent collecting the data from the photo-emitted electrons. As possible alternative methods, the analysis of the cyclotron mass [126–129] or density of states via capacitance experiments [85, 130] have been suggested to recover the band dispersion, especially of 2D materials. In magneto-optical experiments [83, 131–134] the relevant information is obtained comparing the theoretical predictions [77, 135] of the band structure with experimental data.

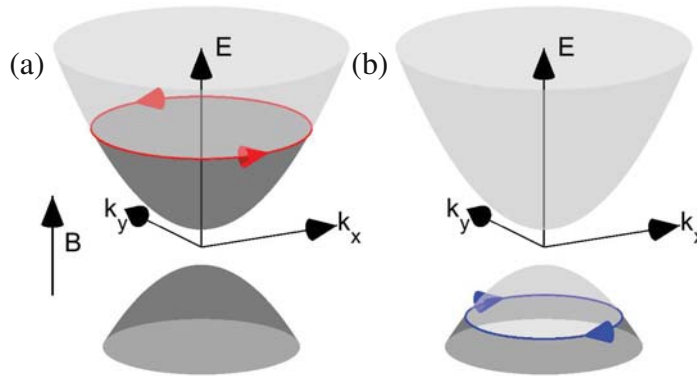


Figure 7.1: Illustration of the orbiting electrons in the band structure of a 2D semiconductor. The effective cyclotron mass of the electron at the Fermi level is related to the area inside the orbit A as Eq. (7.1). States in a conduction band (a) orbit in the opposite direction than states in a valence band (b) due to the different sign of dA/dE .

Within another approach, the band structure may be obtained from the analysis of the cyclotron resonance frequencies that is especially useful for 2D materials. Indeed, in two dimensions and in the quasi-classical approximation, the cyclotron frequency Ω_c may be written in terms of the cyclotron effective mass m_c as in Eq. (3.31) (see also

Chapter 3):

$$m_c \equiv \frac{eB}{\Omega_c} = \frac{\hbar^2}{2\pi} \frac{\partial A}{\partial E} \Big|_{E=E_F} . \quad (7.1)$$

The reader should be reminded that A is the area in the reciprocal space enclosed by the contour of the constant energy E (see Fig. 7.1). As discussed in Section 3.3, an important point is that the cyclotron frequency in Eq. (7.1) linearly depends on the external magnetic field independently of the form of dispersion relations, because the Fermi area is field-independent in the quasi-classical approximation. This approximation is the main assumption in the present experiments, i.e., transitions between several Landau levels should take place simultaneously [80, 129]. This condition is certainly realized at lower magnetic fields utilized in the present experiment.

In the general case, the relation between the area and the band structure may be complicated. In such cases an additional input from the theory is indispensable. If a 2D crystal has a rotationally-symmetric electronic band, we obtain from Eq. (3.11) at $T = 0$:

$$k_f = \sqrt{\frac{4\pi n}{D}} . \quad (7.2)$$

As discussed in Chapter 3, the isotropic approximation can be applied leading to a simple relation between the Fermi-vector k_F and the Fermi-area: $A = \pi k_F^2$. With this in mind, Eq. (7.1) can be rewritten as:

$$\frac{\partial E}{\partial k} \Big|_{E=E_F} = \frac{\hbar^2 k_F}{m_c} , \quad (7.3)$$

and, thus, can be directly integrated to obtain the experimental band structure $E(k)$. As we will see below, for the hole-like states, however, the isotropic approximation breaks down, and additional information from the theory is necessary to obtain the band structure. Possible approaches, in the present cases, are presented in Sections 7.1.1 and 7.2.1. The procedure illustrated above will be applied to a HgTe-based TI and two semi-metallic HgTe samples in Sections 7.1 and 7.2, respectively.

The data from the following section has been published in Ref. [136]. The theoretical band structures presented in Sections 7.1 and 7.2 were calculated within the $\mathbf{k} \cdot \mathbf{p}$ theory by E. G. Novik.

7.1 HgTe-Based Topological Insulator

In this section, we apply the procedure sketched above to a 3D TI HgTe and compare the results with the predictions of the $\mathbf{k} \cdot \mathbf{p}$ model. As described in detail in Chapter 4, the unstrained single-crystalline mercury telluride (HgTe) is a gapless semimetal with the conduction and valence bands formed by Γ_8 bands. If grown in the form of a thin film on a CdTe layer, HgTe is subject to a tensile strain due to lattice mismatch. As

a consequence, the originally degenerate light and heavy Γ_8 hole bands split at the Γ point, thus forming a bulk insulator with a gap around ~ 20 meV [79, 84] for a 80-nm-HgTe film. Due to a band inversion between HgTe and CdHgTe, topologically protected surface states arise in about 10-20 nm thick layer close to the boundary. HgTe films thus form a strong 3D TI. According to band structure calculations, the conduction band of an 80-nm-HgTe 3D TI is non-parabolaical and it is quantized due to the confinement. The valence band of the HgTe film reveals a deep minimum at the Γ point with four shallow side maxima along the $(\pm 1, \pm 1)$ directions (see Fig. 7.2). The minimum is due to the mixing between light and heavy-hole states in the inverted band structure of HgTe [97, 137].

As discussed in Chapter 5, the magneto-optical experiments were carried out on a strained 80-nm-thick HgTe film grown by molecular-beam epitaxy on a (100)-oriented GaAs substrate. The analysis of the cyclotron resonance corresponding to the upper surface state revealed the mobility to be up to $\mu = e\tau/m = 5 \cdot 10^5$ cm²/Vs. Due to the fact that the gate only partially covers the sample, we were not able to fully rely on the magneto-transport measurements. The ungated regions can significantly falsify the transport response. However, at zero gate voltage, this effect is minimized, thus allowing us to gather some additional information about the carriers in the system, as shown below. The cyclotron resonance was investigated in a Mach-Zehnder interferometer arrangement presented in Section 2.2.1. The data were obtained at several fixed frequencies in sweeping magnetic fields. Additional information about the charge carriers in the system was also obtained from the frequency-dependent spectra in zero magnetic field. To unambiguously separate the resonances from the electron-like and hole-like carriers, several experiments were conducted with circularly-polarized radiation. The experiments were carried out at 1.8 K in a split-coil superconducting magnet that provided magnetic field up to ± 7 T in the Faraday geometry. The measurements and the analysis were performed as discussed in Chapter 5.

7.1.1 Theoretical Model

To acquire a more detailed insight into the band structure of the strained HgTe layer, theoretical calculations have been done using a multiband $\mathbf{k} \cdot \mathbf{p}$ model [138] which takes into account the strong coupling between the lowest conduction and the highest valence bands. The $\mathbf{k} \cdot \mathbf{p}$ model considers eight bands: two Γ_6 , two Γ_7 and four Γ_8 subbands. Yet, considering the energy region of our interest, the contribution of the Γ_7 subband is below 1%. The calculations were done for a fully strained HgTe film with Cd_{0.7}Hg_{0.3}Te barriers which is grown on a CdTe substrate. The strain due to the lattice mismatch between HgTe and CdTe of about 0.3% leads to an opening of a direct gap of ≈ 22 meV (the indirect gap is about 10 – 15 meV) between the heavy-hole and light-hole bands in the HgTe layer [79]. The strain effects are taken into consideration by applying a formalism introduced by Bir and Pikus [139]. According to the previous studies of similar structures [79, 131, 140], the crossing point of the surface states is located below

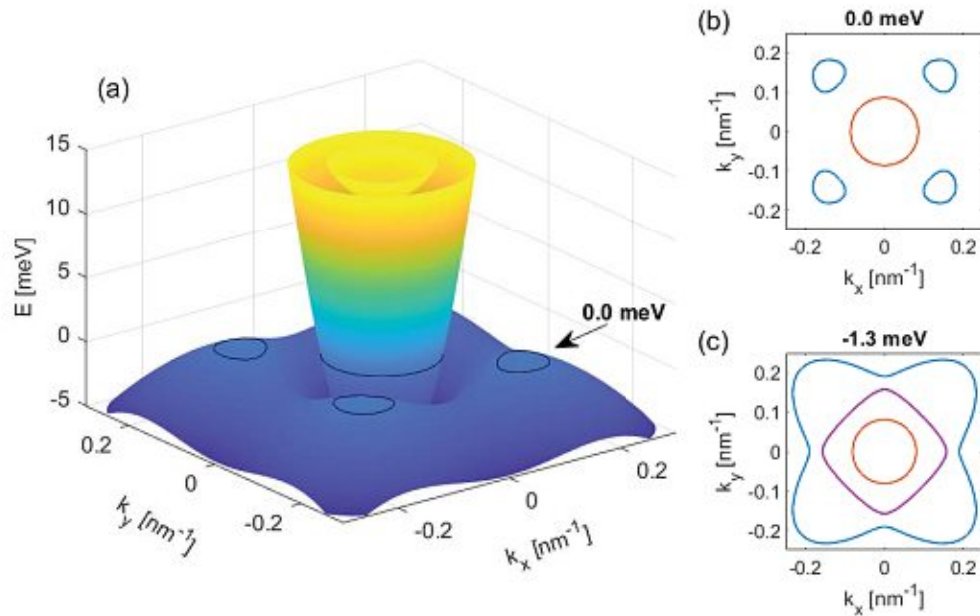


Figure 7.2: Theoretical band structure of a 3D TI HgTe. (a) The first valence band, the surface band and the first conduction band of the 80-nm-thick HgTe layer at the charge neutrality point $n_{tot} = 0$, where the concentrations of electrons and holes equal $\pm 1.2 \cdot 10^{11} \text{ cm}^{-2}$. (b) Cross-section of data in panel (a) at $E_F = 0$ meV. Blue - hole-like Fermi surface ($\partial A/\partial E < 0$) from the islands in the $(\pm 1, \pm 1)$ directions. Orange - electron-like Fermi surface ($\partial A/\partial E > 0$) from the surface states. (c) Fermi surface of the hole-doped sample where four islands are connected and lead to a different cyclotron picture: blue - hole-like, violet - electron-like, orange - electron-like.

the bulk bandgap. Accordingly, a full-band envelope function approach [141] is used to perform the self-consistent calculations of the Hartree potential. This procedure avoids the separation of the occupied electron and hole states which is complicated for structures where both are occupied simultaneously. The calculations include the structure inversion asymmetry (SIA) and, therefore, effectively reproduce the experimental effect of the applied gate. The spatial distribution of charge can be calculated while the total charge density is being varied. The Hartree potential determined by this spatial distribution of charge (see Eq. (2) in Ref. [141]) splits the bulk and surface states and leads to their realignment, resulting in significant band structure modifications (see Figs. 7.7 and 7.8, and the discussion below).

There is an ongoing debate in the literature about the influence of the interface inversion asymmetry (IIA) [142] on the band structure of HgTe structures. Several studies argue a sufficient effect of IIA in HgTe quantum wells grown on (013) substrates [63, 143, 144]. Moreover, theoretical calculations in Ref. [142] predict a gap of about 15 meV caused predominantly by IIA in (001) HgTe quantum wells of critical

thicknesses. However, experimental data [11, 80] do not confirm these predictions. Considering the complexity of the band structure of 80-nm HgTe layers and the missing experimental evidence of the influence of the IIA, these terms are not included in the calculations.

In an attempt to test further anisotropy terms in the Hamiltonian, the inclusion of the bulk inversion asymmetry [145] (BIA) term in calculation of the band structure at the charge neutrality point ($n_{tot} = 0$) was studied. As demonstrated in Fig. 7.3, the inclusion of this term strongly splits the valence bands and reduces the value of the gap. As the latter even worsens the agreement between theory and experiment (see Fig. 7.7 below), the BIA term was not used in the calculations of the band structure.

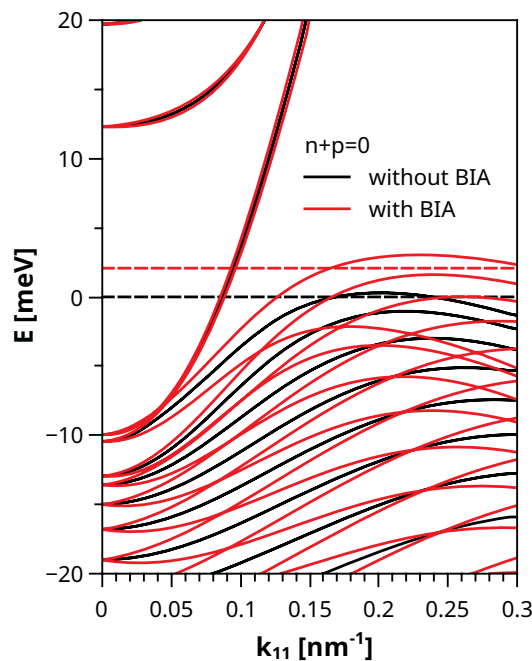


Figure 7.3: Band structure calculation at $n_{tot} = 0$ along the (1,1) direction. The results of the model used in the main text (black data) are compared to the calculated dispersion of the model that includes the BIA term. Dashed lines show the position of the Fermi level for the charge neutrality point. It can be seen that the influence of the BIA on the surface and electron-like states is relatively small. On the other hand, BIA increases the energy of the holes around valence band maxima.

The plots of the surface band, the first valence band (H2), and the first conduction band (H1) calculated using $\mathbf{k} \cdot \mathbf{p}$ model are shown in Fig. 7.2 for the case of the charge neutrality point: the densities of holes and electrons are equal and the total charge density equals $n_{tot} = 0$. Here, all three bands are spin-degenerate. In this case, the Fermi energy crosses the surface of valence bands thus forming four "islands" as shown in Fig. 7.2(b).

In the cyclotron signal, we expect an electron-like resonance due to the surface states

and a hole-like signal from the valence islands. After lowering the Fermi energy, the four regions of the valence band connect forming a ring structure as shown in Fig. 7.2(c). In this case, the fourfold "valley" degeneracy is lifted and each curve of the valence-band ring corresponds to a separate cyclotron resonance: a hole-like signal from the outer curve (blue) and an electron-like signal from the inner curve (violet). The latter effect is due to a different sign of $\partial A/\partial E$ in Eq. (7.1); positive curvature - electrons, negative curvature - holes. It should be noted that even in this case a separate surface resonance is expected that remains electron-like. The island-ring transition is present even if we take into account that the band structure deforms with varying density and that all bands are spin-polarized due to broken symmetry. After the Fermi surface is determined from the band structure calculations, the theoretical cyclotron mass can be calculated using the definition in Eq. (7.1).

To obtain the density dependence of the cyclotron mass within the present theory the effect of the applied gate was modeled by varying the total charge density in the system from $6 \cdot 10^{11} \text{ cm}^{-2}$ (holes) to $-6 \cdot 10^{11} \text{ cm}^{-2}$ (electrons) with the Fermi level reaching the valence and conduction subbands, respectively. For each value of the n_{tot} , the cyclotron mass was calculated using Eq. (7.1) as a function of density within the corresponding band.

Finally, the theoretical band structure confirms the rotational symmetry of both surface states and bulk conduction subbands, thus justifying the use of Eqs. (7.2) and (7.3) to connect the Fermi-vector and the cyclotron mass. On the other hand, the hole islands do not show this isotropic behavior. Nevertheless, at lower hole concentration the islands can be approximated as circles (see Fig. 7.2(b)) with an effective radius k_{eff} shifted by $k_0 \approx (\pm 0.15, \pm 0.15) \text{ nm}^{-1}$ from the Γ -point. In this case $k = k_{eff}$ in Eq. (7.3), where k_{eff} is related to the Fermi-surface area of each of the four islands as $A = \pi k_{eff}^2$. Of course, the exact relation between A and k_{eff} can be calculated from the theory. We believe, however, that a reasonable picture of the band structure can be obtained within an isotropic approximation as well. A direct comparison between theory and experiment can be done using an approximation-independent plot of cyclotron masses vs. density (see Fig. 7.6 below). This presentation is not sensitive to approximations done in Eqs. (7.2) and (7.3).

7.1.2 Results and Discussion

Fig. 7.4 shows typical field-dependent transmission in the geometry with circularly-polarized radiation. The advantage of this geometry is the clear separation of the electron (e) and hole (h) resonances as they are observed for positive and negative external magnetic fields. The inset in Fig. 7.4 demonstrates linear field dependence of the cyclotron resonance frequency ($\omega = 2\pi\nu$) thus verifying the applicability of the quasi-classical approximation in Eqs. (7.1) and (7.3). The data at the low frequency (142 GHz), shown in Fig. 7.4(a), are most sensitive to the overall behavior of the charge carriers as,

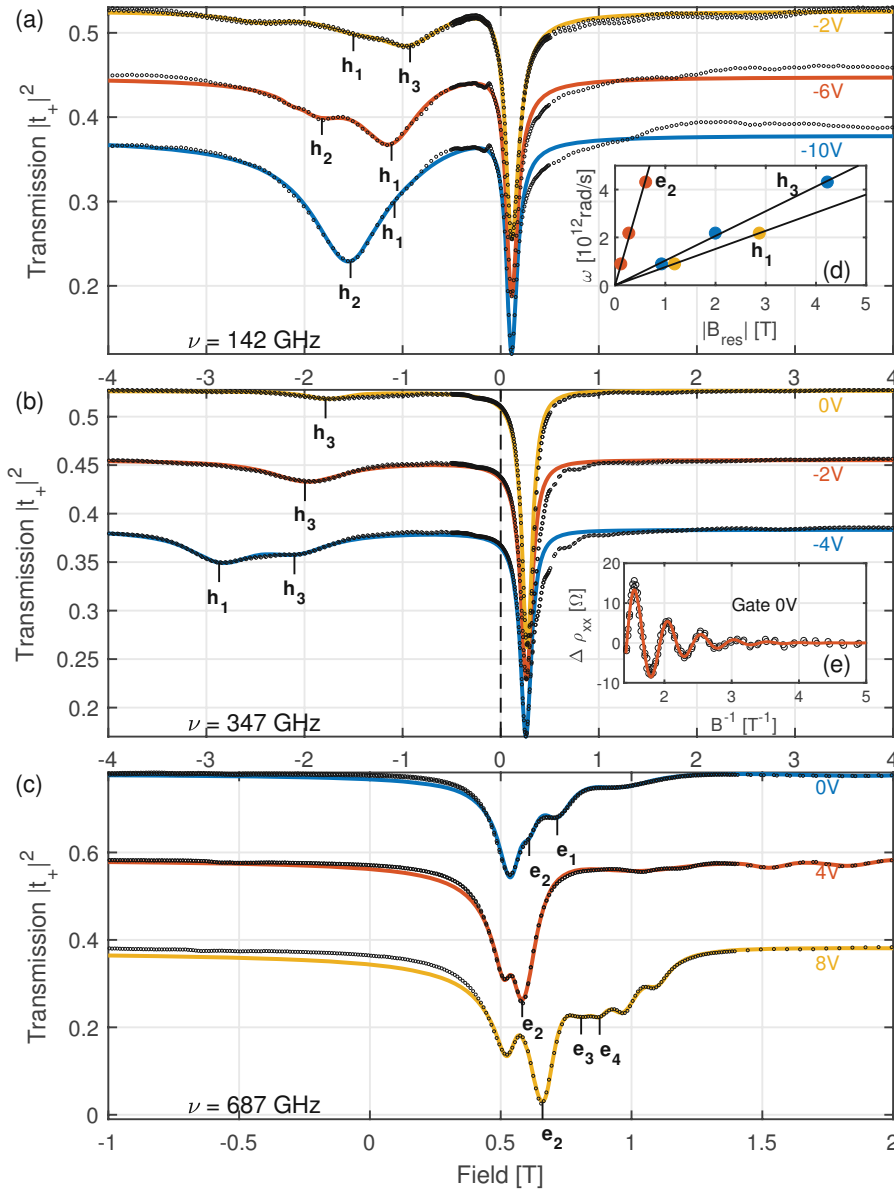


Figure 7.4: Cyclotron resonance with circularly-polarized light. (a-c) The intensity of the transmitted radiation $|t_+|^2$ as a function of the external magnetic field for fixed frequencies as indicated. Resonance features for positive and negative fields correspond to electrons and holes, respectively. Points - experiment, solid lines - theoretical model based on the transmission formulas and the Drude conductivity (see Section 5.2). The absolute scales refer to the lowest curves, others are shifted for clarity. The inset (d) shows the field dependence of the cyclotron resonance demonstrating linear behavior within the quasi-classical approximation according to Eqs. (7.1) and (7.3). (e) The oscillating part of the longitudinal resistivity at zero gate voltage. The experimental data (black circles) were fitted by a single-carrier Lifshits-Kosevich model (Eq. (3.47)) (orange line).

here, electrons and holes may be easily observed simultaneously and they indeed can be well separated for $U_g = -10$ V curve. For large negative voltages, the Fermi energy is situated in the valence band. The cyclotron signal from the hole-like carriers can be observed in the gate voltage range from -10 V to 0 V. This correlates with the position of the charge neutrality point that has been estimated from the resistivity measurements: the longitudinal resistivity ρ_{xx} showed a maximum at around -3 V. With increasing gate voltage the single resonance of the electrons reveals a distinct structure that is most clearly seen in the data at 687 GHz, Fig. 7.4(c).

The transmission curves can be fitted well using the procedure presented in Section 5.2 (solid lines in Fig. 7.4). From the analysis of the resonances in the transmission, we obtain the 2D charge density, effective cyclotron mass, and the scattering time for each separate carrier type. A gradual increase of density with increasing gate voltage is expected for electrons. Similarly, the density of the hole-like carriers must be a decreasing function of the gate voltage. Therefore, in the analysis of the band structure, only the resonances caused by carriers with monotonous gate-voltage dependence of the charge density were taken into account. For completeness, the electrodynamic parameters of the remaining resonances are given in the Supplemental Material of Ref. [136]. We believe that the majority of the additional peaks represents direct transitions between Landau levels and thus cannot be described via the quasi-classical approximation using Eqs. (7.1) and (7.3). For example, carriers h_1 and h_3 in Fig. 7.4 showed a non-monotonous gate-voltage dependence of density and were therefore not considered in the band structure analysis. Nevertheless, we were able to recognize them at multiple frequencies, showing a characteristic behavior of charged carriers in our model. Currently, the gate voltage dependence of the intensity of these modes cannot be used to extract their density, since their behavior goes beyond the quasi-classical approach.

Fig. 7.5 shows the parameters of the cyclotron resonances that will be used to obtain the band structure of the 3D TI. The charge density decreases with the gate voltage for holes and increases for electrons. Both agree with the sign of the charge carriers obtained directly from the spectra in Fig. 7.4.

Additional information about the carriers in the sample was gathered by four-point longitudinal resistivity measurements at zero gate voltage, which displayed strong Shubnikov-de Haas (SdH) oscillations (Section 3.3) as plotted against the reciprocal magnetic field in Fig. 7.4(e). The Lifshits-Kosevich formula (Eq. (3.47)) can be used to extract the carrier properties from the oscillation period. A model with a single carrier type fits the experimental data reasonably well (see orange curve in Fig. 7.4(e)). The oscillation frequency f can be transformed into the carrier density by $n_{SdH} = efD/h$ (Eq. (3.46)), where D represents the degeneracy of states. Assuming a double-degenerate state ($D = 2$), we obtained $n_{SdH} = 0.98 \cdot 10^{11} \text{ cm}^{-2}$. As seen in Fig. 7.5(e), $\frac{n_{SdH}}{2}$ overlaps with the densities of carriers e_1 and e_2 . As discussed below, these carriers can be attributed to bottom and top surface states, respectively. Note that SdH oscillations are mostly sensitive to the carriers density n . In the present case, the magneto-

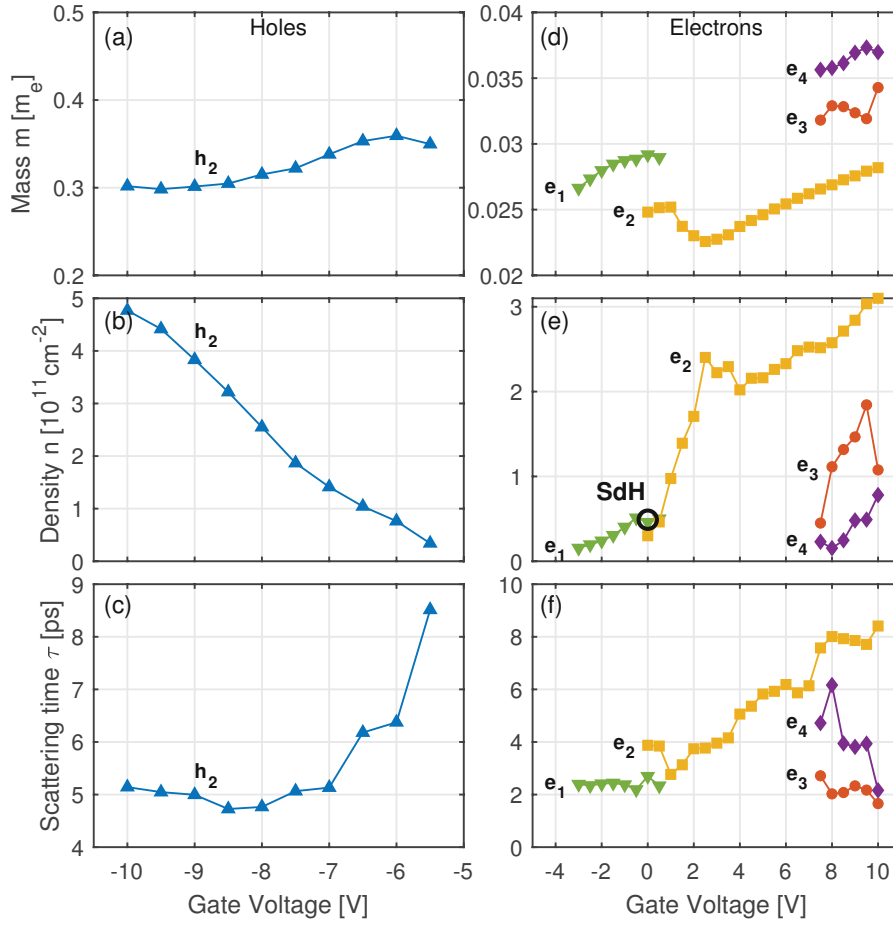


Figure 7.5: Electrodynamic parameters of the cyclotron resonances in HgTe. (a-c) – hole-like carriers, (d-f) – electron-like carriers. Only the most relevant resonances which may be explained via quasi-classical picture are shown. Colored symbols are experimental data from the fits of the spectra in Fig. 7.4. Black circle corresponds to the density $\frac{n_{SdH}}{2}$ resulting from the SdH analysis from Fig. 7.4(e). The lines are guides to the eye.

transport signal does not show any clear indication of the presence of two carrier types with different densities. In fact, Landau filling factors $\nu = n_{SdH}/(B_{min}e/h)$ at the minima of ρ_{xx} seems to give odd values ($\nu = 7, 9, 11, 13, 15$), which is a characteristic signature of a double-degenerate Dirac system [11, 81, 146].

To compare theory and experiment without using isotropic approximation, the cyclotron mass can be plotted directly as a function of the 2D density. This presentation is given in Fig. 7.6, where the $\mathbf{k} \cdot \mathbf{p}$ predictions are shown with empty symbols and the experimental results with full symbols.

The theoretical points were obtained for a discrete number of n_{tot} as discussed in Section 7.1.1. The scattering in the theoretical data comes from several effects: (i) numerical integration of the area A in Eq. (7.1) with a discrete number of \mathbf{k} -points (ii) from

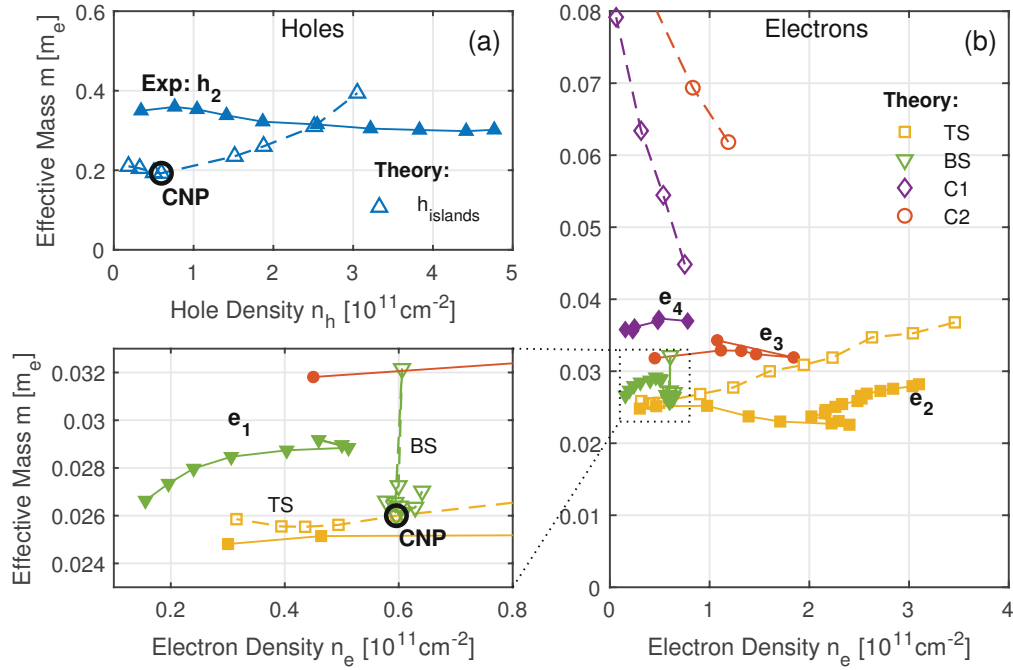


Figure 7.6: Comparison of the cyclotron masses in strained HgTe with $\mathbf{k} \cdot \mathbf{p}$ model calculations. Compared to Fig. 7.5 the cyclotron masses are plotted as a function of density. This presentation allows the comparison with the theoretical model without integrating Eq. (7.3). (a) hole-like carriers. (b) electron-like carriers. Full symbols - experimental values, empty symbols - theory, BS - bottom surface states, TS - top surface states, C1, C2 - spin-polarized bulk conduction bands, CNP - charge neutrality point.

the anti-crossings of the subbands, and (iii) from a finite value of the lateral lattice constant ($a = 1$ nm) in the full-band envelope-function approach used for the self-consistent calculations.

We note that the approximate density-independence of the majority of the observed carriers in Fig. 7.6(a,b) suggests that the dispersion relations will have a parabolic-like shape. Indeed, inserting $E = \hbar^2 k^2 / 2m_c$ into Eq. (7.3) gives the momentum and density-independent cyclotron mass $m_c = eB / \Omega_c = \text{const}(n, k_F)$. However since hybridization of multiple subbands takes place in the system, we do not expect a simple parabolic band structure, but one with higher-order corrections.

Comparing the experimental points (solid symbols in Fig. 7.6(a)) with theoretical predictions, we recognize the h₂-carriers as the fingerprint of the first spin-polarized valence band with four degenerate islands pockets in the band dispersion. Apparently, within the gate voltage range of the present experiment, we did not reach the region of the ring-like Fermi surface nor the rest of the valence subbands at lower energies. Most likely, this is due to the flatness of the band structure at the transition point which leads to small values of $\partial E_F / \partial U_g$. Experiments in quantizing magnetic fields previously showed a transition line involving the hole Landau level in a 20 nm sample [147]. Nevertheless,

our results exhibit the first detection of a hole-carrier in a 3D TI by quasi-classical cyclotron resonance analysis.

Experimental values show fairly flat behavior of the hole mass versus its density, while the theoretical values are slightly increasing. The weak increase was as well experimentally and theoretically observed for much thinner samples ($d \leq 20$ nm) [63]. Currently the reasons behind the mismatch between experiment and theory are not clear. Two factors can impact the experimental values here: (i) the experimental data for holes were obtained at high values of the gate, which leads to deformation of the band structure and (ii) due to relatively low hole density and high magnetic fields (~ 1.5 T) we are approaching the limit where transitions between single Landau levels start to dominate.

Fig. 7.6(b) shows the comparison of the cyclotron mass of the electron-like carriers with model calculations. We start with the analysis of the theoretical mass-density relations of the surface states that are marked by TS (top surface) and BS (bottom surface). The density of the TS states (yellow open squares) can be changed by applying the gate voltage within the full range of Fig. 7.6(b). We observe approximate density independence of the cyclotron mass for the top surface states supporting the parabolic-like form of the surface band. We interpret the experimentally determined carriers e_2 (yellow full squares) as the top surface carriers as their parameters are close to the results of the theory.

On the contrary, the theoretical model predicts only weak variation of the electron density at the bottom surface as a function of doping (green open triangles, magnified part of Fig. 7.6(b)), which is due to screening of the potential by the top surface (see also Fig. 7.8). In the same mass range, we observe the carriers e_1 (green full triangles) that probably correspond to the electrons on the bottom surface. Looking back at Fig. 7.5(d), we observe that the carriers e_3 are possibly a continuation of e_1 . Therefore, we interpret e_3 as the bottom surface carriers as well. The gap between these two carriers in Fig. 7.5(d) might be the result of a dominating cyclotron signal by the top surface carriers e_2 at the gate voltages between +1 and +7 V.

The $\mathbf{k} \cdot \mathbf{p}$ model predicts that the bottom of the bulk conduction band can be reached at high electron densities. For such high voltages not only the top and bottom surfaces are strongly split, but also the spin degeneracy of the conduction band is lifted (see Fig. 7.7(c)). Thus the theory predicts two cyclotron resonances from the bulk conduction band in the relevant doping range that are shown in Fig. 7.6(b) by open diamonds (C1) and open circles (C2). Comparing these predictions with the experiment, we suggest that carriers e_4 correspond to bulk conduction electrons C1.

Finally, we note that within an alternative description the electron-like signals e_3 and e_4 could be identified as C1 and C2, especially since they were observed simultaneously as soon as the Fermi level in the system reached the conduction bands. However, this interpretation provides a less convincing agreement between theory and experiment.

To access the experimental band structure of the HgTe film, the charge density of electrons is transferred to the electron momentum using the relation Eq. (7.2). According

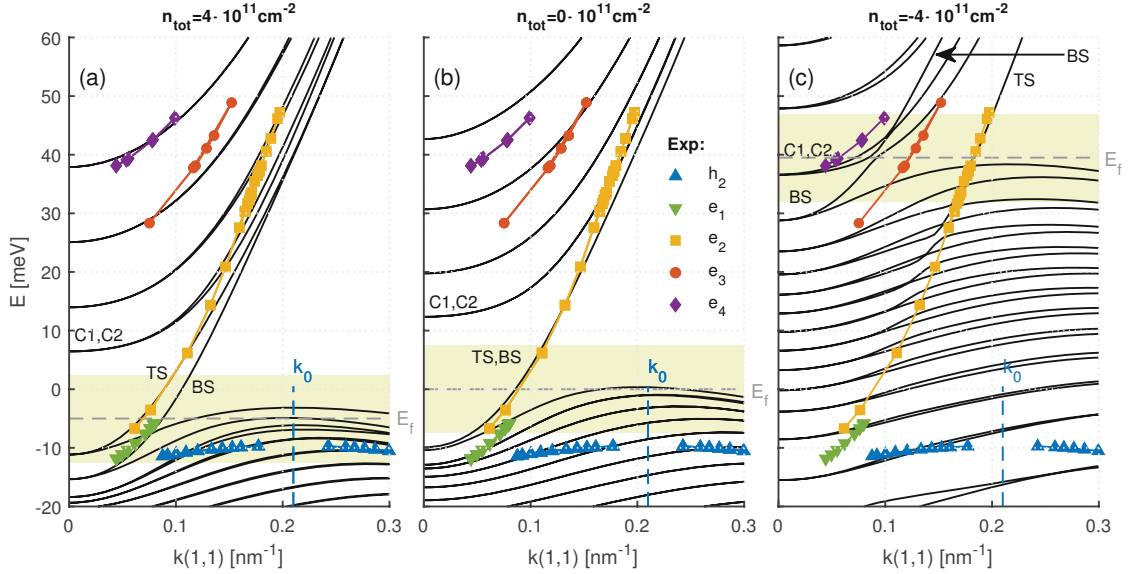


Figure 7.7: Band structure of the 3D TI based on a strained HgTe along the (1,1) direction. Symbols - experimental data obtained from cyclotron mass, solid lines are predictions of the $\mathbf{k} \cdot \mathbf{p}$ model for three values of the total charge density: (a) hole doping $n_{tot} = 4 \cdot 10^{11} \text{ cm}^{-2}$, (b) charge neutrality $n_{tot} = 0$ and (c) electron doping $n_{tot} = -4 \cdot 10^{11} \text{ cm}^{-2}$. Areas highlighted in yellow present the regions, where it is valid to compare experimental results with theory.

to the identification of the carriers above, we assume single degeneracy ($D = 1$) for all electron-like carriers. We classified h_2 hole-carriers as fourfold valley degenerate and spin-polarized hole-pockets states, thus taking $D = 4$. According to the model calculations, the four local maxima of the valence band are expected at finite wavevector, $k_0 \approx (\pm 0.15, \pm 0.15) \text{ nm}^{-1}$. The maximum of the experimental valence band has been shifted by this value. As pointed out in Section 7.1.1, for hole-like carriers we calculate the k -vector along the (1,1) direction as $k = k_0 \pm k_{eff}$ with $k_{eff} = \sqrt{\pi n}$.

The band dispersion, calculated within the approximation above, is shown in Fig. 7.7 as solid symbols. Direct integration lacks in providing the absolute energy position of the bands. Since we assume that the gate voltage defines a constant Fermi level in the film, the bands are vertically aligned to each other by referring to the gate voltage at which they were mutually detected.

In Fig. 7.7 we plot the theoretical band structure for three different doping ranges: (a) hole-doped regime with $n_{tot} = +4 \cdot 10^{11} \text{ cm}^{-2}$, (b) undoped regime with $n_{tot} = 0$, and (c) electron-doped regime with $n_{tot} = -4 \cdot 10^{11} \text{ cm}^{-2}$. The external electric field created by the applied gate drastically influences the energy spectrum, as seen in Fig. 7.7. This variation of the band dispersion can be well understood taking into account the spatial distribution of the probability density of different states and the spatial dependence of the Hartree potential. These dependencies are shown in Fig. 7.8. The yellow, blue, and

red curves show the Hartree potential for the same hole, neutral, and electron-dopings as in Fig. 7.7(a-c). The solid and dashed violet lines represent the probability distribution of the bottom (BS) and top (TS) surface states, respectively, at $n_{tot} = 0$. While varying n_{tot} does alter the distribution functions, the positions of the distribution maxima remain almost unchanged. Therefore, it is clearly evident that Hartree potential influences the top and bottom surfaces differently when $n_{tot} \neq 0$. It is well seen, that at the position of the BS the Hartree potential barely changes with n_{tot} , a consequence of the screening by all other carriers. This explains the weak gate dependence of the BS parameters in Fig. 7.6.

On the other hand, the TS experiences the strongest influence from the varying gate potential being easily split from the BS and shifted in energy in the band diagram. The latter is mostly evident at the positive gate voltages corresponding to electron-doping with $n_{tot} = -4 \cdot 10^{11} \text{ cm}^{-2}$. The value of the Hartree potential at the position of the TS is around -40 meV . This value directly corresponds to the shift of TS with respect to the E_F , when comparing the undoped and the electron-doped regime presented in Fig. 7.7(b,c). Similar shifting occurs for the conduction and valence bands. However, the shifting amplitudes are smaller since the maxima of the corresponding wavefunctions lie in the bulk. The overlap between the bulk valence and TS wave functions leads to multiple crossings and anticrossings of their dispersion curves.

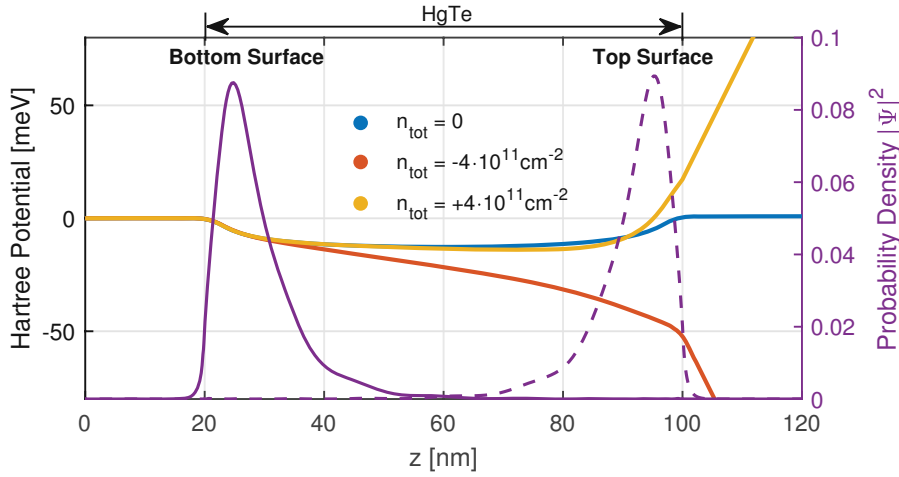


Figure 7.8: Hartree potential and spatial distribution of the wave functions for the top and bottom surface states. Hartree potential (left axis) at neutral, electron and hole dopings that is self-consistently determined as described in Section 7.1.1. The spatial probability distribution (right axis) of the surface states at $n_{tot} = 0$ is superimposed on the Hartree potential.

The variation of the gate voltage leads to shifting of the characteristic band energies and to the splitting of the bands that were degenerate at $n_{tot} = 0$. Therefore, the comparison between experiment and theory is valid in the vicinity of E_F only, with $E_F = E_F(n_{tot})$ being the Fermi level of the system. Three regions around Fermi energy corresponding to electron-doping, hole-doping, and the charge neutrality are shown by

yellow shaded areas in Fig. 7.7(a-c) and they are defined by $E = E_F \pm 7.5$ meV. Also, $U_g = 0$ V and the charge neutrality point do not coincide due to impurity doping - the experimental charge neutrality was found at $U_g = -3$ V.

We start the discussion of the band structure with the region close to the charge neutrality point, shown in panel (b). Here, according to theory, the bands are spin-degenerate and the size quantization of the valence and conduction bands is seen. As the Fermi energy lies in the vicinity of zero, the active states are expected to be the surface states and the valence band holes. In the experiment, however, we have detected only the TS states. These states are marked as e_2 and their dispersion fits well to the theoretical predictions without additional free parameters. On the other hand, e_1 and h_2 appeared at lower energies as the theory predicts.

In the hole-doped region, Fig. 7.7(a), we focus only on the data at lower energies. Here both in the experiment and theory, we observe a clear splitting of the surface bands. These results are denoted as TS and BS in the model and they correspond to e_2 and e_1 carriers, respectively. The reasons behind the vertical misalignment between the experimental and theoretical valence bands and the resulting increase of the indirect bandgap remain unclear. Within our procedure the energy position of the h_2 state cannot be shifted as it is fixed by the values of the gate voltage. Here we would like to note that the inclusion of the BIA terms in our theoretical model resulted in an increase of the energy at which the valence holes appear and therefore an even greater mismatch with the experiment (see Fig. 7.3).

In the predominantly electronic doping regime shown in Fig. 7.7(c), the e_2 surface band nicely overlaps with the theoretical top surface band, which is subject to hybridization and crossings/anti-crossings with several valence subbands. As discussed above, we attribute the carriers e_3 (solid red circles) to the bottom surface band and the carriers e_4 to one of the spin-polarized conduction bands (marked as C1).

To conclude, in addition to two spatially separated surface bands in Fig. 7.7, the bulk valence, and conduction bands are accessed within the present experiment. Although the band structure is strongly influenced by the gate voltage, we observe reasonable coincidence between the $\mathbf{k} \cdot \mathbf{p}$ model and the cyclotron resonance data. We recall that in the theoretical model all parameters are fixed by the known film structure and by the doping level of the layers.

7.1.3 Summary

The study of the cyclotron resonances in the magneto-optical data allowed probing the top and bottom surface states and separate modes that correspond to bulk conduction and valence bands in a 3D TI based on HgTe. The quasi-classical approach is utilized to recover the parameters of the charge carriers, which is approved by the linearity of the cyclotron frequency in external magnetic fields. Within this approximation, the band structure can be extracted from the gate dependence of the magneto-optical spectra.

Considering the obvious effect of the asymmetric gating potential on the sample, the experimental band structure agrees reasonably well with the predictions of the $\mathbf{k} \cdot \mathbf{p}$ model, however, when the Fermi-level is shifted to the valence band, clear deviations between theory and experiment are observed. All electronic charge carriers showed a single degeneracy of states, while the spin-polarized hole states demonstrated a valley degeneracy of four.

7.2 Semimetallic HgTe Samples

Let us recap what we have learned in Chapter 4. Quantum wells based on strained HgTe films have been studied extensively in recent years due to the emergence of numerous exotic properties. These arise due to the band inversion in bulk HgTe, where the Γ_6 and Γ_8 bands shift positions in the energy spectrum. If a 3D HgTe bulk layer is grown on a CdTe substrate, tensile strain due to lattice mismatch splits the originally degenerate light and heavy Γ_8 hole bands at the Γ point, thus forming a bulk insulator. Due to the inverted bands at the interface between HgTe and CdTe, the topologically protected surface states arise in about 10-20 nm thick layer close to the boundary. In the case the thickness of the HgTe film is above ~ 50 nm this results in a 3D TI. Thinner samples represent unique examples of 2D semi-metals, where electrons and holes coexist simultaneously [9].

Several studies of HgTe samples with thicknesses between 8 – 21 nm [63, 148–152] concluded that while the measured properties of the conduction band agree well with the theoretical models the valence band spectrum does not. The results have generally shown the valence subbands being strongly anisotropic, forming four local maxima at non-zero k -values, with an overlap of a few meV with the rotationally symmetric conduction subband. However, the mismatch between the experimental data, such as the precise band overlap and hole effective mass, with their corresponding calculated values indicated that the theoretical approach to this problem is not fully established. Moreover, recent experiments on samples with (013) surface orientation [63] suggested a two-fold valley degeneracy of the top valence subbands.

In this section, we investigate two HgTe thin films with thicknesses of 14.1 and 22 nm by the analysis of the cyclotron resonance frequencies. The experimental data were measured with the Mach-Zehnder interferometer from Section 2.2.1. The HgTe films were grown by molecular-beam epitaxy on a (013)-oriented substrate. Similar to Section 7.1, applying the technique from the beginning of this chapter allowed us to directly obtain the band structures of these 2D systems. The analysis of the SdH oscillations seen in the capacitance of the samples gave additional insight into the properties of the charge carriers in the system, specifically the experimental determination of the state degeneracies. With both experimental techniques, we were able to probe the top valence subband states, the first conduction subband, and even the subsequent second conduction subband. The experimental results of the cyclotron frequency analysis and magneto-

transport measurements were compared with the $\mathbf{k} \cdot \mathbf{p}$ models for both samples and gave generally a great overlap. Primarily, the experimentally suggested two-fold degeneracy of the holes agrees with the proposed theoretical model, in which the combination of the BIA and the SIA leads to a C_2 -symmetry of the valence subband islands.

As presented in detail in Chapter 5, the data were obtained at several fixed frequencies in sweeping magnetic fields. Additional information about the charge carriers in the system was also obtained from the frequency-dependent spectra in the zero magnetic field. To distinguish the resonances from the electron-like and hole-like carriers, most experiments were conducted with circularly-polarized radiation. The experiments were carried out at 1.8 K in a split-coil superconducting magnet that provided an external magnetic field up to ± 7 T in the Faraday geometry. The analysis of the obtained experimental data was performed as described in Section 5.2.

7.2.1 Theoretical Model

Similarly to Section 7.1.1, the band structure of the strained HgTe QWs has been calculated using eight-band $\mathbf{k} \cdot \mathbf{p}$ model in an envelope function approach [138], which includes the coupling between the lowest conduction band Γ_6 and the topmost valence bands Γ_8 and Γ_7 . Assuming that HgTe QWs are grown on a CdTe substrate, strain effects due to the lattice mismatch between HgTe and CdTe were taken into account applying the Bir-Pikus formalism [139]. A method of generalization of the $\mathbf{k} \cdot \mathbf{p}$ model for structures grown on high-index-planes [153] has been used to include additional terms, which are responsible for coupling of states for the (013) growth direction of the QWs, into the Hamiltonian.

The band structure calculations have been done taking into account the SIA and BIA. In accordance with Section 7.1.1, IIA was not included in this model. Whereas in the experiment carrier density in the QW is tuned by the gate voltage, in the model, the variation of the doping in the top barrier is assumed, while the doping in the barrier on the substrate side is taken to be constant. Asymmetric barrier doping results in the asymmetric distribution of the Hartree potential, which has been determined self-consistently by solving the eigenvalue problem and Poisson equation for the 2D charge carriers in the QW [138]. BIA of the zinc-blende crystal structure gives rise to the Dresselhaus spin-orbit interaction. Here, BIA terms linear in momentum for the valence bands Γ_8 and Γ_7 and the terms quadratic in momentum originating from the coupling between the conduction and valence bands [154] were taken into account. The interplay of the SIA and BIA terms results in an anisotropy of the spin splitting, i.e. the spin splitting depends on the direction of the in-plane momentum [155], which contributes to the anisotropy of the energy dispersion.

To obtain the density dependence of the cyclotron mass within the present theory the effect of the applied gate was modeled by varying the total charge density in the system from $5 \cdot 10^{11} \text{ cm}^{-2}$ (holes) to $-12 \cdot 10^{11} \text{ cm}^{-2}$ (electrons). For each value of the n_{tot}

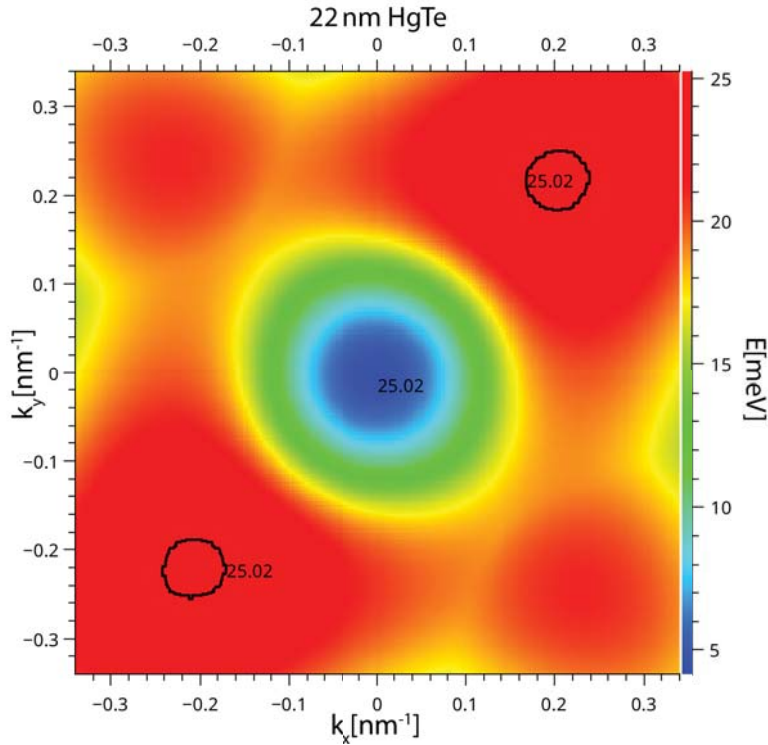


Figure 7.9: Theoretical contour plot of the first valence subband of a 22-nm-HgTe quantum well at $n_{tot} = 0$, calculated in terms of Section 7.2.1. Black markers indicate that close to the valence subband maxima, the Fermi surface can be approximated by circles, which are shifted from $k = (0, 0)$.

the cyclotron mass was calculated using Eq. (7.1) as a function of density within the corresponding bands.

In correlation with the theoretical studies of the 80-nm sample in Section 7.1.1, the theory confirms the rotational symmetry of conduction subbands H1 and E2 in the energy region of interest, justifying the use of Eqs. (7.2) and (7.3). On the other hand, the valence bands show strongly anisotropic behavior, see Fig. 7.9, demonstrating two pronounced maxima ("islands") in the first valence subband H2. At low hole concentrations, the Fermi surfaces of the islands can be approximated by circles with an effective radius k_{eff} shifted by $k_0 = (0.17, 0.17) \text{ nm}^{-1}$ from the Γ -point. Then $k = k_{eff}$ in Eq. (7.3) is related to the Fermi-surface area of each of the two islands as $A = \pi k_{eff}^2$. We would like to stress that a direct comparison between theory and experiment can be done using a plot of cyclotron masses vs. density (see Fig. 7.15 below) which is independent on the approximations done in Eqs. (7.2) and (7.3).

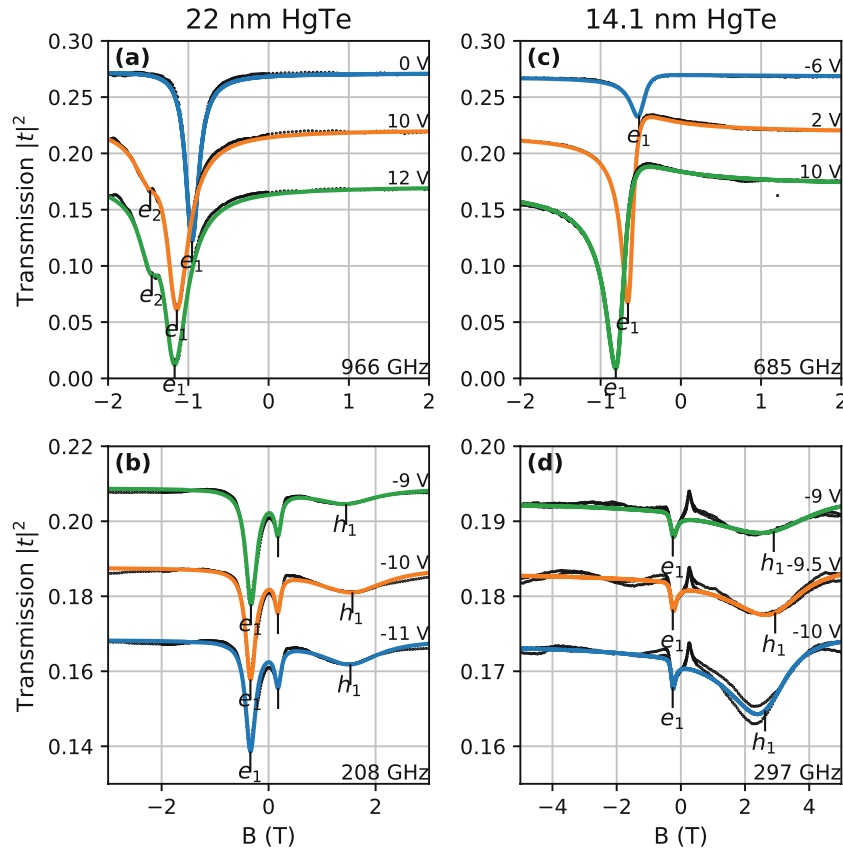


Figure 7.10: Cyclotron resonance with circularly-polarized light. The intensity of the transmitted radiation $|t_+|^2$ through the 22-nm (a,b) and the 14.1-nm sample (c,d) as a function of the external magnetic field for fixed frequencies as indicated. Resonance features for positive and negative fields correspond to holes and electrons, respectively. Black points - experiment, solid lines - theoretical model based on Drude conductivity, see Section 5.2. The absolute scales refer to the lowest curves, others are shifted for clarity.

7.2.2 Results and Discussion

Fig. 7.10 shows several spectra of field-dependent transmission in the geometry with circularly-polarized radiation for both samples under investigation. Below ~ 6 V we observed a hole cyclotron resonance (h_1) at several operating frequencies for both samples. In the entire region of the applied gate voltage, we have observed an electronic cyclotron resonance which we recognized as being a result of the carrier e_1 . In the case of the 22-nm sample, at higher frequencies (698 and 966 GHz), which provide a higher resolution of the cyclotron mass, we have observed an appearance of an additional contribution above $U_g > 9$ V, which we identified as carrier e_2 .

Here, we would like to note that several transmission spectra showed additional con-

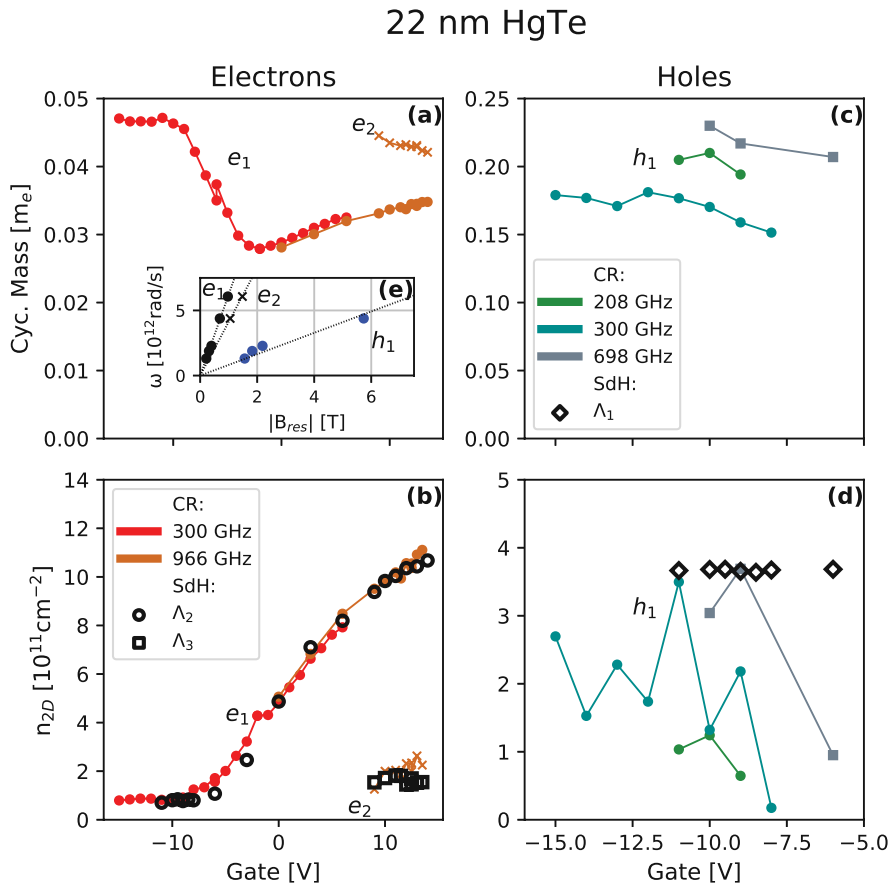


Figure 7.11: Electrodynamic parameters of the cyclotron resonances in 22-nm-HgTe sample. Colored symbols are experimental data from the fits of the spectra in Fig. 7.10. Black empty symbols correspond to the carrier concentration resulting from the SdH analysis from Fig. 7.14. The inset (e) shows the field dependence of the cyclotron resonance demonstrating linear behavior within the quasi-classical approximation according to Eqs. (7.1) and (7.3).

tributions in positive fields (see for example Fig. 7.10(b) at ~ 0.1 T). We recognize these as mirror peaks of the e_1 cyclotron resonance, a consequence of non-ideally circularly-polarized incident radiation. Additionally, several anti-symmetrical mirrored peaks were observed (see Fig. 7.10(d) between ± 0.5 T), for which the source is still unclear.

The transmission curves can be fitted well using the procedure presented in Section 5.2 (solid lines in Fig. 7.10). From the analysis of the resonances in the transmission, we obtain the 2D charge density n , effective cyclotron mass m , and the scattering time τ for each separate carrier. In quasi-classical physics, it is expected that the electron density increases with increasing gate voltage. Similarly, the density of the hole-like carriers must be a decreasing function of the gate voltage.

Figs. 7.11 and 7.12 show the parameters of the cyclotron resonances at some of

14.1 nm HgTe

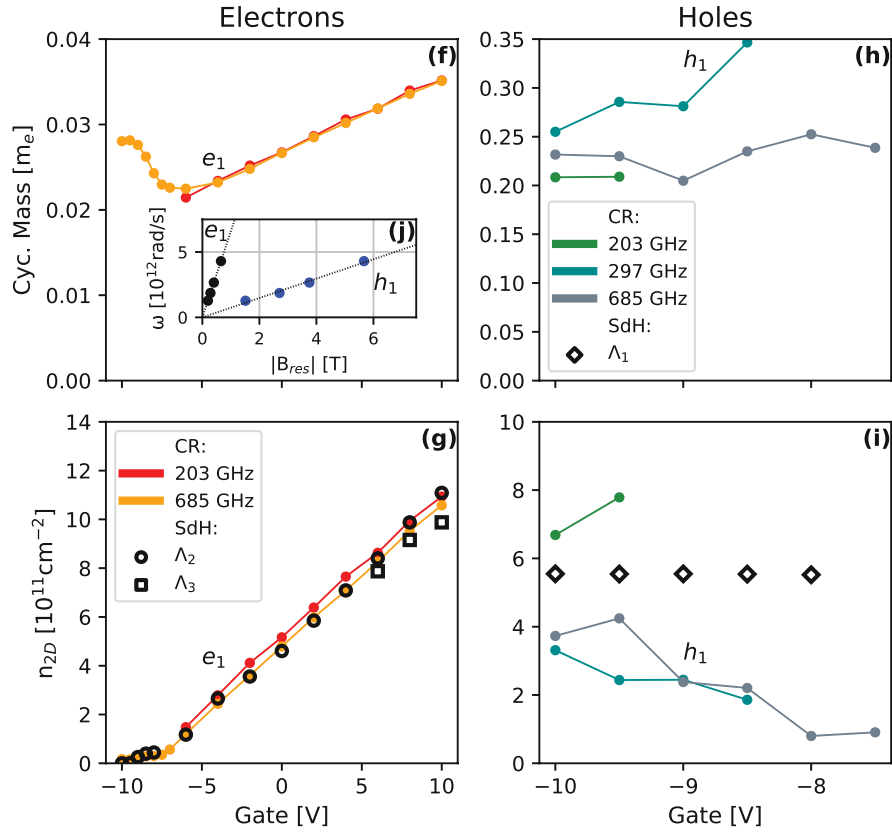


Figure 7.12: Electrodynamical parameters of the cyclotron resonances in 14.1-nm-HgTe sample. Colored symbols are experimental data from the fits of the spectra in Fig. 7.10. Black empty symbols correspond to the carrier concentration resulting from the SdH analysis from Fig. 7.14. The inset (e) shows the field dependence of the cyclotron resonance demonstrating linear behavior within the quasi-classical approximation according to Eqs. (7.1) and (7.3).

the operating frequencies of radiation for both samples, respectively. Data obtained at various frequencies overlap well in the case of electrons. On the other hand, holes are characterized by heavier masses, lower carrier density, and mobility. These factors result in much weaker cyclotron signatures in the transmission spectra. The analysis of the hole cyclotron resonances becomes affected by the noise level, time-related drifts, and other artifacts, resulting in larger fitting errors. We would also like to note that due to low hole densities and high resonant magnetic fields transitions between single Landau levels may hinder the measured resonances. Nevertheless, as seen in Fig. 7.11(e) and Fig. 7.12(e), all carriers demonstrated a linear behavior of the cyclotron frequency ($\omega = 2\pi\nu$) in respect to the resonance field ($B_{res} = m\omega/e$), satisfying the quasi-classical approach in Eq. (7.1). Fig. 7.11(a) and Fig. 7.12(a) show a gradual increase

of the effective mass of e_1 above ~ -5 V. At lower voltages, the mass increases with decreasing gate until it stabilizes at around -8 V for both samples. The effective mass of carrier e_2 decreases with gate, while the mass of h_1 is approximately constant for both samples (Fig. 7.11(c) and Fig. 7.12(c)). The charge density generally decreases with the gate voltage for holes and increases for electrons. Both agree with the sign of the charge carriers obtained directly from the spectra in Fig. 7.10.

Electron mobilities $\mu = e\tau/m$ of the carriers e_1 are plotted in Fig. 7.13 for both samples. The small increase of mobility below -8 V can be attributed to the appearance of holes in the system since the impurity scattering of electrons is screened by the holes [148, 149]. The mobility increases up to around 0 V for the 22-nm sample and around 5 V for the 14.1-nm sample due to the increase in density of the carriers. We attribute the following decrease in mobility above 0 V of the 22-nm sample to the inter-band scattering due to the appearance of carrier e_2 . Similar behavior is observed for the thinner sample, suggesting that an additional band was near, but was not reached due to the safety limitation of the applied gate voltage. The fact that all three parameters of e_1 almost stabilize below -8 V suggests a substantial decrease of $\partial E_F/\partial U_g$. We assume this to be a consequence of the Fermi level entering the flat valence band with a high density of states. Additionally, at high amplitudes of gate voltage, the effect of the gating potential on the electronic state of the sample can become saturated.

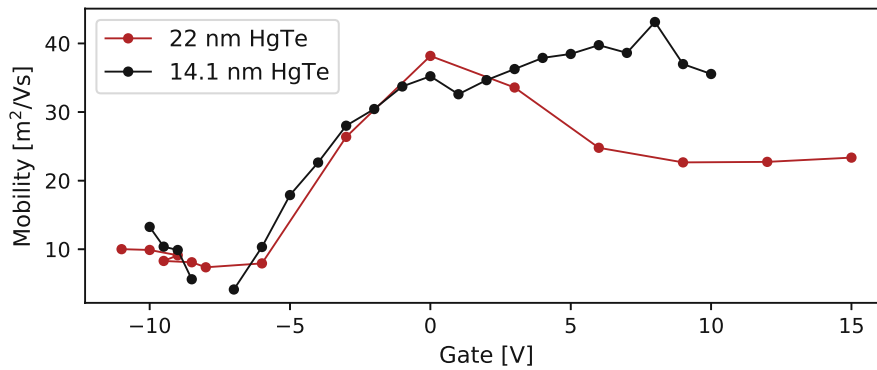


Figure 7.13: Mobility of carriers e_1 for both samples.

Additional information about the carriers in the sample was obtained by capacitance measurements (see Fig. 5.2), which displayed strong SdH oscillations as plotted against the reciprocal magnetic field in Fig. 7.14.

As seen in Fig. 7.14(a,c), the spectra of the 22-nm sample revealed that when the gate voltage value is between -10 and -6 V, two modes are present; a high-frequency mode Λ_1 with $\nu_{SdH} \sim 7.5$ T and a low-frequency mode Λ_2 with $\nu_{SdH} \sim 1$ T. With increasing gate the amplitude and frequency of the latter mode start to drastically increase (note the $10\times$ scaling in Fig. 7.14(a)), fully overshadowing mode Λ_1 above $U_g > -6$ V. At $U_g > 6$ V we observe an appearance of another low-frequency mode Λ_3 , which is well evident in data at $U_g = 12$ V in Fig. 7.14(a).

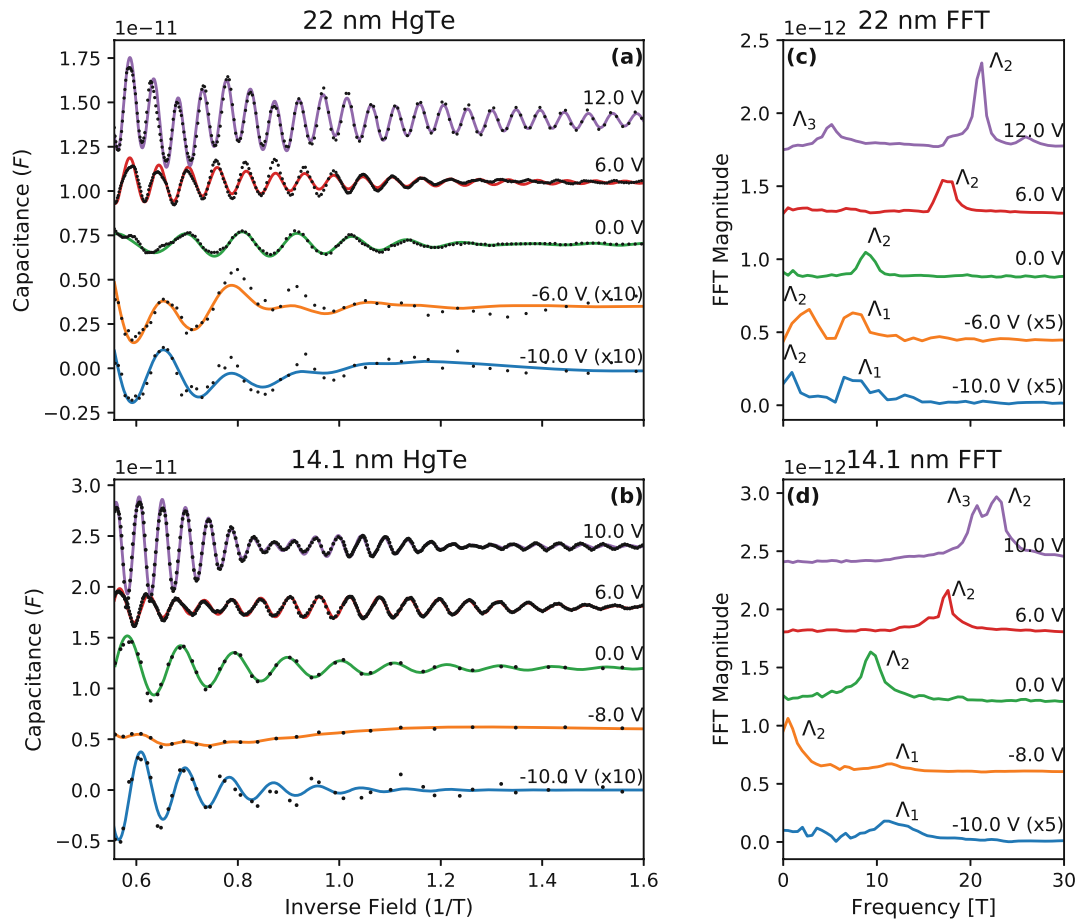


Figure 7.14: SdH oscillations of the capacitance. The SdH oscillations for the 22-nm (a) and 14.1-nm sample (b) detected at various values of the applied gate voltage. The absolute scales refer to the lowest curves, others are shifted for clarity. The experimental data (black data points) were fitted by a multi-carrier Lifshits-Kosevich model Section 3.3 (colored curves). Note vertical scaling of $\times 10$ of data at lower gate voltages. (c) and (d) show the magnitude of the fast Fourier transformation (FFT) of the data from (a) and (b), respectively. The labels correspond to modes obtained with the Lifshits-Kosevich analysis.

Similar behavior is observed for the 14.1-nm sample, Fig. 7.14(b), however, with a few key differences; (i) the low-frequency mode Λ_2 was detected only above -8 V and (ii) the frequency of the mode Λ_3 , detected at higher gate voltages, was only slightly lower than the frequency of mode Λ_2 , resulting in a "beating" phenomenon as seen at $U_g = 10$ V in Fig. 7.14(b).

Fig. 7.14(a,b) also show that the Lifshits-Kosevich model with multiple carriers (Eq. (3.47)) can be applied to the experimental data. As described in Section 3.3, it

allows us to obtain the charge density of the carriers responsible for the oscillatory behavior. As seen in Fig. 7.11(b,d) and Fig. 7.12(b,d), if we acknowledge theoretically acquired D , we find a nice overlap of densities obtained from two different techniques, magneto-optic spectroscopy and SdH analysis. For the 22-nm sample, Λ_1 corresponds to the hole carrier \mathbf{h}_1 with $D = 2$, while the carrier densities from Λ_2 and Λ_3 modes overlap perfectly with carriers \mathbf{e}_1 with $D = 2$ and \mathbf{e}_2 with $D = 1$. Similarly, the Λ_1 mode of the 14.1-nm sample corresponds to \mathbf{h}_1 and Λ_2 to \mathbf{e}_1 . Moreover, mode Λ_3 indicated spin-splitting of the interface state, which was not detected by the mass-sensitive cyclotron resonance analysis. In this case, it is suitable to sum the densities corresponding to Λ_2 and Λ_3 and compare it to n of \mathbf{e}_1 . Due to the relatively small difference between Λ_2 and Λ_3 , the outcome is the same. We would like to acknowledge that the SdH analysis of the Λ_1 modes provided carrier densities of \mathbf{h}_1 that decrease with the increasing gate voltage much slower than expected (with the slope of about $0.015 \cdot 10^{15} \text{ m}^{-2}/\text{V}$). As suspected above, this is due to the decreased $\partial E_F/\partial U_g$. The capacitance study did not show any splitting of the \mathbf{e}_1 -state in the case of the 22-nm sample. Although the exact reasons are unknown, the following artifacts could be considered: a) sample quality, b) temperature not optimal for the study of quantum effects, and c) mode Λ_3 hindering the transparency of data.

To compare theory and experiment without using isotropic approximation, the cyclotron mass can be plotted directly as a function of the 2D density. This presentation is given in Fig. 7.15, where the $\mathbf{k} \cdot \mathbf{p}$ predictions are shown with empty symbols and the experimental results with full symbols. This representation of data has an additional advantage. Since the measurements took place in different cooling cycles, we cannot rely on the gate voltage representing a good absolute metric of the electronic state of the samples. Moreover, we observed that applying high gate voltages (above 10 V) to the sample lead to the saturation of the total charge density and resulted in a shift of gate value at which the charge neutrality point was observed, i.e., the previous correspondence between the applied gate voltage and the electronic state of the sample becomes obsolete.

The theoretical points were obtained for a discrete number of n_{tot} as discussed in Section 7.2.1. The scattering in the theoretical data comes from the numerical integration of the area A in Eq. (7.1) with a discrete number of \mathbf{k} -points.

Fig. 7.15(a,b) shows experimental and theoretical data corresponding to the electron-like carriers in both samples. The comparison between the experimental points with theory allows us to recognize \mathbf{e}_1 -carrier as the fingerprint of the first conduction H1 band. The $\mathbf{k} \cdot \mathbf{p}$ theory predicted two spin-split states H1_1 and H1_2 , which should not be interpreted in terms of spin up and spin down, but as chiral spin-splitting [156]. For both samples, the splitting becomes stronger at lower densities. There, the mass of H1_1 shows signs of divergence, while the mass corresponding to the H1_2 subband stays at lower values and, in the case of the 14.1-nm sample, it even drastically decreases. This behavior, which was observed previously [156], is linked with the Rashba splitting at

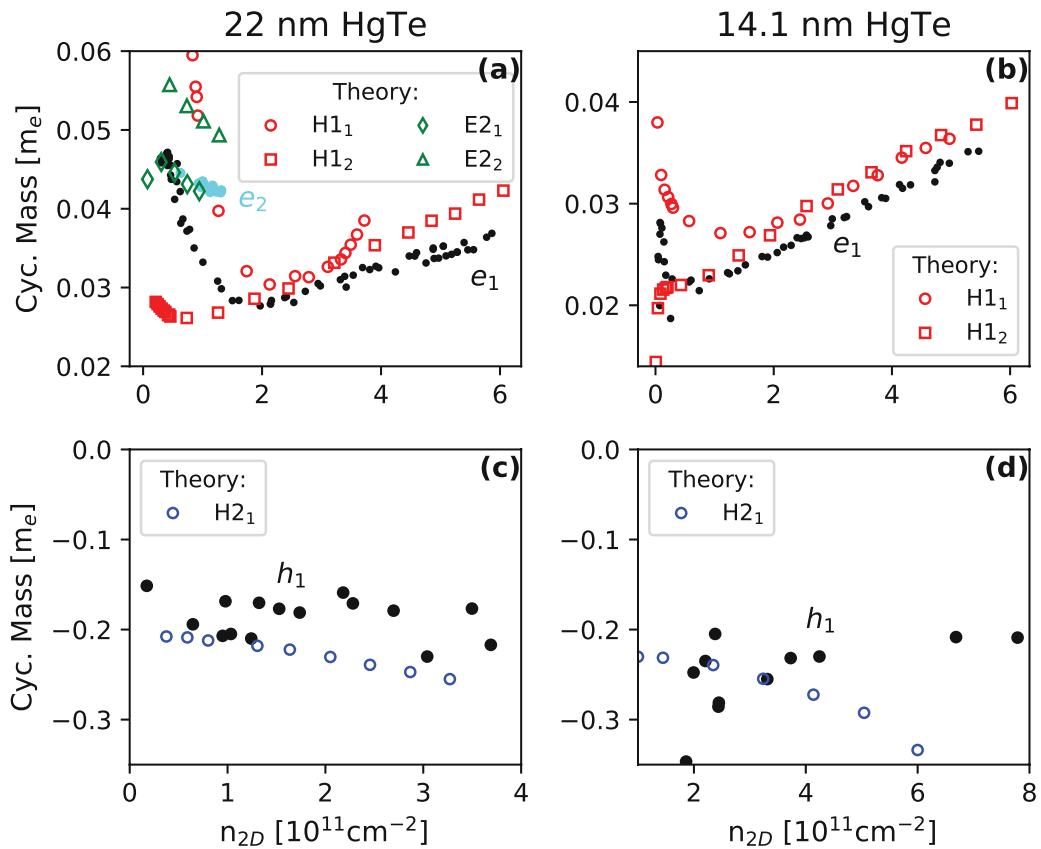


Figure 7.15: Comparison of the experimentally acquired data with the $k \cdot p$ model calculations. Compared to Fig. 7.11 and Fig. 7.12, the cyclotron masses are plotted as a function of density. (a) electron-like carriers and (c) hole-like carriers corresponding to the 22-nm sample. (b) electron-like carriers and (d) hole-like carriers detected in the 14.1-nm sample. Full symbols - experimental values, empty symbols - theory.

small k -values (see, for example, Fig. 7.16 for the case of the 14.1-nm sample). Since the precision of the cyclotron resonance experiments did not allow to observe the two spin-split H1 states separately, the values of density n , in case of the carrier e_1 , were divided by 2. The latter is also supported by the fact that at low concentrations, e_1 data seems to match with the mean value of $H1_1$ and $H1_2$. It should be noted here that the theoretical spin-splitting of the H1 subband at higher densities agrees with the conclusion of the SdH analysis of the 14.1-nm sample above. In the case of the 22-nm sample, the plotted data strongly suggests that the carrier e_2 , which was observed at high gate voltages, is linked with the second spin-polarized conduction band $E2_1$. As shown in Fig. 7.15(c,d), the h_1 -carriers correspond to the first valence bands ($H2_1$) in the systems, i.e., the spin-polarized hole band with the C_2 -symmetrical island pockets in the (k_x, k_y) -plane of the band structure. Similar to previous results [63], the theoretical

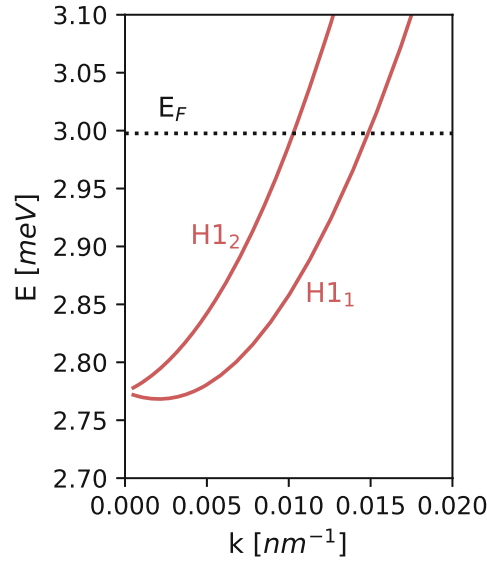


Figure 7.16: A magnified look at the $\mathbf{k} \cdot \mathbf{p}$ predictions of the band structure for the 14.1-nm sample. Rashba splitting results in a minimum of $H1_1$ at small non-zero k -value. Since the slope of $H1_1$ changes sign at a finite k -value, a divergence of mass is expected. Data corresponds to the total density of $n_{tot} = -5 \cdot 10^{11} \text{ m}^{-2}$ with the Fermi level as indicated.

hole mass slightly decreases with the carrier concentration. This trend is supported by the scattering of the experimental points for the 22-nm sample, however, data of the thinner sample do not provide the accuracy for such a conclusion. The reasons behind the experimental errors for holes were already discussed above.

To access the experimental band structure of the HgTe film, we employ the procedure presented at the beginning of this chapter, specifically Eqs. (7.1) to (7.3). According to the identification of the carriers above, we assume spin degeneracy ($D = 2$) for e_1 for both samples and double valley degeneracy ($D = 2$) for the h_1 with the two local maxima of the valence band expected at $k_0 \approx (\pm 0.17, \pm 0.17) \text{ nm}^{-1}$. The maximum of the experimental valence band has been shifted by this value. As pointed out in Section 7.2.1, for hole-like carriers we calculate the k -vector along the (1,1) direction as $k = k_0 \pm k_{eff}$ with $k_{eff} = \sqrt{2\pi n}$. In the case of the 22-nm sample, the carrier e_2 was assumed to be spin-polarized with $D = 1$. The band dispersions, calculated within the approximation above, are shown in Fig. 7.17 as solid black symbols. Direct integration lacks in providing the absolute energy position of the bands. Since we assume that the gate voltage defines a constant Fermi level in the film, the bands are vertically aligned to each other by referring to the gate voltage at which they were mutually detected.

As the Fermi energy lies in the vicinity of zero, the active states are expected to be from the spin-split $H1$ subband and the valence band holes from the $H2_1$ subband. As seen for both samples, this was also experimentally observed. In our study, the detected

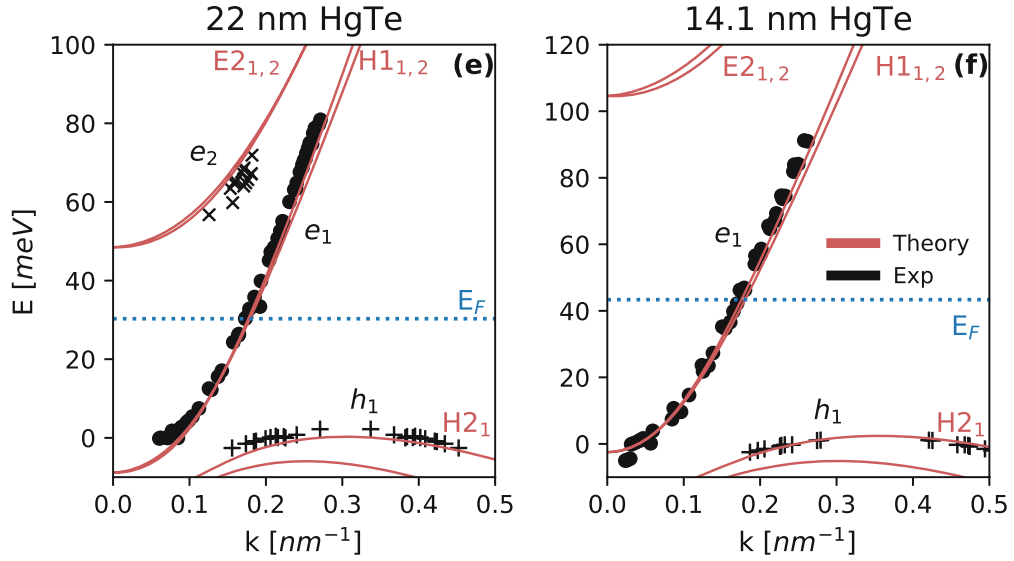


Figure 7.17: Comparison of the experimentally acquired band structures with the $\mathbf{k} \cdot \mathbf{p}$ model calculations. Band structures of both samples along (1,1) direction corresponding to $n_{tot} = 5 \cdot 10^{11} \text{ cm}^{-2}$. Symbols - experimental data obtained from cyclotron mass, solid lines are predictions of the $\mathbf{k} \cdot \mathbf{p}$ model.

carriers e_1 belong to the first conduction band and the h_1 -carriers mark the first valence band, in correlation to the conclusions of mass-density analysis above. Concerning only the 22-nm sample, the e_2 -carrier was observed at energies in correlation to the theoretical prediction of the $E2_1$ band. The reader should note that the theoretical band structures in Fig. 7.17 are calculated at $n_{tot} = 5 \cdot 10^{11} \text{ cm}^{-2}$, corresponding to the Fermi energy of $\sim 30 \text{ meV}$. A much higher charge density is required to move the Fermi energy into the $E2$ subbands. In these conditions, the $E2$ subbands are subject to a stronger splitting due to the asymmetrical structure, similar to the situation in Section 7.1. The detection of a single spin-polarized $E2$ subband is therefore reasonable.

Our study shows that the cyclotron resonance experiments can be efficiently used to directly obtain the band structures of semi-metallic HgTe films. We have experimentally observed the first valence subband, first conduction subband, and also the second conduction subband. The results produce a great overlap with the corresponding $\mathbf{k} \cdot \mathbf{p}$ theory. Furthermore, our work shows that the semi-metallic character of the HgTe samples is experimentally supported by an approximately $\sim 10 \text{ meV}$ overlap between the first conduction and first valence subbands in both samples.

7.2.3 Summary

We described the study of the cyclotron resonances in two HgTe samples with thicknesses of 14.1 and 22 nm in the sub-THz frequency range. The quasi-classical approach is utilized to recover the parameters of the charge carriers, which is approved by the linearity of the cyclotron frequency in external magnetic fields. With the help of $\mathbf{k} \cdot \mathbf{p}$ models of the electronic configurations of both samples, we were able to recognize several cyclotron resonance modes as fingerprints of the first valence band, first conduction band, and in the case of the 22 nm sample also the second conduction band. The outcome of the cyclotron resonance analysis was also strongly supported by the SdH analysis of the field-dependent capacitance measurements. Experimentally obtained band structure showed an overlap of 10 meV between the first conduction and first valence band, in turn confirming the existence of the semi-metallic state in both samples. Furthermore, the comparison between cyclotron resonance and SdH analysis confirmed the anomalous two-fold valley degeneracy of the first hole-like valence band.

8. Conclusion

In this thesis, a sub-terahertz spectroscopic study of HgTe/CdHgTe quantum wells is presented. At low temperatures, the samples were inserted into an optical cryostat and investigated using a Mach-Zehnder interferometer with an implemented controlled polarization of radiation. This experimental setup enabled measuring the amplitude and phase of the complex transmission through the investigated samples. The experimental setup was also equipped with a superconducting magnet, which provided fields up to ± 7 T parallel to the \mathbf{k} -vector of radiation (Faraday geometry). Magneto-optic experiments were conducted with either linearly- or circularly-polarized radiation, while the Fermi-level in the samples was shifted by top-gating.

A theoretical framework was established in order to extract material properties from the results of the spectroscopic study. The structure of the HgTe/CdHgTe quantum wells can be modeled by an insulating slab with an infinitely-thin metallic film on top. We have shown that by using Maxwell's theory, we can formulate a 4×4 propagation matrix that described the interaction between such structure and electromagnetic fields. This allowed us to obtain a set of formulas that describe the complex transmission through the studied sample. The resulting formulas depended on various material properties, with the most crucial being the two-dimensional conductivity of the metallic film. A quasi-classical approach that combined the Drude and Bloch theories, was utilized to obtain the conductivity of a two-dimensional crystal. Inserting the latter into the transmission formulas enabled a direct connection between the transmission spectra and the fundamental properties of the charge carriers in the system.

The model described above allowed us to analyze the cyclotron resonances that were observed in the magneto-optic transmission spectra. We were able to recover the cyclotron effective mass, two-dimensional density, and the scattering rate of positive and negative charge carriers, which belonged to various subbands in the investigated samples.

This approach allowed us to investigate the phenomenon of superradiance in a three-dimensional topological insulator. The analysis of the complex transmission coefficients showed that the radiative and transport lifetimes can be well separated in the continuous-wave spectra. When the gating shifts the Fermi level where carriers have high densities, the super-resonant radiation dominates the energy losses in the system. We have concluded that the superradiance in semiconductors can be well explained via a classical electrodynamic picture, where the coherent emission is established via the coherent interaction of the incident radiation with a thin-film sample. This superradiance study showed not to be dependent on the details of the band structure of the sample.

The cyclotron resonances in another HgTe-based three-dimensional topological insulator were investigated. In addition to the resonances from the top and bottom surface states, separate modes are observed that correspond to bulk conduction and valence bands. We have shown by the linearity of the cyclotron frequency in external magnetic fields that the quasi-classical approach is allowed to recover the charge carriers in these systems. The quasi-classical approach gives a direct relation between the carrier properties and the band structure of a two-dimensional crystal as long as the rotational symmetry of the band structure is ensured. Within this approximation, the band structure can be extracted from the gate dependence of the magneto-optical spectra. Considering the obvious effect of the asymmetric gating potential on the sample, the experimental band structure agrees reasonably well with the predictions of the $\mathbf{k} \cdot \mathbf{p}$ model. Especially for the case when the Fermi-level is shifted to the valence band, clear deviations between theory and experiment are observed. Although the quasi-classical assumption approached the limit of its validity in the case of holes, the valence band was observed to be at lower energies than predicted, which may suggest that a further improvement of the theoretical picture is required.

A similar approach to recover the band structure was applied to two semi-metallic HgTe samples with thicknesses of 14.1 and 22 nm. The comparison between $\mathbf{k} \cdot \mathbf{p}$ models of the electronic configurations of both samples and their corresponding experimental band structures enabled us to recognize several cyclotron resonance modes as fingerprints of the first valence band, first conduction band, and, in the case of the 22-nm sample, also the second conduction band. An overlap of about 10 meV between the first conduction and first valence band was experimentally observed, in turn confirming the existence of the semi-metallic states in both samples. Shubnikov-de Haas oscillations in quantum capacitance were analyzed with the help of the Lifshits-Kosevich model. The carrier concentrations, obtained from the frequency of the observed modes, strongly supported the magneto-optical data and in turn enabled to recover the degeneracy of the probed electronic states. The outcome confirmed the anomalous two-fold valley degeneracy of the first hole-like valence band. The $\mathbf{k} \cdot \mathbf{p}$ model predicted strong splitting of the first-conduction band due to the BIA and Rashba effects, which is especially obvious at lower concentrations. There, one subband showed a divergence of the effective mass, while the mass corresponding to the other subband decreased drastically. Splitting of the first conduction band was not observed in the spectroscopic approach and was only confirmed for one sample at high densities by the Shubnikov-de Haas analysis. The reasons behind this mismatch are still unclear, it should be noted, however, that low carrier concentrations hinder the accuracy of both experimental approaches.

In addition, the thesis demonstrated that versatile wave plates for terahertz-beam shaping can be very easily produced with a commercially available 3D printer. Specifically, we showed how dielectric phase plates can modulate an incoming Gaussian beam in such a way that it produces an arbitrary image on the detector plane. These results are expected to facilitate THz imaging on all levels where customized and cost-efficient beam shaping solutions are required.

9. Acknowledgments

I am very grateful to everyone who participated in making my PhD studies one of the most insightful, exciting, enjoyable, and memorable times of my life. Without the support, guidance, knowledge, and care from the following people, this work would never see the light of day. Namely, I would like to thank:

- Prof. Andrei Pimenov, thank you for your leadership, guidance and for sharing your knowledge. Thank you for motivating and challenging me through constant demand for excellence and for giving me this amazing opportunity.
- Dr. Alexey Shuvaev, thank you for your immense scientific input throughout my PhD studies and my thesis. I am in your debt for your constant readiness to help, for your insightful teachings, crucial experimental lessons, and Majorana discussions. Most of all, thank you for your friendship and dear company in the late hours at Freihaus and downstairs in the "Room of Hell". You're the BOSS!
- Dr. Elena G. Novik, thank you for all your theoretical contributions to the HgTe story. I am very thankful for all our discussions and pleasant video chats.
- Dr. Andre Vogel, for coordinating the Solids4Fun school. I am very grateful for all the countless times you helped me get out of troubling situations that I got myself into. Thank you for always having an open door for a friendly conversation.
- Prof. Ze D. Kvon and Prof. Nikolai N. Mikhailov, for the preparation of the HgTe samples. Prof. Kvon, thank you for that bag of sugar!
- Dr. Maxim Savchenko, for sharing your knowledge and passion for physics and equipping our U4 setup with the capacitance-measuring option.
- Prof. Stefan Rotter, for your helpful discussions regarding the 3D-printed waveplates.
- Dr. Lukas Weymann, thank you for your friendship, epic table-tennis rivalry, for that urban splatter art in front of my building, and that one time when you played "Happy Birthday" for me on your tuba. Thank you for insisting on proof-reading my German abstract, even though I wrote it perfectly. Lunch!
- Dr. Evan Constable, thank you for sharing your passion for science and football with me and for being a good friend. Thank you for showing us the "cool" way

of getting to the first floor of the Freihaus. Also, thank you for proof-reading my abstract on a Sunday.

- Lorenz Bergen, Janek Wettstein, Dr. David Szaller, Dr. Uladzislau Dziom, thank you guys for creating an amazing, friendly, calm, fun, and productive atmosphere in the office. I am very grateful for all our night-outs, conferences, and discussions about science, life, and lunch-options.
- Anna Pimenov, thank you for your help during my studies, for coordinating our group, organizing events, and bringing an artistic value to our boring scientific lives.
- Healthcare workers of the world, for risking their lives for our benefit during the pandemic.
- Bine Travnik, for the relaxing evenings, pleasant meals, and, most of all, for helping me to sleep deeper and better.
- HDL and its members DingDong_Daddy, DonFriedow and Zutor7, for always being RFD and for picking me up every time i was down(ed).
- Billa-Boiz, for all the pleasant elevator rides and quick chats while waiting in the queue.
- HG2, thank you for that amazing Valentine's day and your platinum gift.
- All the guys from the Bro Group, thank you for your friendship, idiotic conversations, memes, and amazing hang-outs. Jak się masz!
- Anči, for being so friendly and having unconditional patience for my delayed responses. Good luck with your Bar Exam!
- Liza, for your friendship through all the years. Thank you for your kindness, support and for always being there when I needed a sympathetic ear.
- The Primi Šport direktor Rimč a.k.a. The Backflip King, thank you brate for putting up with me for more than 15 years, for always being there for help, support, and entertainment. Thank you for all your pleasant visits to Vienna! Thank you for showing me, you can NOT do it on a carpet or grass.
- My eternal flatmate Zupi, Vienna would not be my home without you. For that, I am forever in your debt. I could not wish for a better roomie, life-companion, and comrade in battle. Hvala, što si mi dozvolio, da diram tvoj dlačnik, naučio šta je adakter i gdje idu ove male alkaline. Kralju!
- Babi Vera, hvala ti za vse srčne misli in podporo iz Zagorja, najlepšega mesta na svetu.

Chapter 9. Acknowledgments

- Stara mama in ata Emil, hvala vama za vso podporo, pozdrave in pošiljke dobrot, ki so mi omogočili, da sem lahko veliko časa preživel na svežem zraku.
- My father Jurij, for your love, care, and for always keeping an eye on me.
- My mother Tatjana and sister Pika, thank you for all the love, support, and care that passed across each and every border between us. I owe everything to you two. Thank you for always being there for me. Mum, thank you for always keeping an open door to a warm home in Ljubljana. Thank you for all the carpets, jackets, fans, house-cleaning advice, ..., that I bitterly accepted, only to later learn how useful they were. Pika, thank you for always being my big sister and the best role model. Thank you for always taking care to keep us in touch and for your constant hunger for adventure. I love you both.

Bibliography

- [1] M. Kritikos. *Ten technologies to fight coronavirus*. EPRS| European Parliamentary Research Service.: European Parliament (2020)
- [2] H. Rosling. *Factfulness*. Flammarion (2019)
- [3] A. Damascelli, Z. Hussain, Z. X. Shen. *Angle-resolved photoemission studies of the cuprate superconductors*. *Rev. Mod. Phys.* **75**, 2, pp. 473–541 (2003), URL <https://link.aps.org/doi/10.1103/RevModPhys.75.473>
- [4] R. B. Laughlin. *Quantized Hall conductivity in two dimensions*. *Phys. Rev. B* **23**, pp. 5632–5633 (1981), URL <https://link.aps.org/doi/10.1103/PhysRevB.23.5632>
- [5] D. J. Thouless, M. Kohmoto, M. P. Nightingale, M. den Nijs. *Quantized Hall Conductance in a Two-Dimensional Periodic Potential*. *Phys. Rev. Lett.* **49**, pp. 405–408 (1982), URL <https://link.aps.org/doi/10.1103/PhysRevLett.49.405>
- [6] K. v. Klitzing, G. Dorda, M. Pepper. *New Method for High-Accuracy Determination of the Fine-Structure Constant Based on Quantized Hall Resistance*. *Physical Review Letters* **45**, 6, pp. 494–497 (1980)
- [7] C. L. Kane, E. J. Mele. *Quantum Spin Hall Effect in Graphene*. *Phys. Rev. Lett.* **95**, p. 226801 (2005), URL <https://link.aps.org/doi/10.1103/PhysRevLett.95.226801>
- [8] M. König, S. Wiedmann, C. Brüne, A. Roth, H. Buhmann, L. W. Molenkamp, X.-L. Qi, S.-C. Zhang. *Quantum Spin Hall Insulator State in HgTe Quantum Wells*. *Science* **318**, 5851, pp. 766–770 (2007), URL <http://www.sciencemag.org/content/318/5851/766.abstract>
- [9] Z. D. Kvon, E. B. Olshanetsky, D. A. Kozlov, N. N. Mikhailov, S. A. Dvoretiskii. *Two-dimensional electron-hole system in a HgTe-based quantum well*. *JETP Letters* **87**, 9, pp. 502–505 (2008)
- [10] B. A. Bernevig, T. L. Hughes, S.-C. Zhang. *Quantum Spin Hall Effect and Topological Phase Transition in HgTe Quantum Wells*. *Science* **314**, 5806, pp. 1757–1761 (2006), URL <http://www.sciencemag.org/content/314/5806/1757.abstract>

- [11] B. Büttner, C. X. Liu, G. Tkachov, E. G. Novik, C. Brüne, H. Buhmann, E. M. Hankiewicz, P. Recher, B. Trauzettel, S. C. Zhang, L. W. Molenkamp. *Single valley Dirac fermions in zero-gap HgTe quantum wells*. Nat. Phys. **7**, 5, pp. 418–422 (2011)
- [12] L. Fu, C. L. Kane. *Topological insulators with inversion symmetry*. Phys. Rev. B **76**, p. 045302 (2007), URL <https://link.aps.org/doi/10.1103/PhysRevB.76.045302>
- [13] M. Born, E. Wolf. *Principles of optics: electromagnetic theory of propagation, interference and diffraction of light*. Elsevier (2013)
- [14] N. W. Ashcroft, N. D. Mermin. *Solid State Physics*. HRW international editions, Holt, Rinehart and Winston (1976)
- [15] A. Sommerfeld. *Zur Elektronentheorie der Metalle auf Grund der Fermischen Statistik*. Zeitschrift für Physik **47**, 1-2, pp. 1–32 (1928)
- [16] A. A. Volkov, Y. G. Goncharov, G. V. Kozlov, S. P. Lebedev, A. M. Prokhorov. *Dielectric measurements in the submillimeter wavelength region*. Infrared Phys. **25**, 1-2, p. 369 (1985), URL <http://www.sciencedirect.com/science/article/B6X3W-46K4CH2-29/2/43ef2c1b497859011f2f67a144d4bb72>
- [17] A. Shuvaev. *Spectroscopic study of manganites with magnetoelectric coupling*. Ph.D. thesis, University of Würzburg, Würzburg. [Http://opus.bibliothek.uni-wuerzburg.de/volltexte/2013/7871/](http://opus.bibliothek.uni-wuerzburg.de/volltexte/2013/7871/) (2012)
- [18] A. M. Shuvaev, G. V. Astakhov, C. Brüne, H. Buhmann, L. W. Molenkamp, A. Pimenov. *Terahertz magneto-optical spectroscopy in HgTe thin films*. Semicond. Sci. Technol. **27**, 12, p. 124004 (2012), URL <http://stacks.iop.org/0268-1242/27/i=12/a=124004>
- [19] A. Shuvaev, A. Pimenov, G. V. Astakhov, M. Muhlbauer, C. Brune, H. Buhmann, L. W. Molenkamp. *Room temperature electrically tunable terahertz Faraday effect*. Appl. Phys. Lett. **102**, 24, 241902 (2013), URL <http://link.aip.org/link/?APL/102/241902/1>
- [20] M. Wichmann, A. S. Mondol, N. Kocic, S. Lippert, T. Probst, M. Schwerdtfeger, S. Schumann, T. Hochrein, P. Heidemeyer, M. Bastian, G. Bastian, M. Koch. *Terahertz plastic compound lenses*. Applied Optics **52**, 18, p. 4186 (2013)
- [21] B. Scherger, M. Scheller, C. Jansen, M. Koch, K. Wiesauer. *Terahertz lenses made by compression molding of micropowders*. Applied Optics **50**, 15, p. 2256 (2011)

Bibliography

- [22] S. F. Busch, M. Weidenbach, M. Fey, F. Schäfer, T. Probst, M. Koch. *Optical Properties of 3D Printable Plastics in the THz Regime and their Application for 3D Printed THz Optics*. J. Infr. Millim. Waves **35**, 12, pp. 993–997. ISSN 18666906 (2014)
- [23] G. Grüner, C. Dahl. *Millimeter and submillimeter wave spectroscopy of solids*, volume 200. Springer (1998)
- [24] L. Weymann. *Novel Static and Dynamic Phenomena in Magnetolectric Materials*. Ph.D. thesis, TU Wien (2020)
- [25] J. Kong. *Electromagnetic Wave Theory*. A Wiley-Interscience publication, Wiley. ISBN 9780471828235 (1986), URL <https://books.google.at/books?id=OposAAAAYAAJ>
- [26] Y. Xing, M. Kaaniche, B. Pesquet-Popescu, F. Dufaux. *Digital Holographic Data Representation and Compression*. Elsevier Science. ISBN 9780128028902 (2015)
- [27] D. Leseberg. *Computer-generated three-dimensional image holograms*. Appl. Opt. **31**, 2, pp. 223–229 (1992), URL <http://ao.osa.org/abstract.cfm?URI=ao-31-2-223>
- [28] K. Matsushima. *Computer-generated holograms for three-dimensional surface objects with shade and texture*. Appl. Opt. **44**, 22, pp. 4607–4614 (2005), URL <http://ao.osa.org/abstract.cfm?URI=ao-44-22-4607>
- [29] M. Makowski, M. Sypek, A. Kolodziejczyk, G. Mikula. *Three-plane phase-only computer hologram generated with iterative Fresnel algorithm*. Optical Engineering **44**, 12, p. 125805 (2005)
- [30] M. Makowski, M. Sypek, A. Kolodziejczyk, G. Mikula, J. Suszek. *Iterative design of multiplane holograms: experiments and applications*. Optical Engineering **46**, 4, p. 045802 (2007)
- [31] B. Walther, C. Helgert, C. Rockstuhl, F. Setzpfandt, F. Eilenberger, E.-B. Kley, F. Lederer, A. Tünnermann, T. Pertsch. *Spatial and Spectral Light Shaping with Metamaterials*. Adv. Mater. **24**, 47, pp. 6300–6304. ISSN 1521-4095 (2012), URL <http://dx.doi.org/10.1002/adma.201202540>
- [32] J. Sun, E. Timurdogan, A. Yaacobi, E. S. Hosseini, M. R. Watts. *Large-scale nanophotonic phased array*. Nature **493**, 7431, pp. 195–199. ISSN 0028-0836 (2013)
- [33] N. Yu, F. Capasso. *Flat optics with designer metasurfaces*. Nat. Mater. **13**, 2, pp. 139–150. ISSN 1476-1122 (2014)

- [34] P. Genevet, F. Capasso. *Holographic optical metasurfaces: a review of current progress*. Rep. Prog. Phys. **78**, 2. ISSN 0034-4885 (2015)
- [35] J. Upatnieks, C. Leonard. *Efficiency and Image Contrast of Dielectric Holograms*. J. Opt. Soc. Am. **60**, 3, pp. 297–305 (1970), URL <http://www.osapublishing.org/abstract.cfm?URI=josa-60-3-297>
- [36] M. T. Gale, M. Rossi, H. Schütz, P. Ehbets, H. P. Herzig, D. Prongué. *Continuous-relief diffractive optical elements for two-dimensional array generation*. Appl. Opt. **32**, 14, pp. 2526–2533 (1993), URL <http://ao.osa.org/abstract.cfm?URI=ao-32-14-2526>
- [37] D. Lin, P. Fan, E. Hasman, M. L. Brongersma. *Dielectric gradient metasurface optical elements*. Science **345**, 6194, pp. 298–302 (2014)
- [38] Z. Zeng, H. Zheng, Y. Yu, A. K. Asundi. *Off-axis phase-only holograms of 3D objects using accelerated point-based Fresnel diffraction algorithm*. Opt. Lasers Eng. **93**, Suppl. C, pp. 47 – 54. ISSN 0143-8166 (2017), URL <http://www.sciencedirect.com/science/article/pii/S0143816616302445>
- [39] S. Rotter, S. Gigan. *Light fields in complex media: Mesoscopic scattering meets wave control*. Rev. Mod. Phys. **89**, p. 015005 (2017), URL <https://link.aps.org/doi/10.1103/RevModPhys.89.015005>
- [40] A. D. Squires, E. Constable, R. A. Lewis. *3D Printed Terahertz Diffraction Gratings And Lenses*. J. Infrared Millim. Terahertz Waves **36**, 1, pp. 72–80. ISSN 1866-6906 (2015), URL <https://doi.org/10.1007/s10762-014-0122-8>
- [41] J. Suszek, A. Siemion, M. S. Bieda, N. Błocki, D. Coquillat, G. Cywiński, E. Czerwińska, M. Doch, A. Kowalczyk, N. Palka, et al. *3-D-printed flat optics for THz linear scanners*. IEEE transactions on Terahertz Science and Technology **5**, 2, pp. 314–316 (2015)
- [42] A. Hernandez-Serrano, M. Weidenbach, S. Busch, M. Koch, E. Castro-Camus. *Fabrication of gradient-refractive-index lenses for terahertz applications by three-dimensional printing*. JOSA B **33**, 5, pp. 928–931 (2016)
- [43] W. D. Furlan, V. Ferrando, J. A. Monsoriu, P. Zagrajek, E. Czerwińska, M. Szustakowski. *3D printed diffractive terahertz lenses*. Optics letters **41**, 8, pp. 1748–1751 (2016)
- [44] W. J. Otter, S. Lucyszyn. *Hybrid 3-D-printing technology for tunable THz applications*. Proceedings of the IEEE **105**, 4, pp. 756–767 (2017)

- [45] A. Hernandez-Serrano, E. Castro-Camus. *Quasi-Wollaston-prism for terahertz frequencies fabricated by 3D printing*. *Journal of Infrared, Millimeter, and Terahertz Waves* **38**, 5, pp. 567–573 (2017)
- [46] H. Xin, M. Liang. *3-D-printed microwave and THz devices using polymer jetting techniques*. *Proceedings of the IEEE* **105**, 4, pp. 737–755 (2017)
- [47] F. Machado, P. Zagrajek, J. A. Monsoriu, W. D. Furlan. *Terahertz Sieves*. *IEEE Transactions on Terahertz Science and Technology* **8**, 1, pp. 140–143 (2018)
- [48] R. W. Gerchberg, W. O. Saxton. *A practical algorithm for the determination of phase from image and diffraction plane pictures*. *Optik* **35**, 2, pp. 237–246. ISSN 10500529 (1972), URL <http://ci.nii.ac.jp/naid/10010556614/>
- [49] M. Born, E. Wolf, A. B. Bhatia, P. C. Clemmow, D. Gabor, A. R. Stokes, A. M. Taylor, P. A. Wayman, W. L. Wilcock. *Principles of Optics: Electromagnetic Theory of Propagation, Interference and Diffraction of Light*. Cambridge University Press, 7 edition (1999)
- [50] P. Drude. *Zur elektronentheorie der metalle*. *Annalen der physik* **306**, 3, pp. 566–613 (1900)
- [51] E. H. Hall. *On a New Action of the Magnet on Electric Currents*. *American Journal of Mathematics* **2**, 3, p. 287 (1879)
- [52] J. R. Chelikowsky, M. L. Cohen. *Electronic structure of silicon*. *Physical Review B* **10**, 12, pp. 5095–5107 (1974)
- [53] W. Commons. *A diagram of the first Brillouin zone of a face-centred cubic (FCC) lattice, with points of high symmetry marked*. File: Brillouin Zone (1st, FCC).svg (2008), URL [https://commons.wikimedia.org/wiki/File:Brillouin_Zone_\(1st,_FCC\).svg](https://commons.wikimedia.org/wiki/File:Brillouin_Zone_(1st,_FCC).svg)
- [54] W. Commons. *Schematics of calculated band structure of crystalline Si*. File: Band structure Si schematic.svg (2008), URL https://commons.wikimedia.org/wiki/File:Band_structure_Si_schematic.svg
- [55] V. Dziom, A. Shuvaev, N. N. Mikhailov, A. Pimenov. *Terahertz properties of Dirac fermions in HgTe films with optical doping*. *2D Mater.* **4**, 2, p. 024005 (2017), URL <http://stacks.iop.org/2053-1583/4/i=2/a=024005>

- [56] A. A. Abrikosov. *Fundamentals of the Theory of Metals*. Courier Dover Publications (2017)
- [57] U. Dziom. *THz spectroscopy of novel spin and quantum Hall systems*. Ph.D. thesis, TU Wien (2018)
- [58] L. Onsager. *Interpretation of the de Haas-van Alphen effect*. The London, Edinburgh, and Dublin Philosophical Magazine and Journal of Science **43**, 344, pp. 1006–1008 (1952)
- [59] L. Schubnikow, W. J. de Haas. *Magnetische Widerstandsvergrosserung in Einkristallen von Wismut bei tiefen Temperaturen*. Leiden Commun **207**, p. 3 (1930)
- [60] B. Skinner, B. I. Shklovskii. *Giant capacitance of a plane capacitor with a two-dimensional electron gas in a magnetic field*. Phys. Rev. B **87**, p. 035409 (2013), URL <https://link.aps.org/doi/10.1103/PhysRevB.87.035409>
- [61] A. S. Shigeji Fujita. *Theory of Shubnikov-de Haas and Quantum Hall Oscillations in Graphene under Bias and Gate Voltages*. Global Journal of Science Frontier Research ISSN 2249-4626 (2014), URL <https://journalofscience.org/index.php/GJSFR/article/view/1313>
- [62] E. Lifshits, A. Kosevich. *Theory of the Shubnikov—de Haas effect*. Journal of Physics and Chemistry of Solids **4**, 1-2, pp. 1–10 (1958)
- [63] G. M. Minkov, V. Y. Aleshkin, O. E. Rut, A. A. Sherstobitov, A. V. Germanenko, S. A. Dvoretzki, N. N. Mikhailov. *Valence band energy spectrum of HgTe quantum wells with an inverted band structure*. Phys. Rev. B **96**, 3, p. 035310 (2017)
- [64] A. A. Dobretsova, Z. D. Kvon, S. S. Krishtopenko, N. N. Mikhailov, S. A. Dvoretzky. *Spin splitting of surface states in HgTe quantum wells*. Low Temp. Phys. **45**, 2, pp. 159–164 (2019)
- [65] A. Gold. *Transport time and single-particle relaxation time in two-dimensional semiconductors*. In *Physical Concepts of Materials for Novel Optoelectronic Device Applications II: Device Physics and Applications*, volume 1362, pp. 309–313. International Society for Optics and Photonics (1991)
- [66] E. H. Hwang, S. D. Sarma. *Single-particle relaxation time versus transport scattering time in a two-dimensional graphene layer*. Physical Review B **77**, 19 (2008)

- [67] W. Lawson, S. Nielsen, E. Putley, A. Young. *Preparation and properties of HgTe and mixed crystals of HgTe-CdTe*. Journal of Physics and Chemistry of Solids **9**, 3-4, pp. 325–329 (1959)
- [68] P. Norton. *HgCdTe infrared detectors*. Optoelectronics review , 3, pp. 159–174 (2002)
- [69] A. M. Shuvaev, G. V. Astakhov, A. Pimenov, C. Brüne, H. Buhmann, L. W. Molenkamp. *Giant Magneto-Optical Faraday Effect in HgTe Thin Films in the Terahertz Spectral Range*. Phys. Rev. Lett. **106**, p. 107404 (2011), URL <http://link.aps.org/doi/10.1103/PhysRevLett.106.107404>
- [70] M. Z. Hasan, C. L. Kane. *Colloquium : Topological insulators*. Rev. Mod. Phys. **82**, pp. 3045–3067 (2010), URL <http://link.aps.org/doi/10.1103/RevModPhys.82.3045>
- [71] X.-L. Qi, T. L. Hughes, S.-C. Zhang. *Topological field theory of time-reversal invariant insulators*. Phys. Rev. B **78**, p. 195424 (2008), URL <http://link.aps.org/doi/10.1103/PhysRevB.78.195424>
- [72] M. Z. Hasan, C. L. Kane. *Colloquium: topological insulators*. Reviews of modern physics **82**, 4, p. 3045 (2010)
- [73] X.-L. Qi, S.-C. Zhang. *Topological insulators and superconductors*. Rev. Mod. Phys. **83**, pp. 1057–1110 (2011), URL <https://link.aps.org/doi/10.1103/RevModPhys.83.1057>
- [74] Y. Ando. *Topological insulator materials*. Journal of the Physical Society of Japan **82**, 10, p. 102001 (2013)
- [75] J. K. Asbóth, L. Oroszlány, A. Pályi. *A short course on topological insulators*. Lecture notes in physics **919**, pp. 997–1000 (2016)
- [76] N. N. Berchenko, M. V. Pashkovskii. *Mercury telluride—a zero-gap semiconductor*. Soviet Physics Uspekhi **19**, 6, pp. 462–480 (1976)
- [77] J. Chu, A. Sher. *Physics and Properties of Narrow Gap Semiconductors*. Springer New York. ISBN 9780387748016 (2007), URL <https://books.google.com.ec/books?id=J6PWAvldNfcC>
- [78] C. Brüne. *HgTe based topological insulators*. Ph.d. thesis, Universität Würzburg (2014)
- [79] C. Brüne, C. X. Liu, E. G. Novik, E. M. Hankiewicz, H. Buhmann, Y. L. Chen, X. L. Qi, Z. X. Shen, S. C. Zhang, L. W. Molenkamp. *Quantum Hall Effect from the Topological Surface States of Strained Bulk HgTe*. Phys. Rev. Lett. **106**, p.

- 126803 (2011), URL <http://link.aps.org/doi/10.1103/PhysRevLett.106.126803>
- [80] A. M. Shuvaev, V. Dziom, N. N. Mikhailov, Z. D. Kvon, Y. Shao, D. N. Basov, A. Pimenov. *Band structure of a two-dimensional Dirac semimetal from cyclotron resonance*. Phys. Rev. B **96**, p. 155434 (2017), URL <https://link.aps.org/doi/10.1103/PhysRevB.96.155434>
- [81] A. H. Castro Neto, F. Guinea, N. M. R. Peres, K. S. Novoselov, A. K. Geim. *The electronic properties of graphene*. Rev. Mod. Phys. **81**, pp. 109–162 (2009), URL <http://link.aps.org/doi/10.1103/RevModPhys.81.109>
- [82] Z. D. Kvon, E. B. Olshanetsky, N. N. Mikhailov, D. A. Kozlov. *Two-dimensional electron systems in HgTe quantum wells*. Low Temp. Phys. **35**, 1, pp. 6–14 (2009), URL <http://dx.doi.org/10.1063/1.3064862>
- [83] K.-M. Dantscher, D. A. Kozlov, P. Olbrich, C. Zoth, P. Faltermeier, M. Lindner, G. V. Budkin, S. A. Tarasenko, V. V. Bel'kov, Z. D. Kvon, N. N. Mikhailov, S. A. Dvoretzky, D. Weiss, B. Jenichen, S. D. Ganichev. *Cyclotron-resonance-assisted photocurrents in surface states of a three-dimensional topological insulator based on a strained high-mobility HgTe film*. Phys. Rev. B **92**, p. 165314 (2015), URL <http://link.aps.org/doi/10.1103/PhysRevB.92.165314>
- [84] D. A. Kozlov, Z. D. Kvon, E. B. Olshanetsky, N. N. Mikhailov, S. A. Dvoretzky, D. Weiss. *Transport Properties of a 3D Topological Insulator based on a Strained High-Mobility HgTe Film*. Phys. Rev. Lett. **112**, p. 196801 (2014), URL <https://link.aps.org/doi/10.1103/PhysRevLett.112.196801>
- [85] D. A. Kozlov, D. Bauer, J. Ziegler, R. Fischer, M. L. Savchenko, Z. D. Kvon, N. N. Mikhailov, S. A. Dvoretzky, D. Weiss. *Probing Quantum Capacitance in a 3D Topological Insulator*. Phys. Rev. Lett. **116**, p. 166802 (2016), URL <http://link.aps.org/doi/10.1103/PhysRevLett.116.166802>
- [86] D. A. Kozlov, D. Bauer, J. Ziegler, R. Fischer, M. L. Savchenko, Z. D. Kvon, N. N. Mikhailov, S. A. Dvoretzky, D. Weiss. *Quantum capacitance of a three-dimensional topological insulator based on HgTe*. Low Temperature Physics **43**, 4, pp. 430–436 (2017)
- [87] V. Varavin, S. Dvoretzky, V. Liberman, N. Mikhailov, Y. G. Sidorov. *Molecular beam epitaxy of high quality Hg_{1-x}Cd_xTe films with control of the composition distribution*. Journal of crystal growth **159**, 1-4, pp. 1161–1166 (1996)
- [88] H. R. Philipp, H. Ehrenreich. *Optical Properties of Semiconductors*. Phys. Rev. **129**, pp. 1550–1560 (1963), URL <https://link.aps.org/doi/10.1103/PhysRev.129.1550>

- [89] E. D. Palik, J. K. Furdyna. *Infrared and microwave magnetoplasma effects in semiconductors*. Reports on Progress in Physics **33**, 3, pp. 1193–1322 (1970)
- [90] M. L. Cohen, J. R. Chelikowsky. *Electronic structure and optical properties of semiconductors*, volume 75. Springer Science & Business Media (2012)
- [91] J.-M. Pouchard, P. Q. Liu, T. M. Slipchenko, A. Y. Nikitin, L. Martin-Moreno, J. Faist, A. B. Kuzmenko. *Electrically controlled terahertz magneto-optical phenomena in continuous and patterned graphene*. Nature Communications **8**, 1 (2017)
- [92] I. O. Nedoliuk, S. Hu, A. K. Geim, A. B. Kuzmenko. *Colossal infrared and terahertz magneto-optical activity in a two-dimensional Dirac material*. Nature Nanotechnology **14**, 8, pp. 756–761 (2019)
- [93] R. V. Aguilar, A. V. Stier, W. Liu, L. S. Bilbro, D. K. George, N. Bansal, L. Wu, J. Cerne, A. G. Markelz, S. Oh, N. P. Armitage. *Terahertz Response and Colossal Kerr Rotation from the Surface States of the Topological Insulator Bi₂Se₃*. Physical Review Letters **108**, 8 (2012)
- [94] M. Autore, H. Engelkamp, F. D’Apuzzo, A. D. Gaspare, P. D. Pietro, I. L. Vecchio, M. Brahlek, N. Koirala, S. Oh, S. Lupi. *Observation of Magnetoplasmons in Bi₂Se₃ Topological Insulator*. ACS Photonics **2**, 9, pp. 1231–1235 (2015)
- [95] M. S. Zholudev, A. V. Ikonnikov, F. Teppe, M. Orlita, K. V. Maremyanin, K. E. Spirin, V. I. Gavrilenko, W. Knap, S. A. Dvoretzkiy, N. N. Mihailov. *Cyclotron resonance in HgTe/CdTe-based heterostructures in high magnetic fields*. Nanosci. Res. Lett. **7**, p. 534 (2012)
- [96] Z.-D. Kvon, S. N. Danilov, N. N. Mikhailov, S. A. Dvoretzkiy, W. Prettl, S. D. Ganichev. *Cyclotron resonance photoconductivity of a two-dimensional electron gas in HgTe quantum wells*. Physica E **40**, 6, pp. 1885 – 1887 (2008), URL <http://www.sciencedirect.com/science/article/pii/S1386947707003645>
- [97] V. Dziom, A. Shuvaev, A. Pimenov, G. V. Astakhov, C. Ames, K. Bendias, J. Böttcher, G. Tkachov, E. M. Hankiewicz, C. Brüne, H. Buhmann, L. W. Molenkamp. *Observation of the universal magnetoelectric effect in a 3D topological insulator*. Nat. Commun. **8**, p. 15197 (2017), URL <http://dx.doi.org/10.1038/ncomms15197>
- [98] A. Perot, C. Fabry. *On the application of interference phenomena to the solution of various problems of spectroscopy and metrology*. The Astrophysical Journal **9**, p. 87 (1899)

- [99] A. Shuvaev, V. Dziom, Z. D. Kvon, N. N. Mikhailov, A. Pimenov. *Universal Faraday Rotation in HgTe Wells with Critical Thickness*. Phys. Rev. Lett. **117**, p. 117401 (2016), URL <http://link.aps.org/doi/10.1103/PhysRevLett.117.117401>
- [100] W.-K. Tse, A. H. MacDonald. *Magneto-optical Faraday and Kerr effects in topological insulator films and in other layered quantized Hall systems*. Phys. Rev. B **84**, p. 205327 (2011), URL <http://link.aps.org/doi/10.1103/PhysRevB.84.205327>
- [101] R. Hooke, T. A. Jeeves. *"Direct Search" Solution of Numerical and Statistical Problems*. Journal of the ACM **8**, 2, pp. 212–229 (1961)
- [102] R. H. Dicke. *Coherence in Spontaneous Radiation Processes*. Phys. Rev. **93**, pp. 99–110 (1954), URL <https://link.aps.org/doi/10.1103/PhysRev.93.99>
- [103] N. E. Rehler, J. H. Eberly. *Superradiance*. Phys. Rev. A **3**, pp. 1735–1751 (1971), URL <https://link.aps.org/doi/10.1103/PhysRevA.3.1735>
- [104] N. Skribanowitz, I. P. Herman, J. C. MacGillivray, M. S. Feld. *Observation of Dicke Superradiance in Optically Pumped HF Gas*. Phys. Rev. Lett. **30**, pp. 309–312 (1973), URL <https://link.aps.org/doi/10.1103/PhysRevLett.30.309>
- [105] M. Gross, P. Goy, C. Fabre, S. Haroche, J. M. Raimond. *Maser Oscillation and Microwave Superradiance in Small Systems of Rydberg Atoms*. Phys. Rev. Lett. **43**, pp. 343–346 (1979), URL <https://link.aps.org/doi/10.1103/PhysRevLett.43.343>
- [106] Y. Kaluzny, P. Goy, M. Gross, J. M. Raimond, S. Haroche. *Observation of Self-Induced Rabi Oscillations in Two-Level Atoms Excited Inside a Resonant Cavity: The Ringing Regime of Superradiance*. Phys. Rev. Lett. **51**, pp. 1175–1178 (1983), URL <https://link.aps.org/doi/10.1103/PhysRevLett.51.1175>
- [107] Y. Sonnefraud, N. Verellen, H. Sobhani, G. A. E. Vandenbosch, V. V. Moshchalkov, P. Van Dorpe, P. Nordlander, S. A. Maier. *Experimental Realization of Subradiant, Superradiant, and Fano Resonances in Ring/Disk Plasmonic Nanocavities*. ACS Nano **4**, 3, pp. 1664–1670 (2010), URL <https://doi.org/10.1021/nn901580r>
- [108] M. Wenclawiak, K. Unterrainer, J. Darmo. *Cooperative effects in an ensemble of planar meta-atoms*. Appl. Phys. Lett. **110**, 26, p. 261101 (2017), URL <https://doi.org/10.1063/1.4989691>

- [109] K. Cong, Q. Zhang, Y. Wang, G. T. Noe, A. Belyanin, J. Kono. *Dicke superradiance in solids [Invited]*. J. Opt. Soc. Am. B **33**, 7, pp. C80–C101 (2016), URL <http://josab.osa.org/abstract.cfm?URI=josab-33-7-C80>
- [110] Q. Zhang, T. Arikawa, E. Kato, J. L. Reno, W. Pan, J. D. Watson, M. J. Manfra, M. A. Zudov, M. Tokman, M. Erukhimova, A. Belyanin, J. Kono. *Superradiant Decay of Cyclotron Resonance of Two-Dimensional Electron Gases*. Phys. Rev. Lett. **113**, p. 047601 (2014), URL <https://link.aps.org/doi/10.1103/PhysRevLett.113.047601>
- [111] T. Laurent, Y. Todorov, A. Vasanelli, A. Delteil, C. Sirtori, I. Sagnes, G. Beaudoin. *Superradiant Emission from a Collective Excitation in a Semiconductor*. Phys. Rev. Lett. **115**, p. 187402 (2015), URL <https://link.aps.org/doi/10.1103/PhysRevLett.115.187402>
- [112] Q. Zhang, M. Lou, X. Li, J. L. Reno, W. Pan, J. D. Watson, M. J. Manfra, J. Kono. *Collective non-perturbative coupling of 2D electrons with high-quality-factor terahertz cavity photons*. Nat. Phys. **12**, 11, pp. 1005+ (2016)
- [113] J. A. Curtis, T. Tokumoto, A. T. Hatke, J. G. Cherian, J. L. Reno, S. A. McGill, D. Karaiskaj, D. J. Hilton. *Cyclotron decay time of a two-dimensional electron gas from 0.4 to 100 K*. Phys. Rev. B **93**, p. 155437 (2016), URL <https://link.aps.org/doi/10.1103/PhysRevB.93.155437>
- [114] T. Maag, A. Bayer, S. Baierl, M. Hohenleutner, T. Korn, C. Schueller, D. Schuh, D. Bougeard, C. Lange, R. Huber, M. Mootz, J. E. Sipe, S. W. Koch, M. Kira. *Coherent cyclotron motion beyond Kohn's theorem*. Nat. Phys. **12**, 2, p. 119 (2016)
- [115] V. M. Muravev, I. V. Andreev, V. N. Belyanin, S. I. Gubarev, I. V. Kukushkin. *Observation of axisymmetric dark plasma excitations in a two-dimensional electron system*. Phys. Rev. B **96**, p. 045421 (2017), URL <https://link.aps.org/doi/10.1103/PhysRevB.96.045421>
- [116] A. G. Moiseev, Y. S. Greenberg. *Single-photon superradiant decay of cyclotron resonance in a p-type single-crystal semiconductor film with cubic structure*. Phys. Rev. B **96**, p. 075208 (2017), URL <https://link.aps.org/doi/10.1103/PhysRevB.96.075208>
- [117] J. D. Jackson. *Classical electrodynamics*. Wiley, New York, NY, 3. ed. edition. ISBN 047130932X (1999)
- [118] J. Gospodarič, V. Dziom, A. Shuvaev, A. A. Dobretsova, N. N. Mikhailov, Z. D. Kvon, A. Pimenov. *Superradiant and transport lifetimes of the cyclotron*

- resonance in the topological insulator HgTe*. Phys. Rev. B **99**, p. 115130 (2019), URL
<https://link.aps.org/doi/10.1103/PhysRevB.99.115130>
- [119] O. R. Matov, O. F. Meshkov, O. V. Polishchuk, V. V. Popov. *Theory of electromagnetic emission of 2-dimensional magnetoplasma and cyclotron oscillations in semiconducting heterostructure with periodic screen*. J. Exp. Theor. Phys. **109**, 3, pp. 876–890. ISSN 0044-4510 (1996)
- [120] S. A. Mikhailov. *Radiative decay of collective excitations in an array of quantum dots*. Phys. Rev. B **54**, pp. 10335–10338 (1996), URL
<https://link.aps.org/doi/10.1103/PhysRevB.54.10335>
- [121] S. A. Mikhailov. *Microwave-induced magnetotransport phenomena in two-dimensional electron systems: Importance of electrodynamic effects*. Phys. Rev. B **70**, p. 165311 (2004), URL
<https://link.aps.org/doi/10.1103/PhysRevB.70.165311>
- [122] D. Kozlov, Z. Kvon, E. Olshanetsky, N. Mikhailov, S. Dvoretzky, D. Weiss. *Transport Properties of a 3D Topological Insulator based on a Strained High-Mobility HgTe Film*. Physical Review Letters **112**, 19 (2014)
- [123] A. M. Shuvaev, G. V. Astakhov, G. Tkachov, C. Brüne, H. Buhmann, L. W. Molenkamp, A. Pimenov. *Terahertz quantum Hall effect of Dirac fermions in a topological insulator*. Phys. Rev. B **87**, p. 121104 (2013), URL
<http://link.aps.org/doi/10.1103/PhysRevB.87.121104>
- [124] G. Tkachov, C. Thienel, V. Pinneker, B. Büttner, C. Brüne, H. Buhmann, L. W. Molenkamp, E. M. Hankiewicz. *Backscattering of Dirac Fermions in HgTe Quantum Wells with a Finite Gap*. Physical Review Letters **106**, 7 (2011)
- [125] M. L. Savchenko, Z. D. Kvon, S. Candussio, N. N. Mikhailov, S. A. Dvoretzskii, S. D. Ganichev. *Terahertz Cyclotron Photoconductivity in a Highly Unbalanced Two-Dimensional Electron–Hole System*. JETP Letters **108**, 4, pp. 247–252 (2018)
- [126] K. S. Novoselov, A. K. Geim, S. V. Morozov, D. Jiang, M. I. Katsnelson, I. V. Grigorieva, S. V. Dubonos, A. A. Firsov. *Two-dimensional gas of massless Dirac fermions in graphene*. Nature (London) **438**, p. 197 (2005)
- [127] Y. B. Zhang, Y. W. Tan, H. L. Stormer, P. Kim. *Experimental observation of the quantum Hall effect and Berry’s phase in graphene*. Nature (London) **438**, 7065, pp. 201–204 (2005)

- [128] L. Zhang, Y. Zhang, J. Camacho, M. Khodas, I. Zaliznyak. *The experimental observation of quantum Hall effect of $l=3$ chiral quasiparticles in trilayer graphene*. Nat. Phys. **7**, 12, pp. 953–957 (2011)
- [129] G. M. Minkov, A. V. Germanenko, O. E. Rut, A. A. Sherstobitov, S. A. Dvoretzki, N. N. Mikhailov. *Hole transport and valence-band dispersion law in a HgTe quantum well with a normal energy spectrum*. Phys. Rev. B **89**, p. 165311 (2014), URL <http://link.aps.org/doi/10.1103/PhysRevB.89.165311>
- [130] D. A. Kozlov, M. L. Savchenko, J. Ziegler, Z. D. Kvon, N. N. Mikhailov, S. A. Dvoretzki, D. Weiss. *Capacitance spectroscopy of a system of gapless Dirac fermions in a HgTe quantum well*. JETP Letters **104**, 12, pp. 859–863 (2016), URL <http://dx.doi.org/10.1134/S0021364016240103>
- [131] J. N. Hancock, J. L. M. van Mechelen, A. B. Kuzmenko, D. van der Marel, C. Brüne, E. G. Novik, G. V. Astakhov, H. Buhmann, L. W. Molenkamp. *Surface State Charge Dynamics of a High-Mobility Three-Dimensional Topological Insulator*. Phys. Rev. Lett. **107**, p. 136803 (2011), URL <http://link.aps.org/doi/10.1103/PhysRevLett.107.136803>
- [132] M. Orlita, D. M. Basko, M. S. Zholudev, F. Teppe, W. Knap, V. I. Gavrilenko, N. N. Mikhailov, S. A. Dvoretzki, P. Neugebauer, C. Faugeras, A.-L. Barra, G. Martinez, M. Potemski. *Observation of three-dimensional massless Kane fermions in a zinc-blende crystal*. Nat. Phys. **10**, 3, pp. 233–238 (2014)
- [133] C. Zoth, P. Olbrich, P. Vierling, K.-M. Dantscher, V. V. Bel’kov, M. A. Semina, M. M. Glazov, L. E. Golub, D. A. Kozlov, Z. D. Kvon, N. N. Mikhailov, S. A. Dvoretzki, S. D. Ganichev. *Quantum oscillations of photocurrents in HgTe quantum wells with Dirac and parabolic dispersions*. Phys. Rev. B **90**, p. 205415 (2014), URL <http://link.aps.org/doi/10.1103/PhysRevB.90.205415>
- [134] A. Akrap, M. Hakl, S. Tchoumakov, I. Crassee, J. Kuba, M. O. Goerbig, C. C. Homes, O. Caha, J. Novák, F. Teppe, W. Desrat, S. Koohpayeh, L. Wu, N. P. Armitage, A. Nateprov, E. Arushanov, Q. D. Gibson, R. J. Cava, D. van der Marel, B. A. Piot, C. Faugeras, G. Martinez, M. Potemski, M. Orlita. *Magneto-Optical Signature of Massless Kane Electrons in Cd_3As_2* . Phys. Rev. Lett. **117**, p. 136401 (2016), URL <http://link.aps.org/doi/10.1103/PhysRevLett.117.136401>
- [135] P. Yu, M. Cardona. *Fundamentals of Semiconductors: Physics and Materials Properties*. Advanced texts in physics, Bd. 3, Springer Berlin Heidelberg. ISBN 9783540254706 (2005), URL <https://books.google.at/books?id=W9pdJZoAeyEC>

- [136] J. Gospodarič, V. Dziom, A. Shuvaev, A. A. Dobretsova, N. N. Mikhailov, Z. D. Kvon, E. G. Novik, A. Pimenov. *Band structure of a HgTe-based three-dimensional topological insulator*. *Physical Review B* **102**, 11 (2020)
- [137] K. Ortner, X. C. Zhang, A. Pfeuffer-Jeschke, C. R. Becker, G. Landwehr, L. W. Molenkamp. *Valence band structure of HgTe/Hg_{1-x}Cd_xTe single quantum wells*. *Phys. Rev. B* **66**, p. 075322 (2002), URL
<https://link.aps.org/doi/10.1103/PhysRevB.66.075322>
- [138] E. G. Novik, A. Pfeuffer-Jeschke, T. Jungwirth, V. Latussek, C. R. Becker, G. Landwehr, H. Buhmann, L. W. Molenkamp. *Band structure of semimagnetic Hg_{1-y}Mn_yTe quantum wells*. *Phys. Rev. B* **72**, p. 035321 (2005), URL
<https://link.aps.org/doi/10.1103/PhysRevB.72.035321>
- [139] G. L. Bir, G. E. Pikus. *Symmetry and strain-induced effects in semiconductors*. John Wiley, Chichester (1974)
- [140] S.-C. Wu, B. Yan, C. Felser. *Ab initio study of topological surface states of strained HgTe*. *Europhys. Lett.* **107**, 5, p. 57006 (2014), URL
<https://doi.org/10.1209%2F0295-5075%2F107%2F57006>
- [141] T. Andlauer, P. Vogl. *Full-band envelope-function approach for type-II broken-gap superlattices*. *Phys. Rev. B* **80**, p. 035304 (2009), URL
<https://link.aps.org/doi/10.1103/PhysRevB.80.035304>
- [142] S. A. Tarasenko, M. V. Durnev, M. O. Nestoklon, E. L. Ivchenko, J.-W. Luo, A. Zunger. *Split Dirac cones in HgTe/CdTe quantum wells due to symmetry-enforced level anticrossing at interfaces*. *Phys. Rev. B* **91**, p. 081302 (2015), URL
<https://link.aps.org/doi/10.1103/PhysRevB.91.081302>
- [143] G. M. Minkov, A. V. Germanenko, O. E. Rut, A. A. Sherstobitov, M. O. Nestoklon, S. A. Dvoretzki, N. N. Mikhailov. *Spin-orbit splitting of valence and conduction bands in HgTe quantum wells near the Dirac point*. *Phys. Rev. B* **93**, p. 155304 (2016), URL
<https://link.aps.org/doi/10.1103/PhysRevB.93.155304>
- [144] L. S. Bovkun, A. Ikonnikov, V. V. Y. Aleshkin, K. E. Spirin, V. Gavrilenko, I. N. N. Mikhailov, S. A. Dvoretzskii, F. Teppe, B. A. Piot, M. Potemski, M. Orlita. *Landau level spectroscopy of valence bands in HgTe quantum wells: effects of symmetry lowering*. *J. Phys.: Condens. Matter* **31**, 14, p. 145501 (2019)
- [145] G. Dresselhaus. *Spin-Orbit Coupling Effects in Zinc Blende Structures*. *Phys. Rev.* **100**, pp. 580–586 (1955), URL
<https://link.aps.org/doi/10.1103/PhysRev.100.580>

- [146] C. Brüne, C. Thienel, M. Stuiber, J. Böttcher, H. Buhmann, E. G. Novik, C.-X. Liu, E. M. Hankiewicz, L. W. Molenkamp. *Dirac-Screening Stabilized Surface-State Transport in a Topological Insulator*. Phys. Rev. X **4**, p. 041045 (2014), URL <https://link.aps.org/doi/10.1103/PhysRevX.4.041045>
- [147] M. Zholudev, F. Teppe, M. Orlita, C. Consejo, J. Torres, N. Dyakonova, M. Czapkiewicz, J. Wróbel, G. Grabecki, N. Mikhailov, S. Dvoretiskii, A. Ikonnikov, K. Spirin, V. Aleshkin, V. Gavrilenko, W. Knap. *Magneto spectroscopy of two-dimensional HgTe-based topological insulators around the critical thickness*. Phys. Rev. B **86**, p. 205420 (2012), URL <http://link.aps.org/doi/10.1103/PhysRevB.86.205420>
- [148] E. B. Olshanetsky, Z. D. Kvon, M. V. Entin, L. I. Magarill, N. N. Mikhailov, I. O. Parm, S. A. Dvoretzky. *Scattering processes in a two-dimensional semimetal*. JETP Letters **89**, 6, pp. 290–293 (2009)
- [149] D. A. Kozlov, Z. D. Kvon, N. N. Mikhailov, S. A. Dvoretzskii, J. C. Portal. *Cyclotron resonance in a two-dimensional semimetal based on a HgTe quantum well*. JETP Letters **93**, 3, pp. 170–173 (2011)
- [150] Z. D. Kvon, E. B. Olshanetsky, E. G. Novik, D. A. Kozlov, N. N. Mikhailov, I. O. Parm, S. A. Dvoretzky. *Two-dimensional electron-hole system in HgTe-based quantum wells with surface orientation (112)*. Physical Review B **83**, 19 (2011)
- [151] G. M. Minkov, A. V. Germanenko, O. E. Rut, A. A. Sherstobitov, S. A. Dvoretzki, N. N. Mikhailov. *Two-dimensional semimetal in a wide HgTe quantum well: Magnetotransport and energy spectrum*. Physical Review B **88**, 15 (2013)
- [152] E. Olshanetsky, Z. Kvon, N. Mikhailov, E. Novik, I. Parm, S. Dvoretzky. *Two-dimensional semimetal in HgTe-based quantum wells with surface orientation (100)*. Solid State Communications **152**, 4, pp. 265–267 (2012)
- [153] J. Los, A. Fasolino, A. Catellani. *Generalization of the $k \cdot p$ approach for strained layered semiconductor structures grown on high-index-planes*. Physical Review B **53**, 8, p. 4630 (1996)
- [154] R. Winkler, S. Papadakis, E. De Poortere, M. Shayegan. *Spin-Orbit Coupling in Two-Dimensional Electron and Hole Systems*, volume 41. Springer (2003)
- [155] S. D. Ganichev, L. E. Golub. *Interplay of Rashba/Dresselhaus spin splittings probed by photogalvanic spectroscopy -A review*. physica status solidi (b) **251**, 9, pp. 1801–1823 (2014)

- [156] R. Winkler. *Rashba spin splitting in two-dimensional electron and hole systems*. Physical Review B **62**, 7, pp. 4245–4248 (2000)

Curriculum Vitae

Personal Information

Name Jan Gospodarič
E-mail jan.gospodaric@tuwien.ac.at
Date of birth 23.5.1991
Place of birth Ljubljana, Slovenia
Address Hedwiggasse 2,
1020 Vienna,
Austria



Education

2000-2006 Oskar Kovačič Primary School
2006-2010 General Matriculation, Vič Grammar School, Ljubljana,
2010 – 2014 University of Ljubljana, Faculty for Mathematics and Physics,
Physics BSc,
2014 – 2016 University of Ljubljana, Faculty for Mathematics and Physics,
Condensed Matter MSc,
2017 – present Vienna University of Technology, PhD.

Employment

2012 – 2013 Project work at the Department for Low and Medium Energy
Physics, The Jožef Stefan Institute,
2013 – 2016 Student researcher at the Department for Complex Matter, The
Jožef Stefan Institute,
2017 – 2020 Project assistant in the Solid State Spectroscopy group, Vienna
University of Technology.

Publications

2014 Svetin, D., Vaskivskiy, I., Sutar, P., Goresnik, E., Gospodaric, J.,
Mertelj, T. and Mihailovic, D., *Transitions between photoinduced
macroscopic quantum states in 1T-TaS₂ controlled by substrate
strain*, Applied Physics Express, 7(10), p.103201, DOI:
[10.7567/APEX.7.103201](https://doi.org/10.7567/APEX.7.103201),

- 2015 Vaskivskyi, I., Gospodaric, J., Brazovskii, S., Svetin, D., Sutar, P., Goreschnik, E., Mihailovic, I.A., Mertelj, T. and Mihailovic, D., *Controlling the metal-to-insulator relaxation of the metastable hidden quantum state in 1T-TaS₂*, Science advances, 1(6), p.e1500168, DOI: [10.1126/sciadv.1500168](https://doi.org/10.1126/sciadv.1500168),
- 2016 Vaskivskyi, I., Mihailovic, I.A., Brazovskii, S., Gospodaric, J., Mertelj, T., Svetin, D., Sutar, P. and Mihailovic, D., *Fast electronic resistance switching involving hidden charge density wave states*, Nature communications, 7, p.11442, DOI: [10.1038/ncomms11442](https://doi.org/10.1038/ncomms11442),
- 2018 Gospodaric, J., Kuzmenko, A., Pimenov, A., Huber, C., Suess, D., Rotter, S. and Pimenov, A., *3D-printed phase waveplates for THz beam shaping*, Applied Physics Letters, 112(22), p.221104, DOI: [10.1063/1.5027179](https://doi.org/10.1063/1.5027179),
- 2019 Gospodaric, J., Dziom, V., Shuvaev, A., Dobretsova, A.A., Mikhailov, N.N., Kvon, Z.D. and Pimenov, A., *Superradiant and transport lifetimes of the cyclotron resonance in the topological insulator HgTe*, Physical Review B, 99(11), p.115130, DOI: [10.1103/PhysRevB.99.115130](https://doi.org/10.1103/PhysRevB.99.115130),
- 2020 Gospodaric, J., Dziom, V., Shuvaev, A., Dobretsova, A.A., Mikhailov, N.N., Kvon, Z.D., Novik, E.G., and Pimenov, A., 2020, *Band structure of a HgTe-based three-dimensional topological insulator*, Physical Review B, 102(11), p.115113, DOI: [10.1103/PhysRevB.102.115113](https://doi.org/10.1103/PhysRevB.102.115113).